Functional and Mechanical *in vitro* Analyses of the Mammary Gland Basement Membrane as a Barrier During Cancer Invasion

Doctoral thesis

submitted in partial fulfillment of the
requirements for the degree of

Doctor rerum naturalium (Dr. rer. nat.)

to the
Mathematisch-Naturwissenschaftlichen Fakultät der
Rheinischen Friedrich-Wilhelms-Universität Bonn

by

Aljona Gaiko-Shcherbak
from Tokmak, Kyrgyzstan

Bonn, August 2018

Angefertigt mit Genehmigung der Mathematisch-Naturwissenschaftlichen Fakultät der Rheinischen Friedrich-Wilhelms-Universität Bonn.

1. Gutachter: Prof. Dr. Rudolf Merkel
2. Gutachter: Prof. Dr. Ulrich Kubitscheck

Tag der mündlichen Prüfung: 28.01.2019
Erscheinungsjahr: 2019

In loving memory of my grandfather

Abstract

Among women, breast cancer is the most frequently diagnosed cancer and the leading cause of cancer deaths worldwide. Despite extensive research, the processes involved in invasion of malignant breast cancers are still not fully recognized. In general, the invasion in breast cancer is a highly coordinated process between cancer cells and their microenvironment. In the past decades, the basement membrane gained a crucial role as regulator of cell behavior. However, *in vivo* it is challenging to analyze the processes invasive cells use to break through the basement membrane. Therefore, three-dimensional cultivation of the non-transformed human mammary gland cell line MCF10A, which recapitulates the cellular organization found in mammary acini *in vivo*, made these cells a suitable physiological 3D *in vitro* breast gland model to study the role of the basement membrane during cell invasion. A unique feature of the MCF10A acini model is the tunable thickness of their basement membrane.

It was hypothesized that basement membrane disruption and cell transmigration can be triggered by exogenous stress. Therefore, in this thesis the MCF10A acini model system was used to investigate to what extent the basement membrane integrity suppresses cell invasion. Thereby the interrelated factors like tumor-associated ECM-stiffening, growth factor stimulation, and actomyosin contractility were analyzed on their ability to induce cell invasion through the basement membrane in MCF10A acini.

Using life cell imaging, invasion onset and overall incidence of cell-basement membrane transmigration were determined in dependency of both, normal breast- and tumor-like ECM stiffness. It could be demonstrated that a stiff matrix triggered cell invasion and increased invasion incidence compared to a soft matrix. Simultaneously, the basement membrane played a gatekeeper role by retaining the cells from invasion. Cell transmigration through the basement membrane could be further triggered by aberrant stimulation with epidermal growth factor (EGF) and showed that the mechanosensitivity of MCF10A acini could be switched-off by EGF, while the role of the basement membrane as a mechanical sustainer was strengthened.
On the basis of these results, it was analyzed whether, and to what extent, the basement membrane disruption is accompanied by proteolytic degradation by matrix metalloproteinases (MMPs) during acinar invasion. For that, highly developed and thick basement membrane in MCF10A acini was first purposely weakened by type IV collagenase and showed that even on soft ECM, cells invaded the substrate in partial absence of the basement membrane, again indicating the crucial role of the basement membrane as a barrier. To demonstrate that during

cell invasion in MCF10A acini the basement membrane was proteolytically weakened, MMP activity was inhibited. The results revealed a decrease of invasion incidence in MCF10A acini independent on substrate stiffness, and showed that MMPs are indeed involved in basement membrane degradation, but their activity was shown to be EGF dependent.

Additionally, finger-like protrusions were observed in MCF10A acini reaching through the basement membrane. These actin-rich protrusions were hypothesized to be filopodia-like protrusions that are responsible for sensing of the extracellular microenvironment. These assumption indicating that MCF10A acini are mechanosensitive and able to respond to changes of ECM stiffness was analyzed by measuring forces generated by MCF10A acini during invasion. Thereby it was determined whether, and to what extent, basement membrane disruption is accompanied by altered cell force generation and quantitatively characterized the local invasion process in detail by traction force microscopy (TFM) and elastic resonator interference stress microscopy (ERISM). Interestingly, TFM analyses showed progressively increasing cell forces during cell-mediated basement membrane-breakdown and outgrowth. Additionally, the tumor-like ECM stiffness considerably contributed to generation of higher forces. By ERISM, local, vertical substrate deformations were detected during the early invasion phase in MCF10A acini, strengthening the contribution of the filopodia-like protrusion in being involved in mechanosensing.

Based on these results, it was aimed to analyze which signaling pathway might be involved in induction of the invasive phenotype in MCF10A acini. It could be demonstrated that phosphoinositide 3-kinase (PI3K) is a crucial factor in upstream signaling pathway, as its inhibition led to a significant decrease of invasion incidence and retarded invasion onset.

The results of this thesis demonstrate that the key mechanism of cancer cell invasion is a proteolytic-driven basement membrane transmigration mechanism which is activated by stiff matrix and aberrant EGF signaling. These findings highlight the crucial role of basement membrane-integrity as a mechanical barrier against breast cancer cell invasion.

Contents

Abbreviations

2D	Two-dimensional
3D	Three-dimensional
BM	Basement membrane
CI	Confidence interval
Col-IV	Type IV collagen
DCIS	Ductal carcinoma *in situ*
ECM	Extracellular matrix
EGF	Epidermal growth factor
EGFR	Epidermal growth factor receptor
EHS	Engelberth-Holm-Swarm
EMT	Epithelial-mesenchymal transition
ERISM	Elastic resonator interference stress microscopy
F-actin	Filamentous actin
fJ	Femtojoule
GPa	Giga Pascal
hd	Highly-developed
IDC	Invasive ductal carcinoma
kPa	Kilo Pascal
Lam-332	Laminin-332
ld	Low-developed
MMP	Matrix metalloproteinase
MT-MMP	Membrane-type matrix metalloproteinase
n.s.	Not significant
Pa	Pascal
PI3K	Phosphoinositide 3-OH kinase
TDLU	Terminal ductal lobular unit
TFM	Traction force microscopy
TGF-α	Transforming growth factor alpha

1. Introduction

Breast cancer is one of the most common incident cancers and the leading cause of cancer deaths in women. According to the latest estimates, there were 1.67 million new breast cancer cases diagnosed worldwide in 2012, accounting for 25 % of all cancers, and 522,000 deaths from breast cancer, accounting for 14.7 % of all cancer deaths among women [1,2]. The incidence of breast cancer is increasing, and in Europe the number of breast cancer deaths in 2018 is predicted to be 92,700 [3].

Breast cancer is a heterogeneous disease resulting from the interplay between accumulated genetic disorders and different risk factors [4]. About 5-10% of all breast cancer cases are associated with genetic susceptibility to the disease [5]. Germline mutations in tumor suppressor genes *breast cancer susceptibility gene 1* (*BRCA1*) and *breast cancer susceptibility gene 2* (*BRCA2*) for instance, confer predisposition to early-onset breast- and ovarian cancers. Carriers with mutations in one of these genes are thought to have a 60-80% risk to develop breast cancer [6]. Though, environmental and lifestyle factors (90-95%), rather than inherited genetic factors (5-10%) account for the majority of sporadic breast cancers [5]. Diverse investigations have identified the primary risk factors for breast cancer to be linked to the hormonal milieu to which the breast is exposed. Generally, those are the reproductive risk factors such as early age at the menarche, late age at first full term pregnancy, late age at any birth, nulliparity and late age at menopause [7]. Moreover, modern life style, including smoking tobacco, alcohol intake, obesity, as well as low physical activity, increase the risk of breast cancer additionally [8].

Importantly, in breast cancer patients it is not the primary tumor which causes death, but the result of metastases [9]. Metastasis begins with invasion of cancer cells from the primary tumor into the adjacent tissue. In this process, a metastatic cell encounters several barriers like other cells or the extracellular matrix which have to be overcome prior the cell reaches a blood or lymphatic vessel to travel to distant organs where the cell can reside and form a metastasis [10]. One of those barriers that cells need to penetrate, is the basement membrane which histologically depicts the difference between non-invasive and invasive cancers. But the mechanisms that enable cell invasion through this structural barrier are still insufficiently understood [11]. It is therefore highly important to understand factors that regulate cancer cell invasion through the basement membrane [12].

1. Introduction

1.1. Anatomy of the human breast

The mature female breast is organized by several tissue types, with the main ones being glandular, adipose and connective tissues. Of those, the most important is the glandular tissue, known as mammary gland.

The mammary gland is an exocrine gland that functions to produce and secrete milk in order to feed offspring [13]. It has a unique characteristic since, in contrast to other organs, its development is not completed during embryogenesis, but continues during postnatal life and reaches its mature functional state only by the end of the first full term pregnancy [14,15]. Furthermore, mammary gland undergoes extended remodeling during each menstrual cycle, directly regulated by circulating hormones and growth factors, including progesterone, oestrogen, prolactin and epidermal growth factor (EGF) [14].

In general, the mammary gland is composed of 15-20 lobes that are connected through a complex network of branched ducts to the nipple (see Figure 1.1 A) [16]. Each lobe is subdivided into smaller lobules, making up the terminal ductal-lobular units (TDLU). In TDLUs, acini, the smallest constituents of the mammary gland, act as the milk producing and secreting units (see Figure 1.1 B). These acini are composed of two cellular layers, an inner layer of polarized secretory epithelial cells and an outer layer of contractile myoepithelial cells [14,16]. Both layers are in contact with the basement membrane, a highly condensed and organized form of extracellular matrix that provides structural support to the mammary gland and separates it from the adjacent stroma (see Figure 1.1 C) [14,15,17].

The key feature of luminal epithelial cells is their polarized organization, with apical site facing the lumen, and basal site adhering to the basement membrane. The polar architecture of epithelial cells is determined by a variety of cell adhesion complexes that assemble the cells together. Therefore, the normal tissue architecture and its integrity depend on cell-cell and cell-basement membrane interactions [18,19]. Tight junctions help to maintain epithelial polarity and separate the lumen from intercellular space. Adherens junctions establish and stabilize the cell-cell contacts and connect them to the actin cytoskeleton. Desmosomes bind intermediate filaments and maintain tissue integrity. Gap junctions form the cell-cell communication [20-22]. Additionally, cellular basal polarity is defined by the presence of the basement membrane to which the cells adhere through hemidesmosomes which help to maintain tissue integrity by binding intermediate filaments to the basement membrane (see Figure 1.1 C, zoom-in) [22,23].

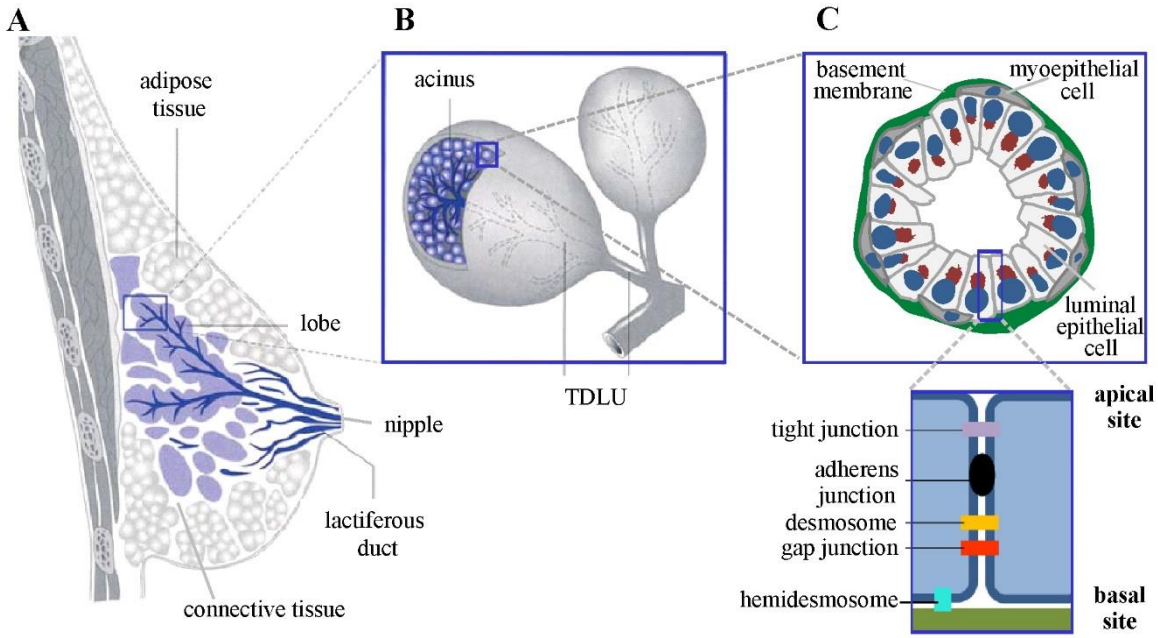

Figure 1.1: Anatomy of the human mammary gland.
A. A mature human breast is composed of three tissue types: adipose-, connective-, and glandular tissues. The glandular tissue (blue) is composed of a complex network of branched lactiferous ducts that connect the functional glandular units (lobes) to the nipple. **B.** Mammary gland tissue is composed of lobes that comprise terminal ductal-lobular units (TDLU) containing acini. **C.** Cross-section through an acinus shows two primary cell types making up the glandular tissue: outer contractile myoepithelial and inner luminal epithelial cells. Both cell layers are in contact with the basement membrane. Zoom-in: epithelial cells show a polarized organization, with apical site facing the lumen, and basal site adhering to the basement membrane. Epithelial polarity is dictated by organization of epithelial junctional complexes (not to scale). Modified from [24,25].

1.2. The basement membrane

The basement membrane is a dense, 50-100 nm (in glomerulus up to 350 nm [26]) thin structure [27], which represents a specialized type of extracellular matrix (ECM) located at the basal site of all epithelial and endothelial cells in the body. It is always associated with cells [28-31].
In general, basement membranes fulfill a variety of biologic functions. One of their leading functions is to separate and simultaneously connect the tissue of its origin from and to the interstitial ECM. Basement membranes provide mechanical support to the tissue of their origin and additionally regulate macromolecular transport between intra- and extravascular spaces [31-33]. Moreover, basement membranes act as growth factor reservoirs and regulate cell behavior initiated by binding of cell surface receptors like integrins to the basement membrane proteins [28,30]. Through these bindings, cells are able to sense the complex biochemical and biomechanical characteristic of the basement membrane and induce cascades of physical and biochemical signals which guide fundamental cell responses like proliferation, matrix secretion

or degradation and migration [31,34]. In a healthy tissue these processes are in balance, preserving the overall architecture of the basement membrane. This tissue homeostasis is of particular importance to cell behavior and any imbalance may lead to disease progression, such as cancer [35-37].

1.2.1. Structure and composition of the basement membrane

The major structural components of the basement membrane are type IV collagen, laminin, nidogen and perlecan (see Figure 1.2). Of these, type IV collagen comprises up to 50 % of the whole basement membrane while laminin is the most abundant non-collagenous protein [30,31,38]. The functional components of type IV collagen and laminin are initially assembled in the Golgi apparatus and secreted via the vesicular secretory pathway, together with nidogen and perlecan, onto the basal site of the cells. In the extracellular space, deposited laminin and type IV collagen self-assemble into two individual sheet-like structures. Structural stability of the basement membrane is given through covalent crosslinking of type IV collagen via disulfide bonds during network formation [11,39]. The formed laminin polymer and type IV collagen network are connected to each other through nidogen and perlecan. This bridging increases the structural integrity of the basement membrane. Adhesion of the basement membrane to the cell is mainly mediated by hemidesmosomes that contain heterodimeric transmembrane receptors called integrins [31,40].

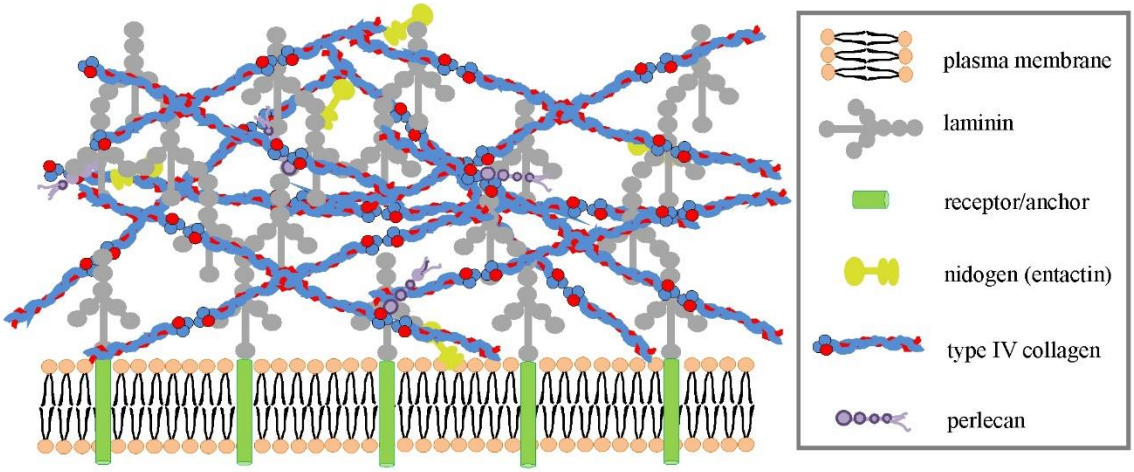

Figure 1.2: Schematic illustration of basement membrane composition.
The main constituents of the basement membrane are type IV collagen, laminin, perlecan and nidogen (entactin). Deposition of these components onto the basal site of the cell initiates their assembly. Type IV collagen and laminins form independent sheet-like structures which are connected and stabilized by nidogen and perlecan. The basement membrane is connected to the cell through anchoring receptor such as integrins. Not to scale. Modified from [30].

Although the main structural components of the basement membranes are the same throughout tissue types, their individual composition is highly dynamic, tissue specific and changes with age and in disease [31,41]. In Figure 1.3 the different organization of the basement membrane in normal and cancerous breast tissues is illustrated. In this example, staining of type IV collagen reveals a strong and continuous basement membrane in physiologically normal breast tissue, while in disease, the pathological breast tissue has no basement membrane.

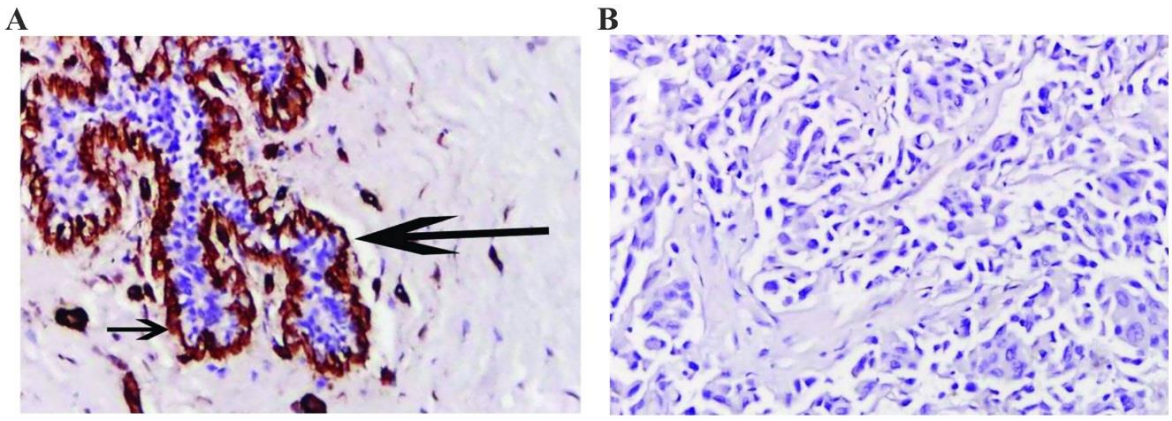

Figure 1.3: Organization of basement membrane in normal and cancerous breast tissues. Immunohistochemical staining of the structure lending protein, type IV collagen, reveals marked differences in the organization of the basement membrane in normal breast tissue and breast cancer. **A.** Normal mammary duct (large arrow). Strong staining of type IV collagen (short arrow) reveals presence of a continuous basement membrane in normal breast tissue. **B.** Breast cancer tissue, negative for collagen IV staining. Modified from [42]: Hematoxylin and eosin staining; original magnifications, x20.

1.3. Factors promoting breast cancer invasion through the basement membrane

Most of the human cancers, including breast cancer, arise from epithelial cells. Cancer from epithelial cells are termed carcinomas and are characterized by loss of growth control, cellular polarity and epithelial organization. One key factor that differentiates benign tumor cells from highly malignant ones is the ability of malignant cells to break through the basement membrane and invade the adjacent tissue [12]. Those cells might detach from the primary tumor and form metastasis at distant organs which is associated with high mortality [9,43].

In the past decades the basement membrane was recognized as a crucial regulator of cell behavior and has been shown to define tumor microenvironment and to regulate signals during tumor progression [30,44]. However, the factors that induce cellular transformation and invasion through the basement membrane are still insufficiently understood. It is hypothesized

that invasion of malignant cells is influenced by a cross-talk of three interrelated factors: growth factor signaling, stromal stiffening and epithelial cytoskeletal contractility (see Figure 1.4). Thereby, the stromal stiffening in cancers is a result of stromal cells activation and infiltration of immune cells. Stiffened ECM in turn stimulates contractility of the cytoskeleton of the transformed epithelial cells. Increased contractility leads to the formation of cell protrusions (collectively called invadosomes), and to production of matrix degrading enzymes, like matrix metalloproteinases (MMPs), which are required for invasion through the basement membrane. In addition, increased cytoskeletal contractility also induces further stromal stiffening. Both, cytoskeletal contractility and stromal stiffening are regulated by growth factor signaling, but also serve to amplify the growth factor signaling pathways, which are involved in promoting cell invasion through the basement membrane [12]. In the following chapters the important roles of those factors in breast cancer development and the ways they promote tumor progression and the resulting cell invasion through the basement membrane will be described in more detail.

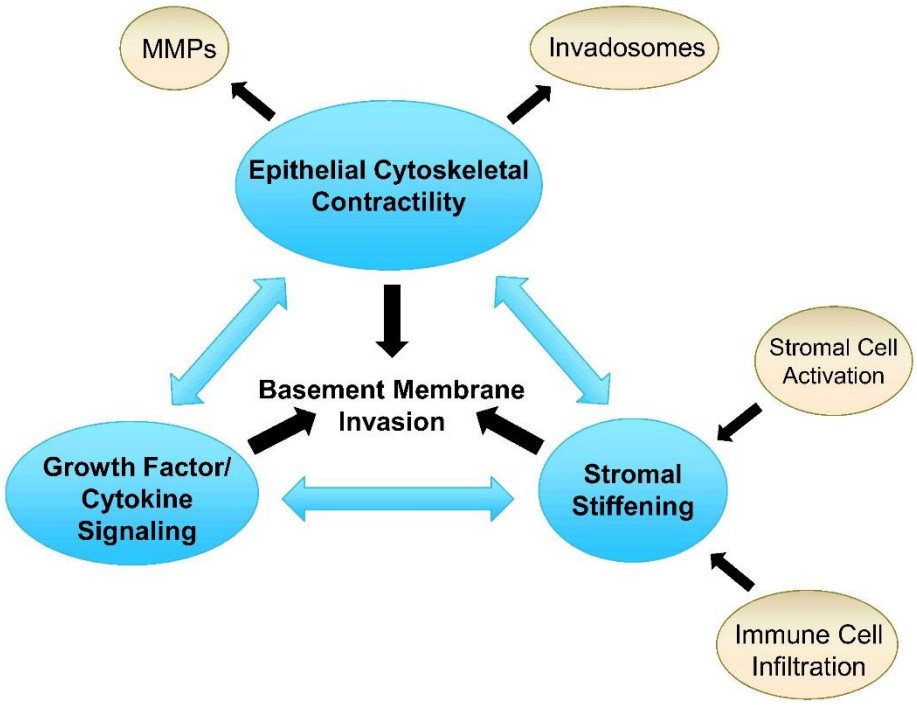

Figure 1.4: Interrelated factors that influence basement membrane transmigration.
Three cohesive factors (blue), growth factor signaling, stromal stiffening and epithelial cytoskeletal contractility interact and promote invasion of cancer cells through the basement membrane. MMPs: matrix metalloproteinases. Figure from [12].

1.3.1. Impact of growth factor signaling on basement membrane invasion

Disruption of cellular polarity and cancer progression are associated with activation of several signaling pathways by which the tissue microenvironment is remodeled [45]. One prominent example is the signaling pathway through the epidermal growth factor receptor (EGFR). EGFR is a transmembrane receptor which is activated by binding of its ligands, EGF and transforming growth factor-alpha (TGF-α). Both of those ligands are produced by cells from the surrounding tissue and act locally as growth factors [46]. Activation of EGFR can activate a variety of downstream signaling pathways leading for example to DNA synthesis and proliferation [47]. The physiological function of EGFR is, among others, the regulation of epithelial tissue differentiation and homeostasis. Therefore, any aberrant activity of EGFR activated pathways can result in dysregulation of cell growth and initiate tumor development [47,48].

Overexpression of EGFR was identified in up to 91 % of breast cancers and is associated with large tumor size, loss of differentiation and poor clinical outcome [46,49]. Additionally, aberrant activation and overexpression of EGFR is linked to increased cell migration and invasion induction [47,49]. A common process by which cells lose their polarity and differentiation and switch from epithelial to a fibroblast-like phenotype is called epithelial-to-mesenchymal transition (EMT) and was shown to be promoted by EGFR [18,49]. EMT is described as the key process of migrating cancer cells which are capable to migrate through the basement membrane [49,50].

1.3.2. The role of stroma changes in basement membrane invasion

In a tissue, cells continuously experience physical forces which modulate cell fate and direct their function. Such physiological forces are for example shear stress, induced by the blood flow, and compressive or tensile stress, induced during mammary gland lactation [51]. Hence, cell health is mediated by the extracellular environment which provides not only biochemical (for example soluble growth factors), but also biomechanical stimuli to control cell behavior [52].

One of those fundamental biomechanical stimuli is ECM stiffness, an isomeric force which controls cell behavior at the nanoscale level. Stiffness is a measure of material property and describes the ability of a material to resist deformation in response to applied forces [52,53].

Each tissue has a characteristic stiffness optimum which is determined by ECM composition, concentration and organization of matrix components [51,54]. Thus for example the optimal stiffness of human brain lies in the range of 0.1-1 kPa, that of the muscle cells in the range of

8-17 kPa, while that of bones lies in the range 2-4 GPa [51,55]. Human breast tissue is very soft and lies in the range between 150 Pa and 3 kPa [56]. Under normal conditions, the resting mammary gland remains very compliant and mechanically static (see Figure 1.5 A) [51,57]. Importantly, the stiffness optimum can change during malignant transformations and developing breast cancers are accompanied by stiff ECM which can reach a stiffness of more than 10 kPa [51,58]. In line with this observation, increasing stroma stiffness has been found to be an independent risk factor that is associated with high risk to develop breast cancer [59].

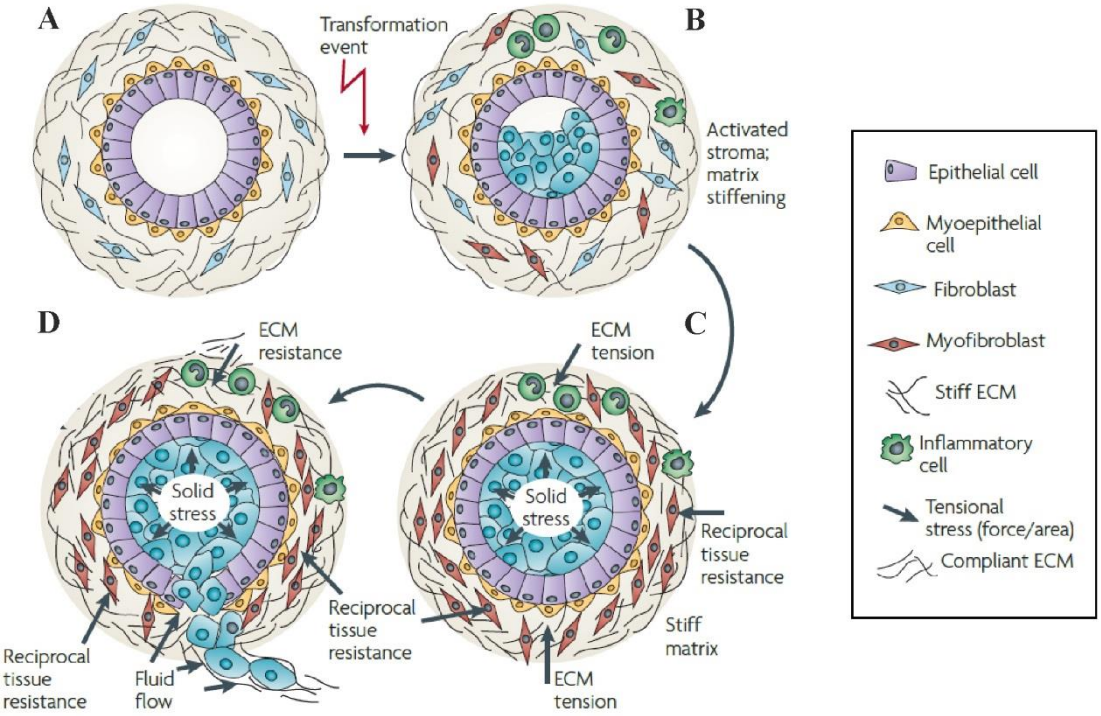

Figure 1.5: Tensional forces in normal and malignant mammary gland.
A. Resting mammary gland is mechanically static and very compliant. **B.** Following genetic transformations, luminal epithelial cells start uncontrolled proliferation and fill up the lumen of the mammary duct. Simultaneously, the surrounding stroma is modified by activated fibroblasts (myofibroblasts), leading to matrix stiffening and infiltration of inflammatory cells. **C.** Those events lead to growth induced solid stress, which is exerted by the tumor mass on the surrounding cells and the ECM. To resist tumor expansion, ECM exerts inward projecting reciprocal stress. **D.** The combination of these reciprocal stresses acts upon tumor cells and induce their invasion into the interstitial tissue. Modified from [51].

As delineated in the previous Section (1.3.1), aberrant growth factor signaling can initiate epithelial polarity loss and contribute to increased cell proliferation and finally foster tumorigenesis through impaired tissue homeostasis [51,60]. As a result, transformed luminal epithelial cells hyper-proliferate. This results in lumen filling of the mammary duct or acinus.

This tissue state is the earliest detectable histological form and the most common type of non-invasive breast cancers, known as the ductal carcinoma *in situ* (DCIS) (see Figure 1.5 B). Although in DCIS the basement membrane remains intact, surrounding the myoepithelial and epithelial cells [12,61], the proliferating cancer cells secrete different growth factors, such as EGF, leading to activation of tumor stroma. In tumor stroma, activated fibroblasts, which are the key regulators of ECM organization and composition, start a chronic wound healing-like response, leading to dramatic changes in ECM composition, stimulation of immune cells infiltration and matrix stiffening. These events are associated with increased tension of the mammary gland and lead to development of mechanical stress (see Figure 1.5 C) [51,57].
The expanding tumor mass exerts outward projecting compressive forces (solid stress) on surrounding myoepithelial cells and the basement membrane, which in turn apply reciprocal inward projecting compressive stress to resist tumor expansion (see Figure 1.5 C) [51,57]. The consequence of matrix stiffening is increased cellular motility, since cells tend to migrate to stiffer environments, a tendency known as durotaxis [62]. Therefore the described physical forces act till some tumor cells undergo malignant transformations, for example EMT (see also Section 1.3.1), and induce invasion via basement membrane degradation, resulting in invasive ductal carcinoma (IDC) (see Figure 1.5 D) [57,63]. Hence, precancerous lesions such as DCIS are clinically distinguished from invasive cancers by the existence of an intact basement membrane [61]. This indicates, that the basement membrane is an essential gatekeeper that retains tumorigenic cells within its boundaries [64].

1.3.3. Proteolytic and force mediated invasion of the basement membrane

Throughout animal embryonic development, cells migrate to distant sites in order to construct tissues. But as already indicated in previous sections, cellular migration is also a vital process in adult life, as for example in wound healing, immune cell trafficking and cancer [65]. During these migration processes, cells encounter several barriers, including other cells and ECMs. Of these, due to their dense structure and small pores, basement membranes are the most difficult barriers cells need to penetrate through [66-68]. Intriguingly, cells acquired a multi-step mechanism to remodel the basement membrane and the underlying ECM: First the actin-cytoskeleton is polymerized to form cellular protrusions that can bind to the underlying matrix. The binding is mediated through integrin adhesions, followed by a reversible proteolytic degradation of the basement membrane by proteases, such as matrix metalloproteinases

(MMPs). Finally, cells break through the basement membrane by actomyosin-mediated contraction, thereby generating forces to the substrate [65].

Invasion initiating protrusions

To initiate migration, cells first have to probe their microenvironment. In general, cells are able to sense two types of information: biochemical, such as growth factors (for example EGF), and biophysical, such as ECM stiffness, ECM topography or for example compressive forces [69]. Cell behavior and local mechanical properties of the cells are mainly regulated through contraction of the actomyosin machinery [70]. The cellular actin cytoskeleton is assembled through polymerization of actin monomers into actin filaments (F-actin). To mediate cell contraction, actin filaments are organized into bundles of 10-30 filaments to form the so called stress fibers (see Figure 1.6). The structure of stress fibers is crosslinked to the molecular motor protein myosin II, and the resulting structure is referred to as actomyosin [71,72]. The presence of myosin II is responsible for generation of contractile forces of the cells by sliding along the actin filaments. This sliding leads to pulling forces (required to move the cell body) which are transmitted through cell-matrix adhesions to the ECM [73,74].

Sensing of the biophysical microenvironment usually happens via filopodia, specialized actin-rich protrusions (see Figure 1.6) [75]. Filopodia are described as finger-like membrane protrusions extending from the leading edge of lamellipodia and are linked to enhancement of cell migration [75]. Filopodia extension is driven by actin polymerization toward the plasma membrane which is the key step in cell migration [76]. The unidirectional organization of filopodia allows molecular transport to the tips of the protrusions. Thus, adhesion molecules such as integrins are often found in the tips of filopodia, correlating with their sensing role [75]. Integrins can adhere to their specific ligands on the ECM and recruit different adhesion proteins which link integrins to the actin cytoskeleton and initiate formation of cell-matrix adhesions, called focal adhesions [77]. After formation of focal adhesions, a migrating cell starts contraction of the actomyosin, in order to initiate migration. Subsequently, the cell applies forces by pulling on the substrate and generates tractions to move the cell body forward, simultaneously the cell de-adheres its rear by disassembly of actin bundles and their contraction [78]. Hereby the magnitude of generated forces is coupled with matrix stiffness [74,79]. As mentioned in the previous Sections 1.3.1 and 1.3.2, altered growth factor signaling can lead to malignancy, in turn, malignant cells can activate tumor stroma, leading to increased stiffening of the ECM [51]. Increased matrix stiffness can further promote cancer progression by

increasing cellular motility and invasiveness through increased focal adhesion assembly and generation of larger forces [68,74,79].

Generation of large contractile forces to pull the cell body is usually not enough for efficient cancer cell invasion in a three-dimensional (3D) environment [80]. This is due to the presence of a basement membrane, which is under physiological conditions not permeable to cells. Therefore, the cell requires a mechanism to remodel the basement membrane in order to break through and to escape from its tissue of origin in order to infiltrate the underlying ECM [11].

Although cells are able to elongate their cytoplasm to form protrusions that can reach through and sense the underlying ECM, the degree to which the cell can deform is limited to a certain pore size. In tumor cells this size is primary given by the nucleus. Consequently, invasive cells have to enlarge the basement membrane pore size by focalized proteolytic degradation [65,68]. The exact mechanism of matrix degradation at this stage in a 3D environment is not fully understood yet [81].

In cancer cells increased density of filopodia is considered to be characteristic for invasive cancer cells in 3D [76,82]. Li and colleagues suggested that filopodia might become invasive and are then represented by invasive finger-like protrusions called invadopodia, which are capable to proteolytically degrade the ECM (see Figure 1.6) [83,84]. An additional factor for invasive cellular behavior at filopodia protrusion that strengthens this hypothesis is the fact, that integrins control MMPs on the cell surface [85].

Formation of invadopodia and secretion of MMPs are both stimulated by stiffened ECM and by soluble growth factors, such as EGF [12,68]. In case of invadopodia formation, matrix-degrading enzymes are recruited to the sites of integrin mediated adhesion, allowing local proteolytic degradation of the basement membrane [80].

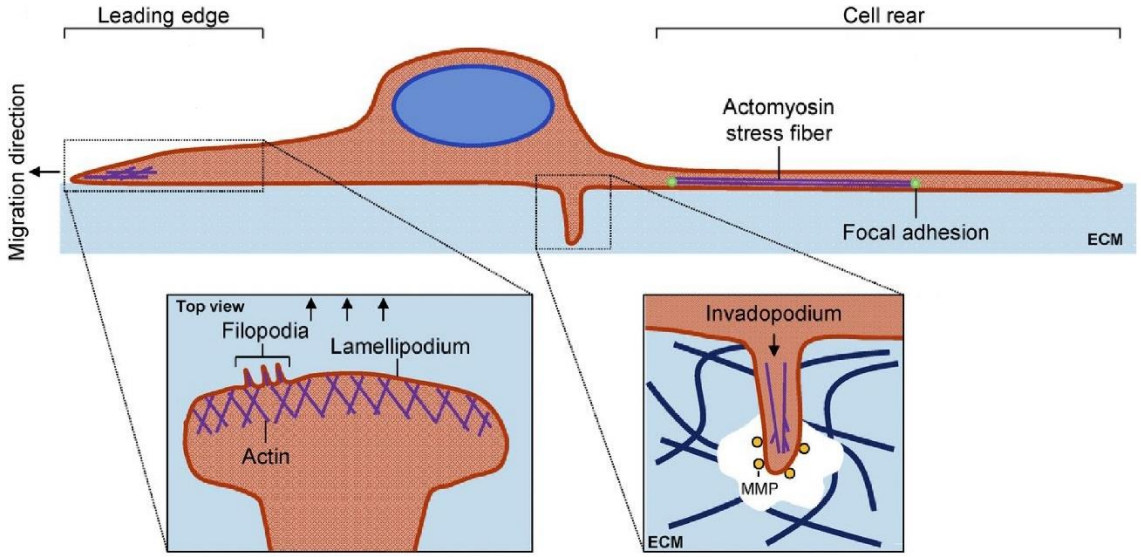

Figure 1.6: Simplified model of a migrating cell.
At the leading edge the migrating cell drives the plasma membrane forward by extending actin rich protrusions, lamellipodium and filopodia. During migration the cell rear is retracted through actomyosin stress fiber coupled to the substrate via focal adhesions. Migration through the ECM is mediated by local degradation of the ECM using specialized protrusions known as invadopodia which secrete MMPs, matrix degrading enzymes. Modified from [86].

Proteolytic degradation of the basement membrane by matrix metalloproteinases

The main and best studied proteases involved in matrix degradation are MMPs, a family of at least 26 zinc-dependent enzymes [87,88]. MMPs are subdivided into two main groups, membrane-anchored or membrane type (MT1-MMP to MT6-MMP) and soluble MMPs, which are additionally classified according to their substrate specificity, such as for example collagenases or gelatinases [89]. MMPs play a central role in normal tissue growth and remodeling, wound healing and angiogenesis through degradation of matrix proteins. Under normal tissue conditions, the activity of MMPs is tightly regulated: in first instance MMPs are produced as inactive precursor enzymes and require activation, they are post-translationally modified and additionally controlled by tissue inhibitors of metalloproteinases [54,90].

In the normal mammary gland for example, the expression of MMPs is generally low, except during the puberty, pregnancy and involution. However, their expression was found to be upregulated in breast cancer and is associated with poor prognosis outcome in breast cancer patients [91,92]. With regard to the mammary basement membrane, which is used histologically to distinguish between non-invasive and invasive cancers, specific type IV collagenases are required by cancer cells for local basement membrane degradation during invasion. A central player during invadopodia mediated ECM degradation is MT1-MMP which is able to cleave several ECM components as well as the pro-enzymes MMP2 and MMP9, the best analyzed

type IV collagenases [11,68]. These two collagenases were shown to be highly active in cancers [93]. Through the activity of MMPs, cancer cells can regulate the extent of basement membrane and underlying matrix degradation, as they have to adhere to it and generate tractions required for migration [87].

1.4. Mammary epithelial MCF10A acini as 3D *in vitro* model

To study molecular mechanisms of clinical relevance, in cancer research the use of cell lines as *in vitro* models has been established as the best choice. Among easy handling and limitless proliferation, there are more than 100 different human breast cancer cell lines available, allowing to investigate mammary-specific functions by culturing mamma carcinoma cell lines of different origin and malignancy [94,95]. Although traditional cultivation of the cells on planar surfaces has been useful for a variety of discoveries, there are limitations due to the lack of extracellular matrices surrounding the cells, which are important regulators of cellular behavior [96]. In order to mimic the *in vivo* environment of the breast, the use of reconstituted basement membranes extracted from Engelberth-Holm-Swarm (EHS) mouse sarcoma has become a standard tool. EHS tumor contains extracellular matrix proteins like laminins and collagens, and is commonly used to culture human mamma carcinoma cells in 3D, achieving *in vivo* like micro tissues [97,98].

MCF10A is a non-transformed, spontaneously immortalized human mammary epithelial cell line [99]. When grown in two-dimensional culture (2D, on culture plastics), MCF10A cells form a confluent monolayer and show a typical epithelial cobblestone morphology, but still appear artificial compared to the spherically organized epithelial cells *in vivo* [16,100,101]. Already a decade ago, Debnath and colleagues pioneered the field of 3D cultivation of MCF10A cells and showed that under defined 3D culture conditions, MCF10A cells form fully differentiated acini with a baso-apical polarity and a hollow lumen [100], recapitulating the 3D cellular organization found in acini *in vivo* (see Section 1.1). Debnath and also other research groups have demonstrated that upon seeding the mammary cells onto EHS matrix, those cells start to proliferate and differentiate into cell clusters. As the morphogenesis proceeds, the first signs of baso-apical polarity becomes evident within those clusters. During further differentiation, the cell clusters take a more ordered acinus-like organization, and two distinct cell populations emerge within each acinus: a polarized outer layer secreting the endogenous

basement membrane, and an inner region of cells. These inner cells start to undergo apoptosis, leading to lumen formation [16,100,102]. In a recent study our group could adopt the 3D culture protocol from Debnath and colleagues and demonstrate that MCF10A acini differentiation and basement membrane formation are highly sensitive to EGF stimulation (see Figure 1.7) [33]. Following EGF stimulation for nine days, the deposited basement membrane reproducibly develops in terms of thickness and stability during differentiation.

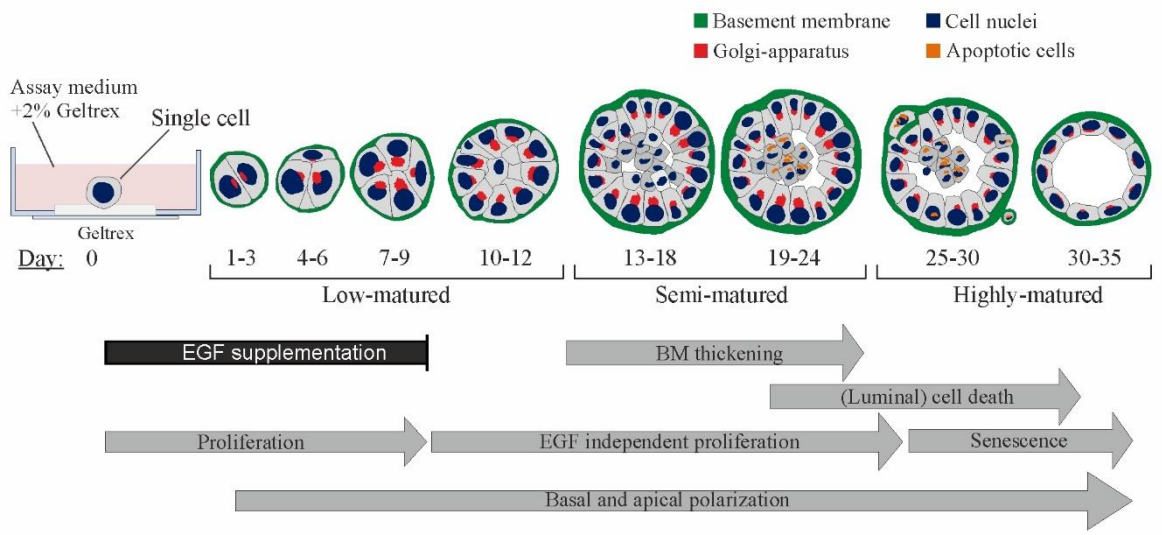

Figure 1.7: Temporal progression of MCF10A acinar differentiation on 3D matrix.
Upon seeding of a single cell suspension onto an EHS substrate, individual cells start proliferation and form a cell cluster after about 4 days in culture. In the early stages of culture, MCF10A cells respond to the exogenous ECM and deposit an endogenous BM, mainly composed of type IV collagen and laminin-322. Already in this phase of morphogenesis the first signs of baso-apical polarization become evident within the cell clusters. As culture progresses at days 7 through 12, the cell cluster takes a more ordered acinus-like form and two distinct cell populations emerge within each acinus: a polarized outer layer secreting the endogenous BM proteins, and an inner region of cells. Those inner cells start to undergo apoptosis by day 13 in culture, leading to lumen formation visible by day 25. Modified from [33].

The described morphology of MCF10A acini makes these cells a suitable physiological 3D *in vitro* breast gland model to study the role of the basement membrane during cell invasion. Since this model does not contain myoepithelial cells which are present *in vivo* (see Section 1.1), this simplified system allows to focus on the investigation of the basement membrane alone, without the need to consider other factors presented by myoepithelial cells, such as additional cell-cell contacts or their interaction with the basement membrane. A unique feature of MCF10A acini model is the tunable thickness of the endogenous basement membrane, which allows the investigation of different states of the basement membrane.

1.5. Aim

During cancer invasion, the basement membrane is one of the most important and difficult barriers invasive cells need to penetrate through to escape from the primary lesion. But the exact mechanisms cells use during this process are still poorly understood. It is therefore pivotal to analyze and identify factors that might be involved in cancer invasion. Uncovering the involved mechanisms could be used to identify possible targets for an efficient therapy that would help to hinder metastatic outcome in breast cancer. The aim of this thesis was therefore to investigate the basement membrane as a mechanical barrier against invasive cells in the human mammary gland. Thereby the focus had to be laid on three main factors that were known to influence cancer invasion and were thought to interplay during this process, namely matrix stiffening, growth factor signaling and actin contractility. For this purpose a suitable 3D *in vitro* invasion assay had to be designed which would enable analyses of these factors.

The non-transformed human mammary epithelial cell line, which forms acini with an endogenous basement membrane when cultured in 3D, mimics the cellular organization found in the mammary gland *in vivo*. The possibility to tune the thickness of the basement membrane in MCF10A acini during their differentiation, made these cells a suitable model system to analyze cell invasion through the basement membrane.

Mechanical properties of the tumor microenvironment play an important role in regulating the outcome and aggressiveness of the tumor. It is described that cells in a tissue constantly sense their mechanical environment and respond to it by activation of appropriate physiological processes. In this context, increased matrix stiffness is known to upregulate cancer invasion. Stiff ECM is associated with higher breast cancer risk. Thus, cell fate, tissue development and its proper functions are force-modulated and tissue force homeostasis is an important factor to maintain a healthy tissue. Loss of tissue homeostasis can lead to cancer progression. Therefore, using MCF10A acini model, the aim was to determine whether invasion in MCF10A acini can be triggered by matrix stiffening. Since stiff ECM is often accompanied by overexpression and aberrant upregulation of growth factor receptors in many breast cancers, the effect of EGF had to be analyzed on its ability to trigger or even to increase the invasive potential of MCF10A acini. The invasive potential of MCF10A acini had to be analyzed on different matrix rigidities, ranging from the normal breast stiffness to the tumor stroma rigidity. Additionally, it had to be analyzed, how increased matrix stiffness influences force generation through actomyosin contractility in MCF10A acini during invasion. The focus of this analysis should be laid on the

phase prior to invasion onset, to analyze early vertical substrate interactions and lateral stress that might be applied by MCF10A acini to the substrate during invasion. Simultaneously, the role of the basement membrane had to be observed during these processes on its ability to suppress cell invasion.

It is known that invasive breast cancer cells use cellular protrusions like invadopodia to proteolytically degrade the ECM. By using biochemical drugs affecting the state of the basement membrane, the aim was to determine whether the basement membrane in MCF10A acini is proteolytically degraded during invasion. On the basis of the outcome of these experiments, it had to be analyzed which signaling pathway might be involved during MCF10A acinar invasion that links the extracellular stimulation to intracellular signaling cascades.

2. Materials and Methods

2.1. Materials

2.1.1. Instruments and equipment

Instruments and equipment	Supplier
Camera: AxioCam MRm, camera chip: 6.5 µm pixel size	Carl Zeiss, Jena
Cell counter, Moxi Z, mini automated cell counter	Orflo Technologies, Hailey, ID, USA
Centrifuge 5415R	Eppendorf, Wesseling
Clean room workbench Hera Safe	Heraeus / Kendro, Hanau
CO_2-Modul S	Carl Zeiss, Jena
Cold light source CL 1500 ECO	Carl Zeiss, Jena
Freezing container, Nalgene® Mr. Frosty	Thermo Scientific, Langenselbold
Heating Insert PS	Carl Zeiss, Jena
Heating Insert XLS	Carl Zeiss, Jena
Incubator XL 2	Carl Zeiss, Jena
Incubator: Heracell 150i CO_2	ThermoFisher Scientific, Waltham
KNF Laboport® Solid PTFE Vacuum Pump	KNF Neuberger Inc.,Trenton, NJ, USA
Laboratory scales JB1603-C/FACT	Mettler-Toledo, Giessen
Laser-Scanning-Microscope LSM 710, LSM 880 with Airyscan	Carl Zeiss, Jena
Light source for fluorescence illumination HXP-120	Carl Zeiss, Jena
Microscope: Axio Observer Z1	Carl Zeiss, Jena
Microscope: Axiovert 40 CFL	Carl Zeiss, Jena
Obcective: LD C-Apochromat M27 63x/1.15 W Corr	Carl Zeiss, Jena
Objective: C-Apochromat 40x/1.2 W Autocorr M27	Carl Zeiss, Jena
Objective: EC Plan-Neofruar 40x/1.30 Oil Ph3 M27	Carl Zeiss, Jena
pH-Meter, 766 Calimatic	Knick, Berlin
Pipette Controllers accu-jet pro	neoLab Migge, Heidelberg
Pipetters, adjustable volume, 10, 20, 200 and 1000 µL volume	Eppendorf, Wesseling
Plasma oven Pico	Diener Electronics, Ebhausen
Sigma 3-16L centrifuge	Sigma Laborzentrifugen, Osterode am Harz
Spin-coater Delta 10 TT	SÜSS MicroTec Lithography, Garching
Stemi-2000 CS stereo microscope	Carl Zeiss, Jena
Universal Oven	Memmert, Schwabach
Vacuum exsiccator	Duran, Wertheim
Vortex REAX top	Heidolph, Schwabach
Water filtration station: MilliQ Gradient A10	Merck, Darmstadt
Waterbath WB22	Memmert, Schwabach

Disposable materials

Materials	Supplier
Cell-culture dishes Ø 35 mm, predrilled cut Ø 17 mm	Greiner bio-one, Frickenhausen
Cryovials, 1.5 mL	Nalgene, Thermo Scientific, Langenselbold
Disposable measuring pipettes, sterile, 2.5 mL, 5 mL, 10 mL, 50 mL	Corning B.V. Life Sciences, Amsterdam, The Netherlands
Eppendorf tubes, safe lock, 0.5 mL, 1.5 mL, 2 mL	Eppendorf, Hamburg
Falcon tubes, 15 mL, 50 mL	BD Biosciences, San Jose, CA, USA
Glass coverslips: # 00, # 0, # 1, # 1.5 high precision	Menzel Gläser, Thermo Scientific, Langenselbold
Glass Pasteur pipettes	VWR Collection, Darmstadt
Low bind reaction vessels, 1.5 mL, 2 mL	Eppendorf, Hamburg
Moxi Z cell count cassettes type S	Orflo Technologies, Hailey, ID, USA
Syringe filters Acrodisc PES, Supor, pore size 0.1 µm	Pall Laboratory, Dreieich
TipOne Pipette Tips, 10 µL, 200 µL, 1250 µL, graduated	Starlab, Hamburg
Tissue culture flasks 25cm^2	BD Biosciences, Heidelberg
Petri dishes	VWR Collection, Darmstadt
Beakers, 100 mL, 500 mL, 1000 mL	VWR Collection, Darmstadt
Spatulas	VWR Collection, Darmstadt
Weighing boats, anti-static	VWR Collection, Darmstadt

2.1.2. Software

Nomination	Supplier
ZEN 2.3 blue edition	Carl Zeiss, Jena
ZEN black 8.0	Carl Zeiss, Jena
ImageJ 1.51	National Institute of Health, Maryland, USA
GraphPad Prism 7	GraphPad Software Inc., La Jolla, CA, USA
MatLab 9.0	MathWorks, Natick, MA, USA

2.2. Chemicals and reagents

Nomination	Supplier
APTES (3-aminopropyl)triethoxysilane)	Sigma Aldrich, Steinheim
Bovine serum albumin (BSA), fraction V, for biochemistry	Merck, Darmstadt
Cholera toxin from *Vibrio cholerae*	Sigma Aldrich, Steinheim
Collagen A (type I collagen)	Biochrom, Berlin
Collagenase IV	Worthington, Lakewood, CA, USA
CRS, Cell Recovery Solution	BD Biosciences, Fernwald
Cryo-SFM	Promo Cell, Heidelberg
DMEM/F12 (1:1) medium GlutaMAX, HEPES	Life Technologies, Darmstadt
EDC ((N-Ethyl-N′-(3-dimethylaminopropyl) carbodiimide hydrochloride	Sigma Aldrich, Steinheim
Epidermal growth factor, human	Sigma Aldrich, Steinheim
$F(ab')_2$ fragment of goat anti-mouse IgG (H+L)	Life Technologies, Darmstadt
Fibronectin, human	BD Biosciences, Fernwald
Formaldehyde, 37 %	Sigma Aldrich, Steinheim
Geltrex™ LDEV-Free Reduced Growth Factor Basement Membrane Matrix LOT: 1819408 (15.4 mg/mL) LOT: 1367663 (15.6 mg/mL) LOT: 1718979 (15.6 mg/mL) LOT: 1911983 (16.0 mg/mL) LOT: 1957341 (16.0 mg/mL) LOT: 1799776 (16.1 mg/mL)	Life Technologies, Darmstadt
Glutaraldehyde EM Grade, 25 %	Ted Pella, Inc., Redding, CA, USA
Glycine	Sigma Aldrich, Steinheim
Goat serum	Sigma Aldrich, Steinheim
HBSS, Hank's Balanced Salt Solution	Life Technologies, Darmstadt
Horse serum	Life Technologies, Darmstadt
Hydrocortisone	Sigma Aldrich, Steinheim
Insulin human recombinant	Sigma Aldrich, Steinheim
KCl (potassium chloride)	Sigma Aldrich, Steinheim
KH_2PO_4 (potassium dihydrogen phosphate)	Sigma Aldrich, Steinheim
Marimastat	Sigma Aldrich, Steinheim
MES (2-(N-morpholino)ethanesulfonic acid)	Sigma Aldrich, Steinheim
Methanol	Merck, Darmstadt
$MgCl_2$ (magnesium chloride)	Sigma Aldrich, Steinheim
Na_2HPO_4 (Sodium hydrogen phosphate)	Sigma Aldrich, Steinheim
$NaBH_4$ (sodium borhydride)	Merck, Darmstadt
NaCl (sodium chloride)	Sigma Aldrich, Steinheim
Penicillin-Streptomycin, liquid, 10,000 U/mL	Life Technologies, Darmstadt
SDS (Sodium dodecyl sulfate)	Sigma Aldrich, Steinheim
Skim milk powder	Sigma Aldrich, Steinheim
Sulfo-NHS (N-hydroxysuccinimide)	Sigma Aldrich, Steinheim
Sylgard®-184 silicone elastomer kit	Dow Corning, Steinfurt
Triton-X-100	Sigma Aldrich, Steinheim
Trypsin-EDTA 0.05 %, phenol-red	Life Technologies, Darmstadt
Tween-20	Sigma Aldrich, Steinheim
Wortmannin	Sigma Aldrich, Steinheim

2.3. Antibodies and fluorescent dyes

Primary antibodies

Isotype	Host	Cat. Nr.	Supplier
Laminin-5 (γ2 chain), mAb, clone D4B5	mouse	MAB19562	Millipore, Billerica, MA, USA
Integrin α6	rat	ab105669	Abcam, Cambridge, UK
Integrin β4 (ERP8559)	mouse	ab133682	Abcam, Cambridge, UK
Collagen IV	rabbit	ab6586	Abcam, Cambridge, UK

Secondary antibodies

Isotype	Host	Conjugate	Supplier
Mouse-IgG	chicken	Alexa Fluor 488	Invitrogen, Karlsruhe
Rat-IgG	goat	Alexa Fluor 405	Invitrogen, Karlsruhe
Rabbit-IgG	donkey	Alexa Fluor 546	Invitrogen, Karlsruhe

Fluorescent dyes and peptides

Product name	Conjugate	Supplier
Alexa Fluor 488 Phalloidin	488	Invitrogen, Karlsruhe
Phalloidin Cruz Fluor 405 Conjugate	405	Santa Cruz Biotechnology, Dallas, TX, USA
NucBlue	DAPI (4′,6-Diamidin-2-phenylindol)	Invitrogen, Karlsruhe
DRAQ5	Far-red fluorescent probe (Ex. wavelength 646 nm)	Thermo Fisher Scientific, Waltham

2.4. Media recipes, buffers and solutions

Media recipes for cultivation of MCF10A cells*

Components	Growth medium (2D)	Assay medium (3D)	EGF-free assay medium (3D)
DMEM/F12, GlutaMAX	ad 500 mL	ad 500 mL	ad 500 mL
Horse serum	5 %	2 %	2 %
Epidermal growth factor (EGF)	20 ng/mL	5 ng/mL	-
Hydrocortisone	0.5 µg/mL	0.5 µg/mL	0.5 µg/mL
Cholera toxin	100 ng/mL	1 ng/mL	1 ng/mL
Insulin	10 µg/mL	10 µg/mL	10 µg/mL
Penicillin/ Streptomycin (10000 Units/mL)	1 %	1 %	1 %
Geltrex	-	2 %	2 %

* According to [33].

CB (Cytoskeleton Buffer), pH 6.1

EGTA	1.902 g/L
Glucose	0.9 g/L
MES	1.95 g/L
$MgCl_2$	0.476 g/L
NaCl	8.77 g/L
Streptomycin	1 g/L

PBS (Phosphate Buffered Saline), pH 7.2

NaCl	8 g/L
Na_2HPO_4	1.15 g/L
KCl	0.2 g/L
KH_2PO_4	0.2 g/L

Blocking buffers

5 % skim milk powder	0.5 g
or	
10 % goat serum	1 mL
CB	ad 10 mL

Dilution buffer

5 % blocking buffer stock	1 mL
CB	ad 10 mL

Fixative solution (3.7 % formaldehyde)

37 % formaldehyde stock	1 mL
CB	ad 10 mL

3D fixative solution (2 % formaldehyde / 0.5 % glutaraldehyde)

37 % formaldehyde stock	0.54 mL
25 % glutaraldehyde stock	0.4 mL
CB	ad 10 mL

Quenching solution for in situ stainings

$NaBH_4$	100 mg
CB	ad 10 mL

Glycine solution, 30 mM

Glycine	0.1126 g
CB	ad 50 mL

Permeabilization solution

Triton-X-100	100 µL
CB	ad 10 mL

Silane buffer pH 4.5-5.5

Water	25 mL
Ethanol absolute	ad 500 mL

Silane solution

APTES	0.5 mL
Silane buffer	ad 10 mL

Coupling buffer, 50 mM MES, pH 6.0

MES	4.88 g
Water	ad 500 mL

Stock solutions Sulfo-NHS and EDC

Sulfo-NHS	20 mg
or	
EDC	20 mg
Coupling buffer	ad 100 µL

Beads activating solution

Coupling buffer	787 µL
10 % SDS	10 µL
FluoSpheres carboxylate	3 µL
EDC stock	100 µL
Sulfo-NHS stock	100 µL

2.5. Substrate preparation

2.5.1. Substrates for 3D cultivation of MCF10A cells

For three-dimensional (3D) cultivation of MCF10A cells (described in 2.6.2), cell culture dishes with a glass bottom were prepared. For that purpose, pre-drilled culture dishes with an outer diameter of 35 mm and an inner hole of 17 mm were used. Coverslips with a thickness of 60-80 µm were glued to the bottom of the dish by means of Sylgard®-184 silicone elastomer kit, with a base to cross-linker mass ratio of 10:1 (specifications of Sylgard®-184 are described in 2.5.2). Beforehand, both components were rigorously mixed for 3 minutes and degassed for 10 minutes by vacuum application. Finally, the dishes with glued coverslips were heat cured at 60 °C for 16 hours.

To sterilize the prepared dishes for cell culture applications, cold plasma treatment was applied. Plasma treatment additionally facilitated subsequent coating by hydrophilizing the coverslips. As process gas, industrial oxygen was applied for three minutes at 70 % power in a plasma oven. Finally, the substrates were coated with Geltrex, a growth factor reduced basement membrane matrix. Geltrex was stored at -80 °C for long term storage or at -20 °C in small aliquots, and thawed overnight at 4 °C before use. Geltrex is viscous at 4 °C, but gels quickly at room temperature, therefore the aliquots were kept on ice and the glass-bottom culture dished were pre-chilled to ease a uniform deposition of a thin Geltrex layer (44 µL/cm^2). Coated dishes were placed into the incubator at 37 °C for 30 minutes to allow gelation of Geltrex.

2.5.2. Substrates for invasion assay

Substrate features and preparation

Polydimethylsiloxan (PDMS) is a biocompatible elastomeric silicone rubber, and was used to produce soft substrates for cell traction analysis on MCF10A acini. Here, Sylgard 184, a two component kit, was used. It consists of a vinyl terminated polydimethylsiloxane as base and a methylhydrosiloxane-dimethylsiloxane copolymer as cross-linker. Depending on the base to cross-linker ratio, it is possible to get an accurately defined substrate elasticity that was characterized as described by Cesa and coworkers [103].

For invasion assays, two different ratios of base and cross-linker were prepared, 50:1 (12 kPa) and 73:1 (0.12 kPa). Both components at indicated ratios were thoroughly mixed with a spatula for 5 minutes. The pre-polymer mixtures were degassed for 10 minutes by vacuum application, as air bubbles which were inevitably introduced into the mixtures during mixing, would change

the mechanical properties of the substrate and negatively affect the transparency of the substrate and lead to insufficient image quality. Subsequently, the not yet crosslinked polymer mixtures were evenly distributed on a coverslip. For that, round coverslips with a thickness of 80-120 µm were used, which were secured by vacuum on the spin-coater chuck. One drop of pre-polymer was applied onto the glass. With linear acceleration of the motor, coverslips were spun at 1,800 rounds per minute for 15 seconds, producing a substrate thickness of 80 µm. By using the mentioned coverslips, an overall substrate thickness of approximately 180 µm was reached. This thickness was close to the optimal requirements of applied objectives, which are optically corrected for a coverslip thickness of 170 µm. In the next step culture dishes with an inner hole of 17 mm in diameter were placed on top of the coated coverslips. Finally, crosslinking of the elastomer was performed at 60 °C for 16 hours, simultaneously the silicone acted as glue. After curing, the substrates displayed a Poisson's ratio of 0.5.

Substrate functionalization for traction force microscopy

After cross-linking, PDMS substrates of defined elasticities were functionalized for traction force microscopy (TFM). For that, fluorescent microbeads (FluoSpheres, carboxylate-modified, 0.2 µm, crimson fluorescent, Thermo Fisher, Waltham, MA, USA) were covalently coupled via carbodiimide EDC/NHS catalyzed reaction to the substrates. Buffers and solutions for this method are listed in Section 2.4, all steps were performed at room temperature.

First, APTES was functionalized via hydrolysis in silane buffer for 120 minutes. Silanization of PDMS was performed by applying 176 µL/cm^2 hydrolyzed silane solution on top of each substrate for exactly 3 minutes. Surplus silane was removed by extensive washing with ethanol. Subsequently, the substrates were vacuum dried for 30 minutes. In the meantime microbeads were re-suspended in the beads activating solution containing SDS to prevent clumping of the beads. Carboxy-groups were activated by adding EDC and sulfo-NHS. The solution was incubated for 15 minutes. Finally, 66 µL/cm^2 of the activated bead solution were applied onto the silanized PDMS surfaces and incubated for 3 minutes to immobilize beads. Excessive beads were removed by three washing steps with distilled water. Functionalized substrates were stored at 4 °C covered with 2 mL PBS until use.

Coating of the substrates for invasion assay

Before MCF10A acini were seeded onto the elastomeric substrates, PBS was removed and the substrates coated either with 600 µL of 20 µg/mL ice-cold Geltrex diluted in PBS or with 600 µL of 20 µg/mL fibronectin, and incubated overnight at 4 °C. Coating of the elastomeric

substrates with an ECM component is required to facilitate cellular adhesion to the substrate by providing appropriate ligands. Shortly before seeding, excess solution was removed.

2.6. Cell culture methods

The human mammary epithelial cell line MCF10A was cultivated under standard cell culture conditions in a humidified environment at 37 °C and 5 % CO_2 supply. MCF10A cells were purchased from American Type Culture Collection (ATCC, Manassas, USA) and maintained in culture as will be described in the following sections.

2.6.1. 2D cultivation and maintenance of MCF10A cells

MCF10A cells were cultivated as a monolayer in 25 cm^2 cell culture tissue flasks, filled with 5 mL growth medium (see Section 2.4). The cells were passaged at a confluence of 75-90 %. For that, the monolayer was washed twice with 10 mL PBS and trypsinized with 0.5 mL 0.05 % trypsin-EDTA solution. As soon as all adherent cells detached from the substrate, the enzymatic reaction of trypsin was stopped by adding 10 mL serum containing growth medium. Cell suspension was centrifuged at 180 *g* for 5 minutes to discard trypsin and cell debris. The cell pellet was resuspended in 10 mL fresh growth medium.

Cell number determination

To ensure experimental reproducibility, determination of the exact cell number was of high importance. An automated cell counter (Moxi-Z-mini) was used to count the cells. A volume of 75 µL of the single cell suspension was loaded into a cassette with electronic current passing through a micro fluidic cell sensing zone (CSZ). Cells passing through the CSZ caused a momentary increase in measured voltage, which was directly proportional to the cell size. Cell number per milliliter was measured and displayed automatically.

One part of the cell solution was used for 3D cultivation of MCF10A cells (described in 2.6.2) and diluted to 5 x 10^3 cells/mL in EGF-free assay medium. For maintenance of cells in culture, 0.5 mL cell suspension were transferred into a new 25 cm^2 flask containing 4.5 mL growth medium.

Cryo conservation of cells

Since continuous cultures are prone to genetic variations, MCF10A cells were maximally maintained in culture up to passage number 20. In order to ensure low passage numbers for all performed experiments, cells were cryopreserved at early stages (P 2-4) in freezing medium and stored in liquid nitrogen. For that, trypsinized and centrifuged cells were resuspended in cryo-SFM medium at a concentration of 1-1.5 x 10^6 cells/mL. Subsequently, the cell suspension was aliquoted into cryovials at 1 mL/vial and placed into a freezing container which provides a cooling rate of -1 °C/min in the -80 °C freezer, thus preventing damage to the cells. For long term storage, cryovials with cells were transferred into liquid nitrogen after 24 hours at -80 °C.

2.6.2. 3D cultivation of MCF10A cells

For 3D cultivation, MCF10A cells were maintained in culture as described in 2.6.1. Following trypsinization, the exact cell number was determined, the cell suspension was diluted to a concentration of 5 x 10^3 cells/mL in EGF-free assay medium and centrifuged at 180 *g* for 5 minutes. The cell pellet was resuspended to a single cell solution in assay medium (see Section 2.4). Three-dimensional cultivation of MCF10A cells was performed according to the previously published protocol [33].

Cells were seeded on top of the Geltrex layer (prepared as described in 2.5.1) at a density of 220 cells/cm^2. Cells were let to settle down and attach to the substrate for 30 minutes in the incubator at 37 °C and were finally covered with 1.5 mL assay medium containing. The day of seeding was set as day 0. Medium was changed every 3-4 days. From day 9 in culture, the assay medium was substituted with EGF-free assay medium for further cultivation. Following this protocol, MCF10A cells formed baso-apically polarized acini with endogenously produced and secreted basement membrane. The basement membrane was deposited by developing acini from day one in culture, and also developed in terms of thickness and stability over the cultivation time. Following this course, acini could be categorized into two developmental groups, depending on the state of the basement membrane (see Figure 2.1). In acini up to day 12 in 3D culture, the basement membrane remained thin. Accordingly this group was termed low-developed basement membrane (ld-BM) acini. From day 13 on in culture, the basement membrane grew thicker and did not change further in thickness from day 20 on. The group with thick basement membrane (from day 20 on) was termed highly-developed basement membrane (hd-BM) acini.

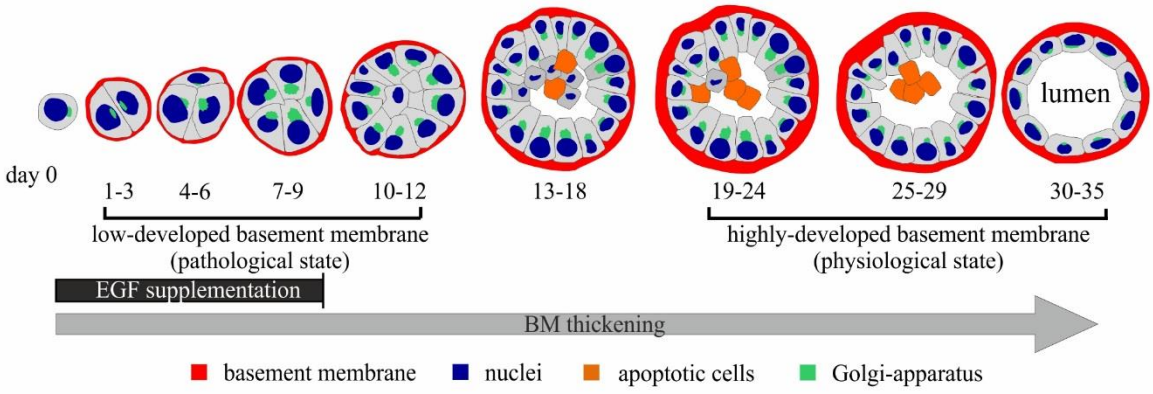

Figure 2.1: Scheme of basement membrane maturation during MCF10A acini growth.
Upon seeding on Geltrex MCF10A cells start to proliferate and form multicellular acini which grow up to day 18 in culture, thereby depositing an endogenous basement membrane (BM). Cellular proliferation is triggered by EGF supplementation during the first 8 days in culture. From day 9 in culture, MCF10A acini are depleted of EGF to initiate luminal clearance. From day 13, luminal clearance starts by apoptosis of the inner cell layer, leading to single-layered epithelial cells with a hollow lumen achieved by day 30 in culture. During differentiation, baso-apical polarity is formed in MCF10A acini which is characterized by the presence of the basement membrane on the basal site and Golgi-apparati facing the apical site of the acini. Up to day 12 in culture, the basement membrane remains relatively thin. Thickening and strengthening of the basement membrane proceeds from day 13 in culture and is reached by day 20 in culture. MCF10A acini are grouped according to the differentiation grade of their basement membrane into low-developed BM (up to day 10 in culture) and highly developed BM (from day 20 in culture) acini. Not to scale, adapted from [33].

2.7. Recovery and transfer of MCF10A acini

For the invasion assays, MCF10A acini were isolated from Geltrex and transferred onto functionalized PDMS substrates (detailed preparation is described in 2.5.2).

During the transfer, it was of high importance not to damage the endogenously produced basement membrane of MCF10A acini. To ensure this, commercially available Cell Recovery Solution (CRS) was used. Geltrex is a gelled matrix which can be dissolved by EDTA-containing agent, such as CRS. CRS dissolves the EHS-substrate without enzymatic digestion (product specification sheet, BD Cell Recovery Solution), thus leaving the BM intact, because the type IV collagen present in the basement membrane is covalently crosslinked [11,104]. The integrity of the basement membrane was proven by immunofluorescent stainings of the basement membrane proteins in transferred MCF10A.

For recovery, acini on Geltrex were washed with 1 mL ice-cold CRS and incubated for 30 minutes at 4 °C in 2 mL fresh CRS. After incubation, CRS was carefully replaced by 1 mL ice-cold EGF-free assay medium. The fragile Geltrex with intact acini on it was vigorously dissolved in medium by pipetting up and down. About 250 µL acini containing solution were

transferred into a new dish while the remaining solution was kept on ice, since dissolved Geltrex would gel again at room temperature. Under a stereo microscope individual acini were manually harvested from the solution using a small pipette and transferred into a new 2 mL micro-centrifuge tube, treated for minimizing protein binding. This tube contained 200 µL fresh ice-cold EGF-free assay medium. As soon as all acini were collected, they were again transferred into a petri dish and harvested in a second round under the stereo microscope, simultaneously concentrated in a small media volume of 20 µL and finally transferred onto the functionalized elastomeric substrate. Acini were let to attach to the substrate for 10 minutes and then covered with 4 mL medium (see Section 2.7.2).

2.7.1. 3D *in vitro* invasion assay of MCF10A acini to investigate basement membrane transmigration

To investigate the influence of tumor-associated ECM stiffening on invasive potential of MCF10A acini at different basement membrane developmental states and the role of the basement membrane as a potential invasion barrier, a novel 3D *in vitro* invasion assay was developed. On the basis of the established 3D protocol for cultivation of MCF10A cells (see Section 2.6.2), in this work the basement membrane was classified into two developmental stages: low developed basement membrane (ld-BM, 10 days old acini) and highly developed basement membrane (hd-BM, 20 days old acini). For invasion assay, ld-BM acini were chosen to recapitulate a pathological breast acini state with a weak basement membrane, while hd-BM acini represented the physiological basement membrane state in healthy mammary gland.
The time course of the invasion assay is schematically shown in Figure 2.2.

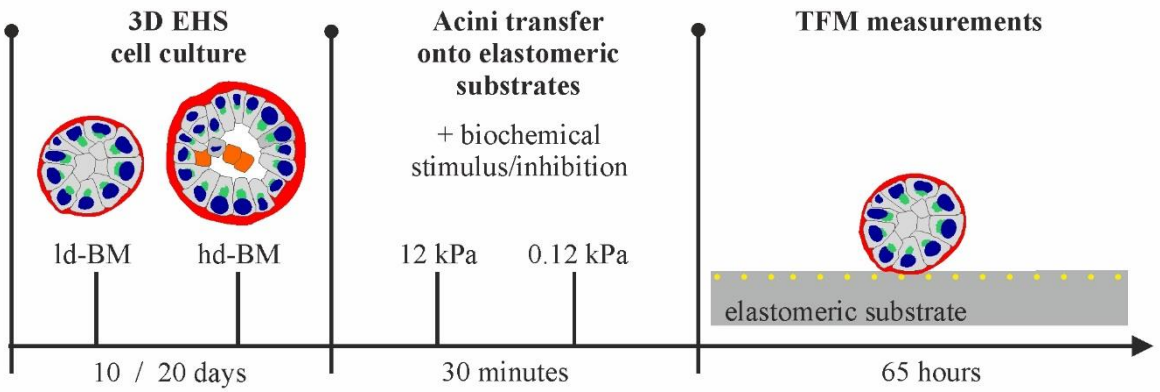

Figure 2.2: Scheme of the 3D *in vitro* invasion assay.
For invasion assay, ld-BM and hd-BM MCF10A acini were isolated from Geltrex and transferred onto elastomeric substrates of two different elasticities of 0.12 kPa and 12 kPa. Depending on the experimental question, acini were stimulated with proliferative factors promoting basement membrane disruption and invasion or with respective inhibitors. Behavior of MCF10A acini was observed over a period of up to 65 hours.

For analyses, ld-BM and hd-BM MCF10A acini were recovered from Geltrex (as described in 2.7) and transferred onto functionalized PDMS substrates (see Section 2.5.2) of two different elasticities: 0.12 kPa (representing normal breast elasticity) and 12 kPa (representing tumor stroma stiffness) to analyze acinar invasive behavior on different matrix rigidities and to measure tractions produced by MCF10A acini during the invasion. The time of acini transfer was set as 0. From this time point on, acini were analyzed for 65 hours. Thereby the time needed for incubation and microscope setting preparations was subtracted from the overall analysis time of 65 hours.

Initially, to investigate only the influence of substrate rigidity on acini, invasion experiments on MCF10A acini were performed using EGF-free assay medium. Invasion events were analyzed by phase contrast microscopy. The time point when the first cellular outline was visible protruding from the acinus, was noted and assigned as invasion onset. Furthermore, the assay allowed to biochemically manipulate the state of the basement membrane. The detailed application procedure and used drugs are described in the next section.

2.7.2. Biochemical treatments of the basement membrane

Following invasion experiments on MCF10A acini with EGF-free assay medium, biochemical manipulations of acini were performed. In order to either stimulate or inhibit cellular transmigration through the BM by invasion relevant biochemical factors:

Epidermal growth factor stimulation

EGF was used to trigger cellular proliferation and initiate invasion. For that growth medium containing 20 ng/mL EGF was used. MCF10A acini were covered with this medium directly after the transfer and kept in it during the entire investigation time.

Collagenase type IV treatment

Collagenase type IV, a specific type IV collagen digesting enzyme, was used to weaken the basement membrane by proteolytic digestion to investigate the impact of structural integrity of the basement membrane as a barrier for acinar invasion. MCF10A acini recovered from Geltrex were incubated in HBSS buffer containing 290 U/mL collagenase type IV at 37° C for 30 minutes, based on previously published results [33]. Subsequently, MCF10A acini were transferred onto PDMS substrates, left to settle down, shortly washed with growth medium to remove the remaining collagenase type IV, and covered with 4 mL fresh growth medium that was retained on MCF10A acini over the whole investigation time.

Marimastat

Marimastat is a broad-spectrum matrix metalloproteinase (MMP) inhibitor. It was used to inhibit MMPs in order to investigate their role as possible degrading enzymes of the basement membrane. MCF10A acini were covered with medium containing 20 µM marimastat directly after the transfer onto the PDMS substrates (adopted from [105]). This medium was left on MCF10A acini over the whole investigation time.

Wortmannin

Phosphoinositide 3-kinase (PI3K) mediates signal transduction of extracellular stimuli and regulates different cellular mechanisms, such as survival, membrane transport and cell migration [106]. Wortmannin is a PI3K inhibitor and was used to inhibit PI3K-mediated cascades responsible for cell invasion. MCF10A acini were first transferred onto the PDMS substrates and covered by growth medium containing 25 nM wortmannin. The samples were incubated at 37 °C for 1 hour (adapted from [107]). Afterwards, the medium was replaced by fresh growth medium which was left on MCF10A acini over the further investigation time.

In Table 2.1 experimental conditions, the used media and chemical drugs, as well as the applied concentrations are summarized.

Table 2.1: Overview of conditions used in invasion assays, including media and biochemical manipulators.

Treatment	Medium	Drug	Concentration
1[#]	EGF-free AM	- EGF	-
2[#]	EGF-free AM	- EGF + Marimastat	- 20 µM
3	GM	+ EGF	20 ng/mL
4	GM	+ EGF 20 mg/mL + Collagenase IV	20 ng/mL 290 U/mL
5	GM	+ EGF + Marimastat	20 ng/mL 20 µM
6	GM	+ EGF + Wortmannin	20 ng/mL 25 nM

[#]: These experiments were partially performed and evaluated by the coworker Julian Eschenbruch (ICS-7, Forschungszentrum Jülich). AM: assay medium, GM: growth medium.

Treatments 1 and 3-5 were performed on 0.12 kPa and 12 kPa stiff substrates with ld-BM and hd-BM MCF10A acini. Treatments 2 and 6 were performed only on 12 kPa stiff substrates and only with ld-BM acini, respectively. Condition 4 was performed only on 0.12 kPa stiff substrates and only with hd-BM acini. All experiments were performed in triplicates. In general 24-29 MCF10A acini were analyzed per experiment. In each experiment one cell-free position without an acinus was imaged to determine the noise value or possible artefacts produced by the experimental settings.

2.8. Traction force microscopy (TFM)

Traction force microscopy (TFM) was pioneered by Harris, Wild and Stopak in 1980 who showed that fibroblasts are able to form folds of an elastic sheet to which they adhere [108]. During the next decades, this method was further developed and improved by introducing a non-wrinkling substrate (silicone rubber with embedded beads), bonded to glass coverslips [109,110]. During last decades, TFM has become a powerful and very popular tool to retrieve cell forces applied to the substrate. In general, this method describes tangential deformations (x- and y-directions) of a continuous, linearly elastic substrate, exerted by a cell which adheres to the substrate [111,112]. Thereby, a cell is attached to an elastic substrate with incorporated fluorescent microbeads as markers to track substrate displacements generated by cellular tractions. This condition is recorded by imaging. To get a reference of the non-deformed state of the substrate, the cell is removed and the recovered substrate is imaged again. Knowing

the mechanical properties of the substrate, measured deformations can be converted into traction forces generated by cells [111,113].

TFM was originally developed to analyze single cells. Nowadays however, research is increasingly focused on multicellular cluster, representing more physiological models which are naturally more complicated than single cells. In contrast to single cells, cells in a multicellular system form not only cell-matrix contacts, but also cell-cell contacts, making the calculations for traction recovery complicated [113]. Butler and colleagues introduced the concept of strain energy, which is another measure of contractile strength that is defined as total energy transferred to the elastomeric substrate by the cell [114] and is applicable to multicellular systems.

2.8.1. Experimental setup and procedure

Life cell analyses were performed using an Axio Observer Z1 and an EC Plan-Neofluar 40x/1.30 Oil Ph3 objective. Cell culture conditions (37 °C and 5 % CO_2) were sustained during the whole experiment by means of the thermostated incubation chamber. Image acquisition was performed using ZEN 2.3 blue edition software.

Samples with transferred MCF10A acini were mounted onto the motorized stage of the microscope. To exclude thermal drift, samples were left to equilibrate to the incubation temperature of 37 °C for a minimum of 30 minutes. During this time positions containing acini were marked and settings adjusted. Per experimental setup, 24-29 positions containing acini and an acinus-free position were chosen. To catch the invasion process of MCF10A acini and the produced substrate deformations, the field of view around the analyzed acini was increased by creating a tile scan by applying 9 tiles (3 x 3) in total, with a single acinus placed in the central tile. Images with a pixel size of 0.158 x 0.158 µm (image size: 63981 x 38061 pixels) and an overlap of 10 % were taken, leading to a full image size after stitching of around 610 x 458 µm.

MCF10A acini were analyzed in phase contrast. At the same time the fluorescence of the beads was excited using the HXP-120 light source, by a wave length of 605 nm and selected by the appropriate filter set 64 HE. The beads channel was assigned as reference channel for autofocus strategy to keep the beads in focus during the multi-position long term measurements. Images were taken at 20 minutes intervals for up to 65 hours, depending on equilibration time that was substituted from the total time of 65 hours.

2.8.2. Image processing and data analysis

To stitch all nine tiles to one large image, a *MacroStitchingTool2* implemented in ImageJ was used [115]. This stitching tool was applied only to the nine tiles of the first time point. For stitching, the beads channel was used. The image tiles of the phase contrast channel were stitched using the coordinates from the beads channel. The resulting stitching parameters were saved and used for stitching of the tiles at further time points applying a MatLab based program *CellClusterStitchingTool* developed at the ICS-7 institute by Dr. Ronald Springer. In this program each tile was individually drift corrected over time. Subsequently, these tiles were stitched using the previously saved parameters. The time points of both channels were stacked to two individual image sequences.

The produced image stacks were further used to determine bead displacements according to previous publications [111,116]. For this, the custom developed program *CellForceAnalysis* (MatLab based, developed at the ICS-7 institute by Dr. Ronald Springer) was used. The first image of the beads channel was utilized as reference image. A manually marked region around a randomly chosen bead was defined as template (see Figure 2.3 A). This template was cross-correlated with the image to localize all other beads [117] (see Figure 2.3 B). Only positions where the normalized cross-correlation coefficient exceeding a threshold of 0.8 were accepted as bead positions. Prior to force retrieval, drift was determined from the average shift of the beads in areas located in cell free areas (see Figure 2.3 C).

For determination of contractile forces, the algorithm described by Houben and colleagues was applied [117]. To visualize tractions produced by MCF10A acini, the force application region was marked by a circle around the acini in the phase contrast image stacks (see Figure 2.3 D). The displacement of each bead in subsequent frames was determined with respect to the reference image (see Figure 2.3 E). Finally, contractile strength was calculated and displayed as stress in $nN/\mu m^2$ (see Figure 2.3 F). For a better comparison, the determined cellular tractions were further converted into strain energy and given in fJ [114].

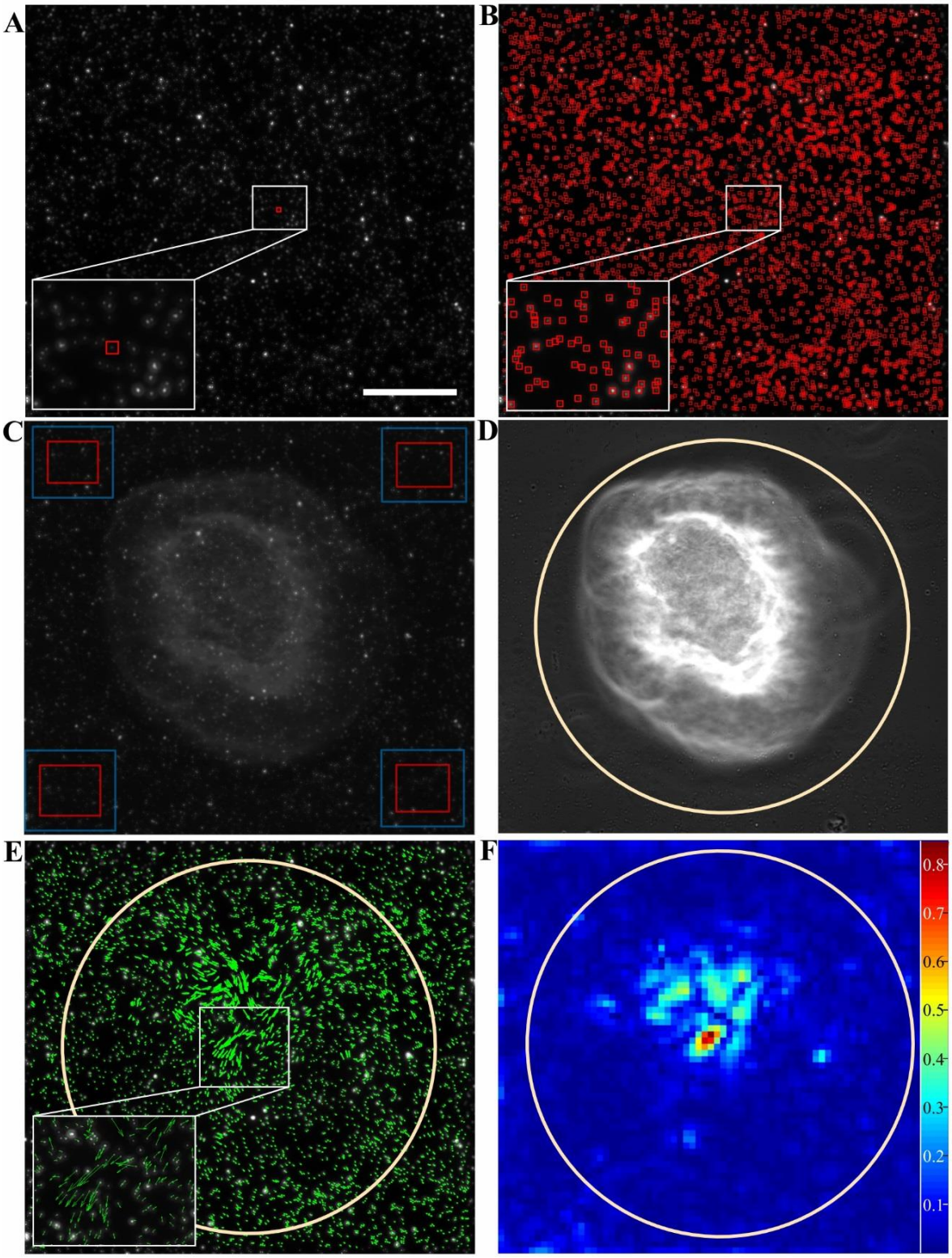

Figure 2.3: Workflow of image processing during cell traction analysis.
A. The first image frame of the beads channel was used to mark a single, randomly chosen bead by a rectangle. Scale bar = 50 µm. **B.** In the next step, all other beads were found by applying the cross-correlation algorithm to the whole image. **C.** Cell free areas were marked to determine the drift from the average shift of the beads in these areas. **D.** The region of interest was marked by a circle around the acinus in which cell tractions were calculated. **E.** The displacement of the beads was determined in all image frames over time with respect to the first image as reference. **F.** Shear stress applied by cells to the substrate. Heat map is given in [nN/µm^2].

2.9. Elastic Resonator Interference Stress Microscopy (ERISM)

In contrast to the well-established TFM, Elastic Resonator Interference Stress Microscopy (ERISM) is a novel approach with a quite different focus. While TFM can easily track in-plane displacements, this method has a limited sensitivity to vertical forces (z-axis) [118,119]. By using optical interference on a thin deformable substrate, ERISM can measure extremely weak mechanical forces produced by cells in a vertical direction during migration, as cells extend small protrusions to probe their environment. However, ERISM has a limited sensitivity to tangential forces. The general element of ERISM is an elastic, optical micro-cavity consisting of an elastomer spaced between two semitransparent gold mirrors (see Figure 2.4 A). Illumination of the substrate with monochromatic light leads to reflection on the cavity and interference of light. Any changes in cavity thickness produced by adherent cells are observed as interference fringe patterns (see Figure 2.4 B and C). Using the reflection spectra from each image stack, the cell-induced vertical displacements are calculated by an algorithm and visualized as a heat map (see Figure 2.4 D). Thereby the unchanged thickness of the micro-cavity is used as internal reference to determine substrate displacements [118,119]. ERISM represents a method sensitive enough to measure substrate deformation produced by small cellular protrusions like filopodia or invadopodia.

In this thesis, ERISM measurements were performed in cooperation with Dr. Nils Kronenberg and Prof. Malte Gather from the University of St Andrews, SUPA, School of Physics and Astronomy, UK, according to the protocol published elsewhere [118].

For the ERISM analysis, MCF10A ld-BM and hd-BM acini were recovered from Geltrex (as described in section 2.7) and transferred onto the elastic (siloxane-based) optical micro-cavity sandwiched between two thin semi-transparent gold layers. The ERISM chips with an elastic modulus of 3 kPa were coated with type I collagen overnight and washed with medium prior to acini transfer. Measurements were performed for up to 30 hours at different intervals, ranging between 2 and 20 minutes. The experiments were performed in triplicates for both ld-BM and hd-BM groups. Microscopy and data processing were performed by Dr. N. Kronenberg (University of St Andrews).

MCF10A acini were identified by phase contrast microscopy as shown in Figure 2.4 E. Micro-cavity reflection was imaged under illumination with monochromatic light of 201 different wavelengths between 550 nm and 750 nm. Local deformations induced by MCF10A acini created a fringe pattern which provided a direct measure of substrate deformation (see Figure 2.4 F).

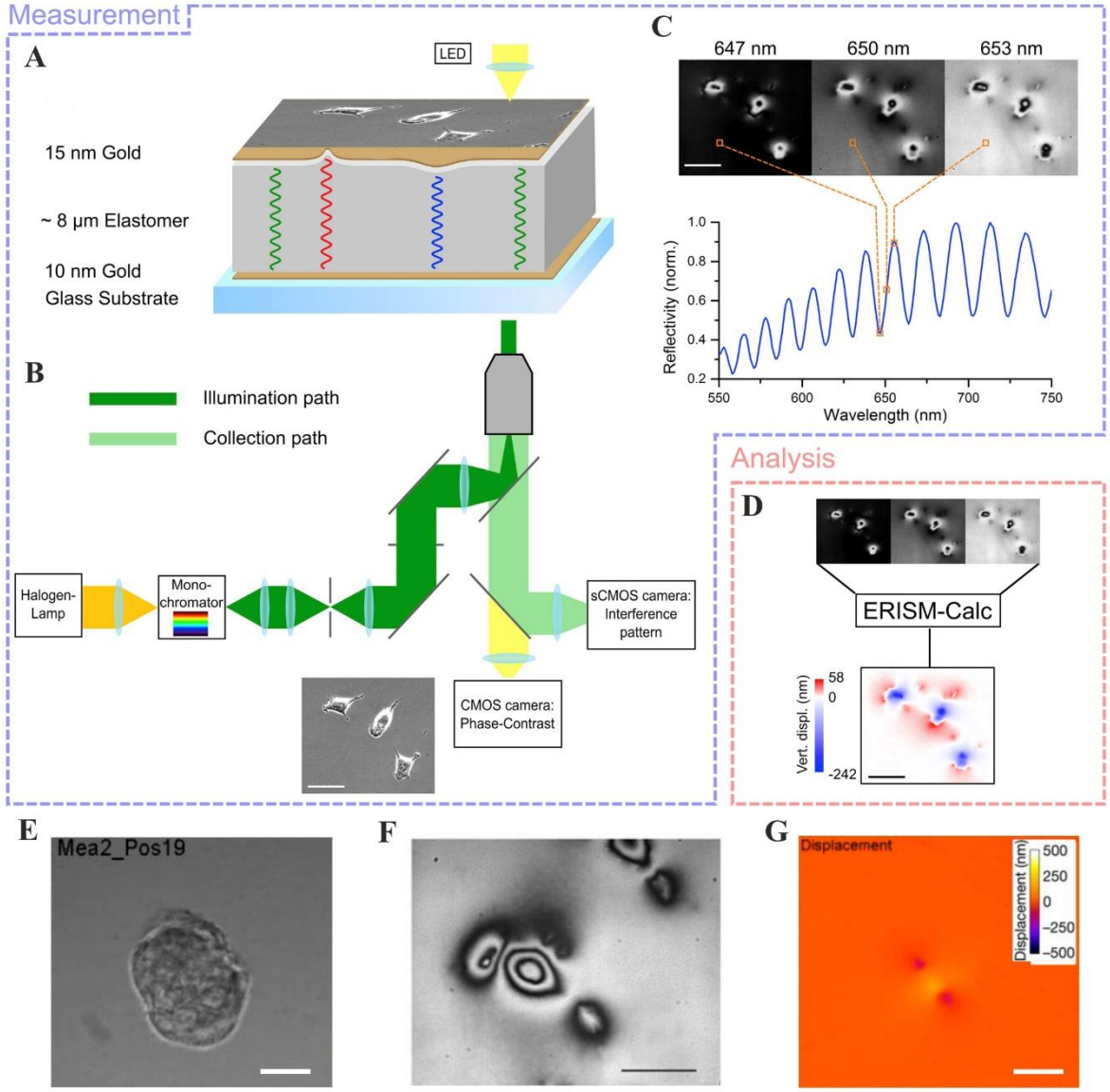

Figure. 2.4: Principle and workflow of Elastic Resonator Interference Stress Microscopy. **A.** Cells are imaged on a micro-cavity consisting of an elastomer spaced between two semitransparent gold mirrors. **B.** The sample is illuminated from underneath with monochromatic light from a monochromator using a halogen lamp. The reflectivity is recorded by an sCMOS camera, while simultaneously phase contrast images are recorded on a separate CMOS camera. **C.** Reflection images at designated wavelengths showing fringe patterns produced by adherent cells. **D.** Using the reflection spectra, the ERISM-Calc software calculates the cell-induced displacements. Scale bars = 50 µm. **E.** Phase-contrast image of an MCF10A acinus on the micro-cavity surface. Scale bar = 25 µm. **F.** Co-registered monochromatic reflectance image of a micro-cavity at 655nm wavelength of illumination (not from the acinus in E). Scale bar = 50 µm. **G.** ERISM map obtained from the reflectance data, showing deformation induced by the MCF10A acinus from **E**. Scale bar = 25 µm. Figure modified from [118,119].

The reflectance was analyzed as a function of wavelength for each pixel. To obtain the acini-induced substrate deformation, a background plane was subtracted from the measured thickness

map. Finally, the acini-induced deformations were displayed in the ERISM maps (Figure 2.4 G). To visualize the structures more clearly, broad features of substrate deformations were removed via spatial Fourier filter, with a lower cutoff of 10 pixel and an upper cutoff of 3 pixel. The pixel size was 0.162 µm using a 40x objective, and 0.324 µm using a 20x objective.

2.10. Immunocytochemistry

MCF10A acini were immunocytochemically stained either *in situ* (on Geltrex) or transferred onto a glass bottom dish with a high precision coverslip, 170 ± 5 µm in thickness, as described in 2.7. An overview of solutions used for immunocytochemical stainings is given in 2.4. Antibodies and fluorescent dyes used are listed in 2.3. All steps were performed at room temperature, unless otherwise stated.

Samples were washed with 2 mL CB. Acini *in situ* were fixed with 1 mL 3D fixative solution for 20 minutes and subsequently quenched with 2 mL freshly prepared $NaBH_4$ solution, two times for 5 minutes. Glutaraldehyde is a much stronger fixating agent than formaldehyde and was required to ensure a firm fixation of Geltrex.

Transferred acini were fixed with 1 mL 3.7 % formaldehyde for 20 minutes and quenched with 2 mL glycine solution for 5 minutes.

After quenching, the following steps were identical for all samples. Permeabilization of cellular membranes was done by treatment with 1 % Triton-X-100 solution in CB (see Section 2.4), for 10 minutes in ld-BM and for 20 minutes in hd-BM acini. Before antibodies were applied to the samples, a blocking step was performed to prevent unspecific antibody binding. Samples were incubated with 2 mL blocking buffer containing 1 % goat $F(ab')_2$ anti-mouse IgG fragment for 2 hours. Afterwards, primary antibodies were applied to the samples in 200 µL dilution buffer and incubated for 16 hours at 4 °C. On the following day samples were washed three times with 2 mL CB for 5 minutes each washing step. Subsequently, secondary antibodies were applied in 200 µL dilution buffer for 45 minutes in darkness. For staining of F-actin fluorescently labeled phalloidin was applied simultaneously with secondary antibodies. Afterwards, samples were washed two times with 2 mL CB. Finally, cell nuclei were counterstained with DRAQ5 or NucBlue for 10 minutes. Samples were covered with 2 mL CB and analyzed by confocal laser scanning microscopy or stored at 4 °C until analysis.

2.11. Confocal Laser Scanning Microscopy

For visualization of immunocytochemically labeled structures in MCF10A acini, confocal laser scanning microscopes cLSM 710 and cLSM 880 were used.

The advantage of cLSM is that a thick specimen like an MCF10A acinus can be imaged by thin optical sectioning. Thereby the fluorescent light is projected onto a pinhole diaphragm in a way that no other light that is out-of-focus can pass through the pinhole and reach the detector.

The used microscopes consist of a motorized inverted microscope base (Axio Observer Z.1) and are equipped with a diode, argon-ion (Ar+), and helium-neon (HeNe) lasers, providing the excitation wavelengths of 405 nm, 458/488/514 nm, 543 nm (LSM 710) or 561 nm (LSM 880), and 633 nm, respectively.

The excitation light was separated from the emitted light by a main beam splitter (405 nm, 488/543/633 nm on LSM 710, or 488/561/633 nm on LSM 880). The emitted fluorescence light of Alexa Fluor 405 was analyzed using the 410-495 nm wavelength band-pass filter, Alexa Fluor 488 was analyzed with the suitable 505-520 nm wavelength band-pass filter, Alexa Fluor 546 with 550-615 nm (LSM 710) or with 565-610 nm (LSM 880) wavelength band-pass filter. For a better visualization of the images shown in this thesis, brightness and contrast of the immunofluorescent images were increased afterwards.

2.12. Statistical analyses

Statistical analyses were performed using the software GraphPad Prism 7. The mean values of the invasion onsets were compared using the Tukey's multiple comparison test. Mean values with 95% confidence interval were plotted. Mann-Whitney-Test was used to compare the strain energy values measured by TFM, and for comparison of the displaced volume measured by ERIM. Median values with 95 % confidence interval were plotted.

Confidence interval of a proportion was determined for incidence of invasive acini, using the Two-Proportions Z-Test. This analysis was performed using MatLab 9.0 software.

For all tests the significance was assessed as following: * = $p < 0.05$, ** = $p < 0.01$, *** = $p < 0.001$, **** = $p < 0.0001$. In case of $p > 0.05$ the difference was assessed as not significant (n.s.).

3. Results

The aim of this thesis was to investigate the human mammary gland basement membrane barrier function against invasive cells. For this purpose a tailored 3D *in vitro* invasion assay using the non-tumorigenic MCF10A acini as cell culture model system has been developed. Besides the possibility to monitor the invasion process of MCF10A acini in real time under normal and progressive tumor resembling conditions, this novel invasion assay additionally enabled simultaneous measurement of the mechanical stress that is applied by MCF10A acinar cells to the elastomeric substrates (ECM) during invasion.

3.1. MCF10A acini as reliable 3D *in vitro* model

MCF10A cells are classified as a non-invasive mammary epithelial cell line [99] which is approved under physiological 3D cell culture conditions, as these cells form fully differentiated acini with baso-apical polarity, recapitulating the 3D spherical organization of a mammary gland acinus *in vivo* [100].

When cultured on Geltrex according to the previously published protocol [33], MCF10A cells formed baso-apically polarized acini with endogenously produced and secreted basement membrane. Depending on the cultivation time, the basement membrane showed two distinct developmental stages. Up to day 10 in culture the basement membrane was thin and was therefore designated as low-developed basement membrane (ld-BM). From day 20 in culture, the basement membrane was thick and therefore designated as highly-developed (hd-BM).

To display the presence of two developmental states of the basement membrane, the allocation of well-established basement membrane marker proteins, type IV collagen and laminin-332 was shown (see Figure 3.1). Those marker proteins in general showed a homogeneous distribution of the basement membrane around the acini at both developmental stages. In ld-BM acini the signal of the basement membrane appeared to be relatively poor and diffuse, directly compared to the smooth and bright basement membrane present in hd-BM acini. In ld-BM acini, the staining of the basement membrane was very weak, resembling the pathological basement membrane, while in hd-BM acini the stainings were very strong and continuous, representing the physiological basement membrane.

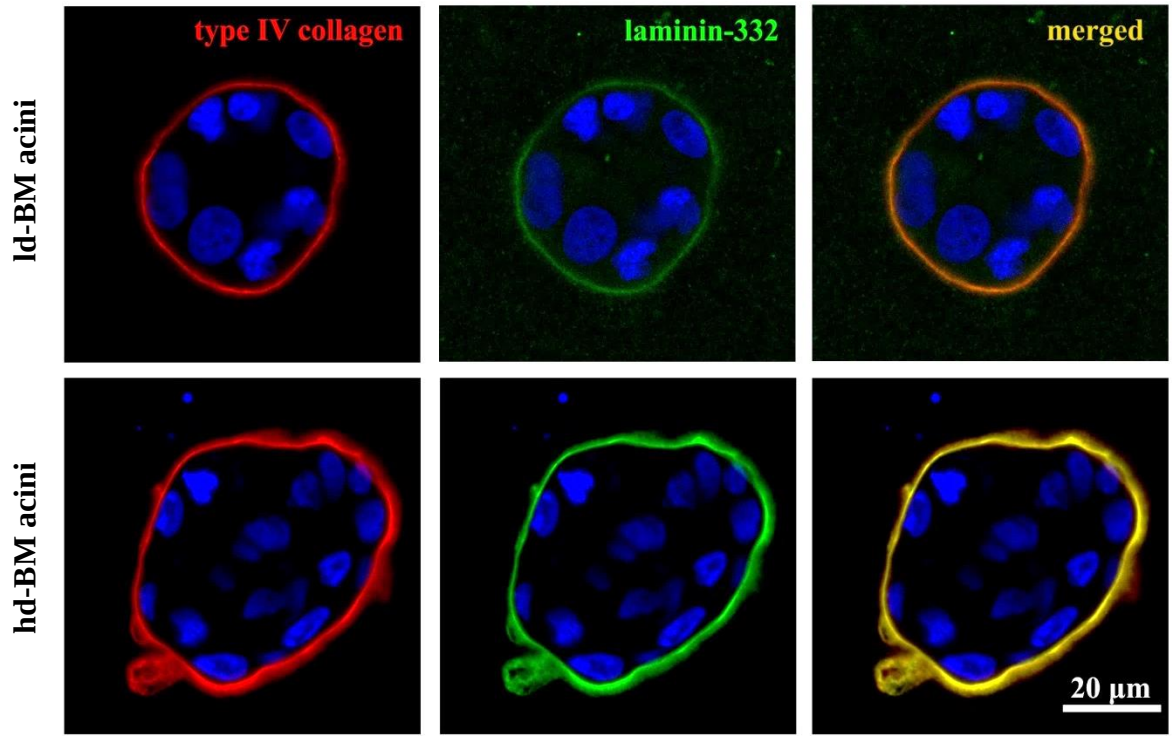

Figure 3.1: Basement membrane maturation in MCF10A acini.
Cross-sections through ld-BM and hd-BM MCF10A acini. Representative immunofluorescent stainings of two main structure lending basement membrane proteins type IV collagen (red) and laminin-332 (green). The overlay of both signals (yellow) indicates their co-localization as functional basement membrane. The cell nuclei were counterstained with DAPI (blue). Scale bar = 20 µm.

3.2. Initiation of an invasive phenotype in MCF10A acini

During cancer progression, altered growth factor signaling can lead to malignancy, such as loss of cellular polarity during EMT. In turn, malignant cells can activate tumor stroma, leading to increased stiffening of the ECM [51]. Increased matrix stiffness in combination with altered growth factor signaling can further promote cancer progression by initiating degradation of the basement membrane [12,68], can increase cellular motility as well as invasiveness through increased focal adhesion assembly and lead to generation of larger forces [68,74,79]. This complex reciprocity raises the question whether it is possible to induce an invasive phenotype in the non-tumorigenic MCF10A acini by altering environmental factors that are known to induce malignancy. To answer this question, factors promoting invasive phenotype were applied to MCF10A acini.

Since MCF10A acini were demonstrated to have a developmental state in which the basement membrane is relatively thin (see Figure 3.1), this group (ld-BM acini) was chosen to represent

the pathological state of the mammary gland *in vivo* with a weakened or not fully-matured basement membrane [120]. The presence of a tumor-like stiffened ECM, as found *in vivo*, was resembled by the elastomeric substrate with a Young's modulus of 12 kPa [58]. Additionally, to affect and alter the tumor-associated EGFR signaling cascades, biochemical tumor microenvironment was simulated by aberrant EGF stimulation.

For investigation, ld-BM MCF10A acini were recovered from their 3D EHS matrix, transferred onto elastomeric substrate with a stiffness of 12 kPa, and stimulated with EGF-containing growth medium. The process was imaged by phase contrast microscopy for up to 65 hours to analyze acinar behavior under this tumor resembling condition. Directly after the transfer of MCF10A acini onto the elastomeric substrate, acini adhered, but did not remain static. Instead, the cells in single acini seemed to be in a constant movement, resulting in a kind of rotation on the spot (see Figure 3.2 A-A``). This behavior was designated as the rolling phase. Individual acini remained in this phase for a different durations of time. Following this initial rolling phase, the behavior of MCF10A acini could be categorized into two distinct fractions: One fraction remained in the rolling phase over the whole observation time of 65 hours, while the other fraction showed invasive migration, including BM transmigration and subsequent cell dissemination on the substrate. At some point, in this invasive acini fraction, cellular outlines protruding from the acini could be observed (see Figure 3.2 B). This time point was defined as the invasion onset. These cells, initially visible as outlines, finally escaped from the acinus and were followed by further cells which disseminated on the substrate (see Figure 3.2 C). After 65 hours, most of the invasive acini lost their 3D spherical appearance and showed a monolayered growth pattern (see Figure 3.2 D).

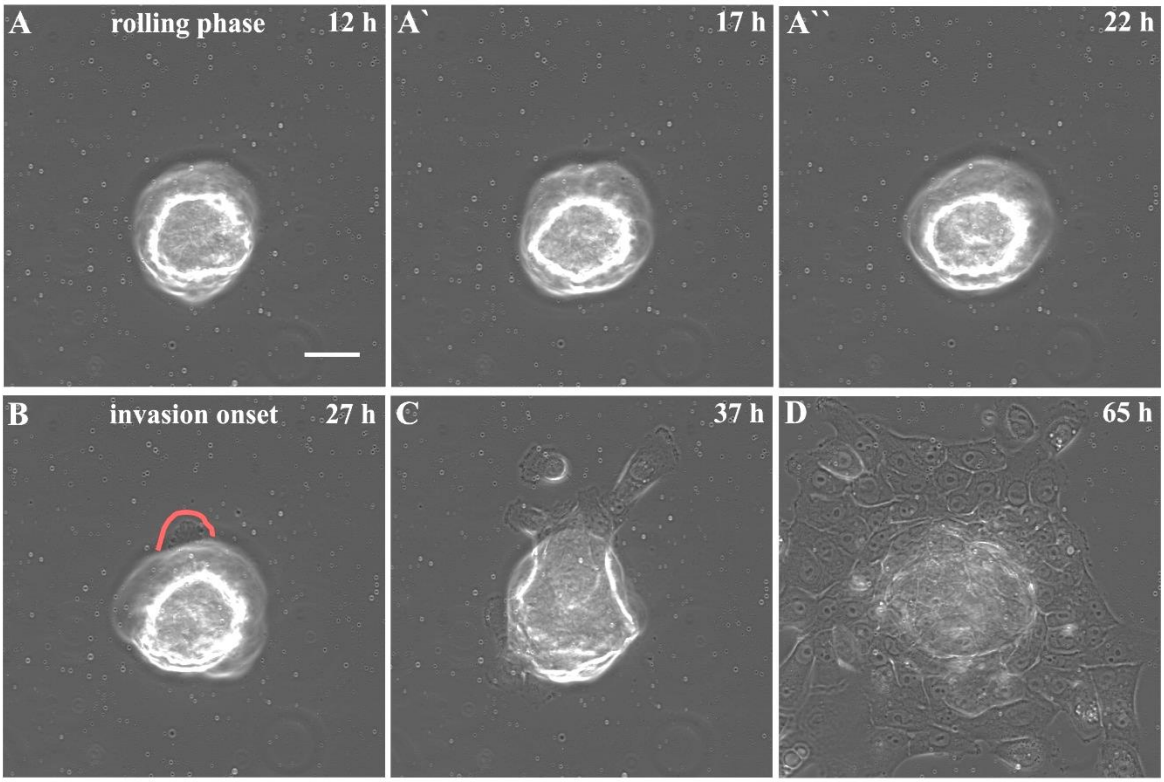

Figure 3.2: Invasive phenotype of MCF10A acini.
Ld-BM MCF10A acini on 12 kPa elastomeric substrate, stimulated with 20 ng/mL EGF, were analyzed in phase contrast. An image sequence of a representative invasion pattern is shown. **A-A``.** MCF10A acinus in the rolling phase, between 12 hours after the transfer and 5 hours prior to invasion. **B.** After 27 hours on the substrate first cellular outline (red curb) was observed. This time point was defined as "invasion onset". **C.** The first cell escaping from the acinus was followed by further cells, which collectively invaded the substrate. **D.** By the end of the measurement (65 hours) disseminated cells formed a monolayer. Scale bar = 50 µm.

To visualize the acinar characteristic appearance during EGF induced invasion, MCF10A acini were fixated at different invasion stages and immunocytochemically stained (see Figure 3.3). Interestingly, immunofluorescent staining of F-actin and type IV collagen at an early stage of invasion revealed the presence of thin cellular actin-rich protrusions (see Figure 3.3 A). These protrusions seemed to reach through the pores of the basement membrane (see Figure 3.3 A, zoom-in, white arrows). As the invasion proceeded, several cells were visible leaving the acinus through the basement membrane scaffold (see Figure 3.3 B, white stars). At this stage the basement membrane was predominantly found surrounding the acini, but was locally disrupted by the invading cells (see Figure 3.3 B`). At the late stage of acinar invasion, the spherical structure of acini disappeared, leaving a monolayer of cells disseminated on the substrate. Residuals of fragments of the basement membrane could be found around the cellular monolayers (see Figure 3.3 C). Here staining of integrin α6, a hemidesmosomal marker (baso-apical polarity marker), which is normally localized to the basement membrane, was shown to

be distributed in the cell membrane, indicating the disruption of baso-apical polarity during the late stage of invasion. To prove the presence of α6 integrin subunit at the hemidesmosomes, a co-staining of α6 and β4 integrins was performed in hd-BM MCF10A acini (see Figure 3.3 D). Both integrin subunits showed co-localization at the site of the basement membrane, surrounding MCF10A acini.

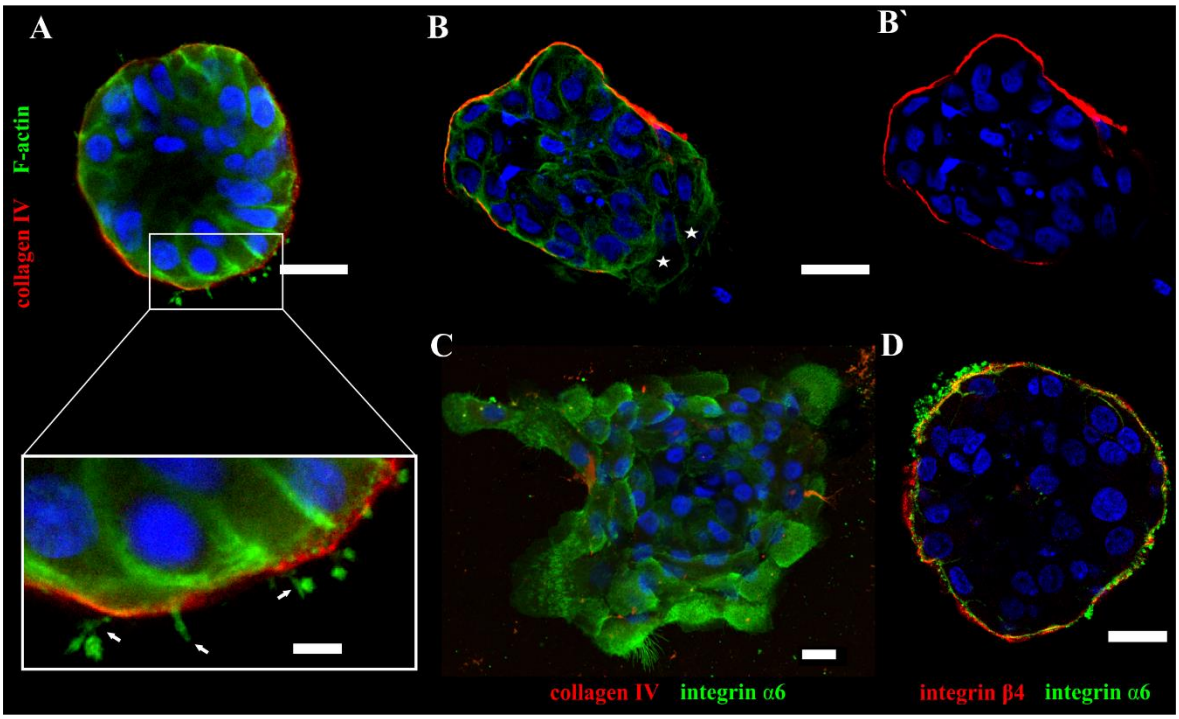

Figure 3.3: Morphology loss of MCF10A acini during basement membrane invasion.
Representative immunofluorescent stainings of MCF10A acini on tumor-like stroma stiffness (12kPa) are shown at different stages of the invasion progress. **A.** MCF10A acinus with ld-BM (type IV collagen, red) in the rolling phase. Zoom-in: small finger-like actin-rich protrusions (green, marked by white arrows) are visible, reaching through the pores of the basement membrane (red). **B.** Invasive ld-BM acinus with locally invading cells (white stars). F-actin is shown in green, basement membrane is shown in red (type IV collagen). **B`.** The acinus still retained its spherical shape. The basement membrane (red) was not continuous, but locally disrupted by invading cells (shown in B). **B and B`.** Raw image kindly provided by the coworker J. Eschenbruch, (ICS-7). **C.** Late phase of ld-BM acinar invasion. The acinus already lost its spherical structure and the cells spread on the substrate, forming a monolayer. Basement membrane residues (type IV collagen, red) were detected around the monolayer. Integrin α6 (green) was distributed in the cell membrane. Under normal conditions, integrin α6 (green) and integrin β4 (red) were found to be co-localized in hemidesmosomes, connecting the cells to the basement membrane, as was visualized in **D** in an hd-BM acinus. Cell nuclei were counterstained with DRAQ5 (A and D) or DAPI (B and C), blue. Scale bars = 20 µm, zoom-in = 5 µm.

Interestingly, these initial experiments demonstrated that originally non-tumorigenic, well-structured MCF10A acini could be efficiently triggered toward a highly invasive phenotype. Loss of spherical structure, local BM disruption and collective cell migration have

been shown to be inducible by exerting tumor resembling biochemical and biomechanical cues to breast gland acini *in vitro*. This led to the question, to what extent the here applied tumor promoting factors contributed individually to the invasion onset. Therefore, a suitable invasion assay was established and used to systematically analyze the influence of the invasion-relevant factors, such as the state of the basement membrane, ECM stiffness and EGF stimulation.

3.3. Establishment of tumor progressing scenarios for the invasion assay

In vivo, basement membranes are often found to be perturbed or weakened in epithelial cancers [120]. The reproducible ability to generate two developmental states of the basement membrane in MCF10A acini (see Figure 3.1) allowed *in vitro* analyses of two clinically distinct states of the basement membrane.

For the following experiments, ld-BM acini were chosen as model for the pathological state of the mammary gland with a weakened basement membrane, while hd-BM acini were chosen model for the physiological state in healthy breast with a fully matured and structure lending basement membrane scaffold. These characteristics of MCF10A acini made those cells a suitable model system for the following studies on invasion and physical properties of the basement membrane in health and disease.

Additionally, the stiffening of the ECM could be simulated using elastomeric substrates of different elasticities. To mimic normal and tumor tissue elasticities, elastomeric silicone rubber substrates with Young's moduli of 0.12 kPa, corresponding to normal-like stroma [56] and 12 kPa, corresponding to tumor-like stroma [51,58] were chosen, respectively.

Combinations of the mentioned parameters were hypothesized to give rise to the formation of four global groups displaying distinct mechano-biological states of the mammary gland (see Figure 3.4), ranging from the most physiological state with hd-BM acini on normal-like stroma (0.12 kPa) to the most pathological group with ld-BM on tumor-like stroma (12 kPa). With the two groups of hd-BM on 12 kPa matrix and ld-BM on 0.12 kPa matrix, delineating an intermediate state. These four groups are thought to represent tumor progression series.

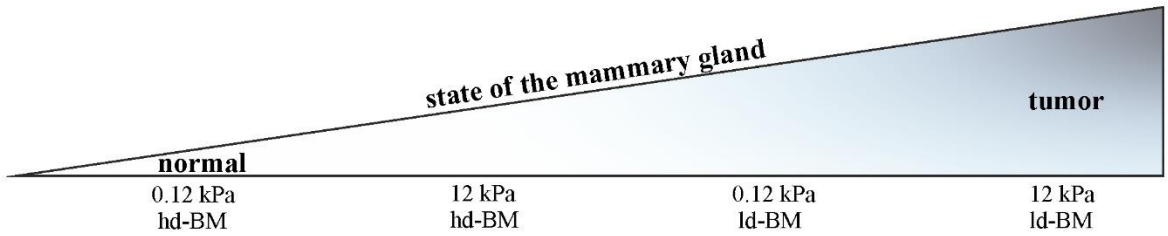

Figure 3.4: Scheme of tumor progression series of the mammary gland from mechanically normal-like to tumor-like phenotype in MCF10A acini model.
MCF10A acini with hd-BM on 0.12 kPa represent normal breast tissue, corresponding to the most physiological conditions *in vivo*. Acini with hd-BM on 12 kPa represent a less physiological state, still with an intact basement membrane but a stiffened extracellular matrix. The state of ld-BM acini on 0.12 kPa represents a kind of competitor of hd-BM acini on 12 kPa, but with a weakened basement membrane, thus prevailing the more pathological state. The most tumor-like condition is represented by ld-BM acini on 12 kPa stiff matrix.

Additionally, the four established groups of mechano-biological tumor progressive scenarios allowed further biochemical treatments of MCF10A acini in order to initiate or suppress their invasive properties.

In the subsequent experiments following biochemical and biomechanical parameters were analyzed on their potential to initiate or retain invasion: ECM stiffness, EGF stimulation and the state of the basement membrane.

3.3.1. Influence of extracellular matrix stiffness on cell invasion

In vivo, mechanical properties of the ECM play a crucial role for the aggressiveness of cancer cells. Thus, cancer invasion is stimulated by increased substrate stiffness [62,121], which in turn has been identified to be associated with breast cancer risk [122].

Using the newly established 3D invasion assay (see Section 3.3), the intention of the following experiments was to determine whether invasion in MCF10A acini can be triggered by matrix stiffening. Simultaneously, the role of the basement membrane as a barrier to invasive cells was observed. To focus exclusively on the influence of the substrate rigidity, no extrinsic EGF stimulus was applied to MCF10A acini. The mean invasion time points were determined for each sample group by evaluation of the phase contrast image sequences. The time point as the first cells escaped from the acinus was defined as invasion onset (see Figure 3.2).

The evaluation of invasion events in analyzed groups revealed that under the most physiological condition (hd-BM, 0.12 kPa), only 2 % of analyzed acini (n = 53) switched to an invasive phenotype and disseminated on the substrate, while 98 % were non-invasive (resting). The invasive phenotype increased 5-fold in the same hd-BM acini (n = 48) group facing a stiffer

(12 kPa) substrate. The invasive phenotype increased even further in ld-BM acini, as the conditions became more tumor-like: In ld-BM groups, 21 % of analyzed acini (n = 82) gained invasive phenotype on the soft substrate, while the number of resting acini decreased to 79 %. And even 29 % of analyzed ld-BM (n = 86) acini invaded the tumor-like (12 kPa) substrate, while 71 % remained resting. An overall comparison of the invasion incidences in analyzed groups comparing the fractions of invasive versus resting acini in percent is graphically shown in Figure 3.5. It could be observed that under tumor progressing scenarios (see also Figure 3.4), the fraction of resting acini decreased, while the fraction of invasive acini increased.

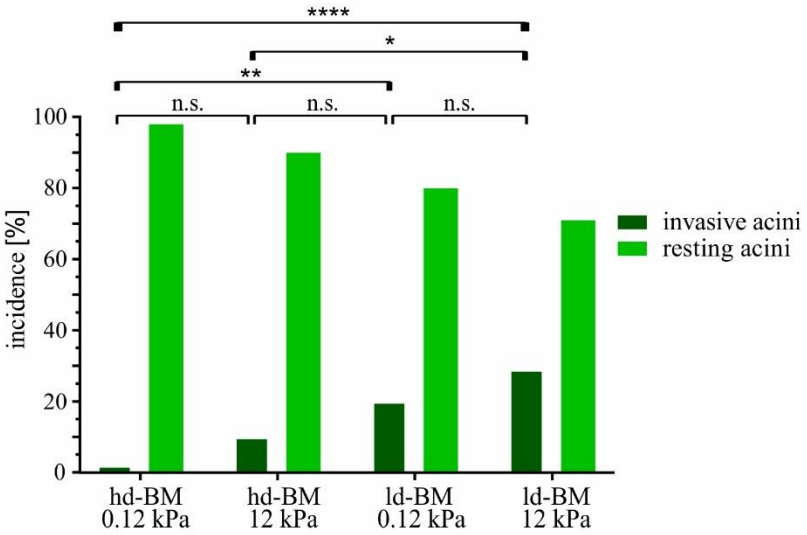

Figure 3.5: Incidences of invasive and resting MCF10A acini under tumor progressing scenarios.
The amount of invasive and resting acini (shown as incidence in percent) was compared under tumor progressing scenarios. In the most physiological state (hd-BM on 0.12 kPa) of MCF10A acini, the amount of resting acini was the highest (98 %), while only 2% of acini in this group became invasive. This distribution changed with progressing tumorous state of acini to ld-BM on 12 kPa, as more acini got the invasive phenotype and less acini stayed as resting acini. Numbers of analyzed acini: hd-BM on 0.12 kPa n = 53, hd-BM on 12 kPa n = 48, ld-BM on 0.12 kPa n = 82, ld-BM on 12 kPa n = 86. Two proportions Z-Test was used to compare the invasive fractions: *: $p < 0.05$, **: $p < 0.01$, ****: $p < 0.0001$, n.s.: not significant.

Further, the course of cumulative invasion onset over time were compared in all four sample groups (see Figure 3.6). A gradual increase of cumulative invasion events was observed in ld-BM acini, while in hd-BM acini the curves remained rather flat, irrespective of the substrate stiffness. The number of total events increased with tumor progressing scenarios. In the most physiological group, hd-BM acini on soft substrates, only one single acinus invaded the substrate, corresponding to 2 %. In contrast, in the most pathological group, ld-BM acini on

rigid substrates, 29% of analyzed acini disseminated on the substrates, indicating a 14.5-fold change of increase in invasive potential. Interestingly, in the intermediate sample groups, the invasion frequency was 2-fold higher in ld-BM acini of soft matrix (21 %), than in hd-BM acini on stiff matrix (10 %).

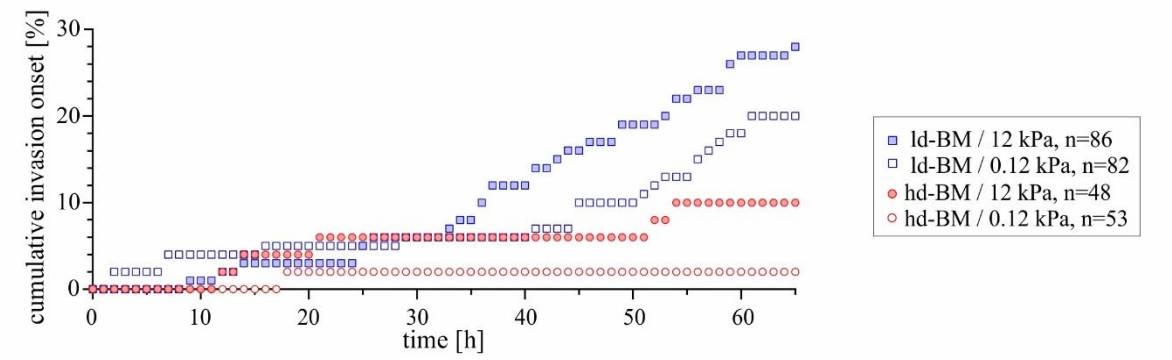

Figure 3.6: Course of cumulative invasion onset in MCF10A acini under tumor progressing scenarios.
Invasion course and outcome are given as cumulative invasion onset over 65 hours. MCF10A acini were analyzed under changing mechanobiological scenarios, without further biochemical stimulation. Under the most physiological condition (hd-BM, 0.12 kPa), the course of cumulative invasion onset was relatively flat compared to the most tumorous conditions (ld-BM, 12 kPa). In hd-BM acini on 0.12 kPa, one acinus invaded the substrate after 18 hours on the substrate, leading to a flat course of the graph. The courses of cumulative invasion onset were similar in both intermediate groups during the first 40 hours on the substrate. But by the end of analyses, the invasion outcomes were different, as in ld-BM acini on 0.12 kPa the fraction of invasive acini was higher than in hd-BM acini of 12 kPa.

From these data, the scatter and the mean time points of invasion onset for all invasive acini from all sample groups were plotted in Figure 3.7. In hd-BM acini only one single acinus invaded the substrate 18 hours after the transfer of acini onto the substrate. In the same BM-group on stiffer substrate (12 kPa), the invasion onsets of the five invasive acini were distributed between 12 and 54 hours after the transfer onto the substrate. As only a few hd-BM acini disseminated on the substrates, no mean time point of invasion onset could be calculated for this BM-group. In ld-BM acini the fraction of invasive acini was high. In these ld-BM groups, the mean invasion onset on 0.12 kPa substrates was calculated to be 40 hours after the transfer, and on 12 kPa, the invasion started 41 hour after the transfer.

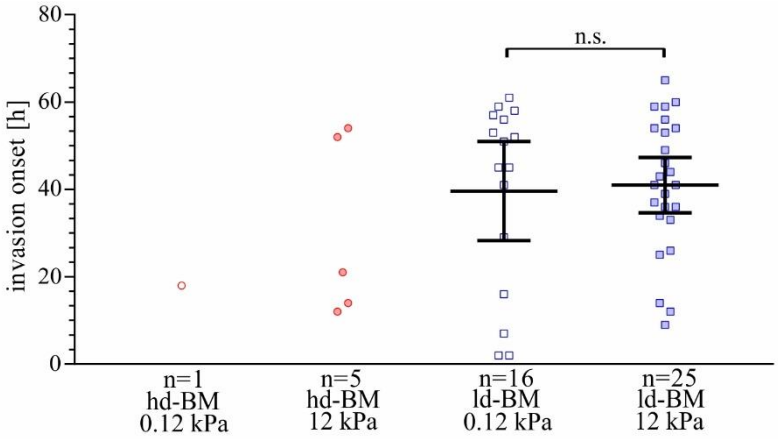

Figure 3.7: Counts of individual invasion onset in MCF10A acini under tumor progressing scenarios.
Scatter plots illustrate the distribution of the individual time points of invasion onsets in hours and the mean values. No significant difference in invasion onsets in ld-BM acini could be observed. In these groups the mean time point of invasion was at 41 hours on 12 kPa and at 40 hour on 0.12 kPa substrates. As the number of invasion onsets in hd-BM acini was low, no mean of invasion onset could be given. Tukey's multiple comparison test: n.s.: $p > 0.05$. Scatter bars: mean with 95 % confidence interval.

The presented analyses on biochemically unstimulated (EGF-depleted) MCF10A acini have demonstrated that on tumor-like (12 kPa) substrates, the invasion incidence in the same basement membrane MCF10A acini groups, was clearly higher than on soft substrates (0.12 kPa). These results indicate that under normal breast gland tissue conditions, a highly developed basement membrane is associated with decreased cell invasion events on tumor-like substrate stiffness (12 kPa).

3.3.2. Influence of EGF on cell invasion in MCF10A acini

In many breast cancers, stiff ECM is accompanied by overexpression of growth factor receptors, which is a marker for a malignant phenotype and poor patient prognosis [49]. A study on MCF10A cells growing as a 2D monolayer has demonstrated that stimulation of those benign cells with high EGF concentration over-rides contact inhibition of these cells and initiates proliferation and invasion [123].

Based on the findings from the previous experiments (see Section 3.3.1), native, EGF-depleted MCF10A acini were analyzed under the established tumor progressing scenarios, from most physiological to highly pathological, as described in 3.3. In the following experiments, breast acini were stimulated with EGF to extrinsically foster cell invasion and decipher the role of the

basement membrane as a possible barrier to invasive cells under EGFR-signaling driven pro-invasive conditions.

The experiments revealed, that under EGF-stimulation the fraction of invasive acini increased in all four analyzed groups (see Figure 3.8). The incidence of invasive acini upon EGF-stimulation was 21-39 % higher in ld-BM acini (see Figure 3.8 A). While in hd-BM groups about half of the analyzed acini disseminated on the substrates (53 % on 0.12 kPa and 59 % on 12 kPa), in ld-BM groups the amount of invasive acini increased to around 80 % (82 % on 0.12 kPa and 80 % on 12 kPa). When directly compared to EGF-depleted acini (see Figure 3.8 B, compare also Figure 3.8 A to Figure 3.5), it could be noticed that the overall invasion incidence in EGF-stimulated acini in mean induced an increase of invasive acini fraction by 53 % in each group. Upon EGF stimulation, the invasive fraction of hd-BM acini on 0.12 kPa ECM increased from 2 %to 53 %, and on 12 kPa from 10 % to 59 %. In ld-BM acini EGF induced an increase of invasive acini from 21 % to 82 % on 0.12 kPa, and from 29 % to 80 % on 12 kPa.

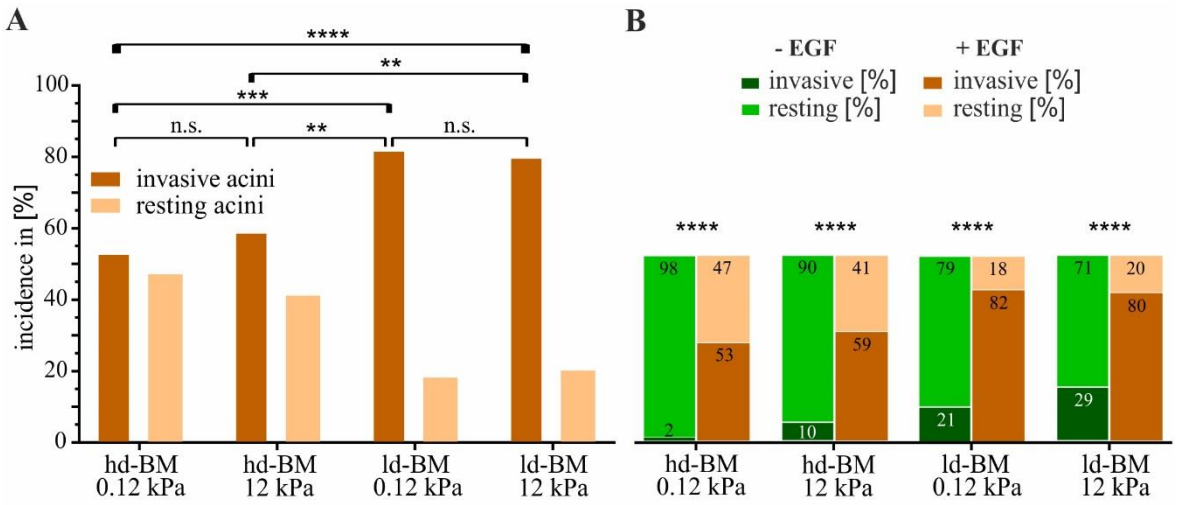

Figure 3.8: Acini invasion incidences in presence and absence of EGF stimulation.
A. The amount of invasive and resting acini (shown as incidence in percent) was compared under tumor progressing scenarios. In hd-BM acini groups, the incidences of resting and invasive acini were similar: about half of the acini in these groups were invasive, independent on substrate stiffness, while the other half was resting. This distribution changed with the basement membrane state. In ld-BM acini on both substrate rigidities, about 80 % of acini invaded the substrates and only 20% were resting. Numbers of analyzed acini: hd-BM on 0.12 kPa n = 113, hd-BM on 12 kPa n = 101, ld-BM on 0.12 kPa n = 67, ld-BM on 12 kPa n = 65. **B.** Combined data analysis from Figure 3.8 A and Figure 3.5. Two proportions Z-Test was used to compare the invasive fractions: **: $p < 0.01$, ***: $p < 0.001$, ****: $p < 0.0001$, n.s.: not significant.

Long term measurements of MCF10A acini stimulated by EGF revealed a different course and outcome of cumulative invasion onsets from those seen in EGF-depleted acini (see Figure 3.9, compare also to Figure 3.6). In general, in EGF-depleted groups, cumulative invasion outcomes seemed to be influenced by substrate rigidity and the state of the basement membrane. In contrast, in EGF-stimulated acini, two outcome groups with similar amounts of cumulative invasion onsets were observed. Here, the incidence of invasive acini seemed to be dependent on the state of the basement membrane and less on substrate rigidity. The general curve progressions showing the cumulative invasion onsets were similar between BM-groups. In ld-BM acini the graphs were steeper than in hd-BM acini, and revealed higher numbers of cumulative invasion onsets (Figure 3.9).

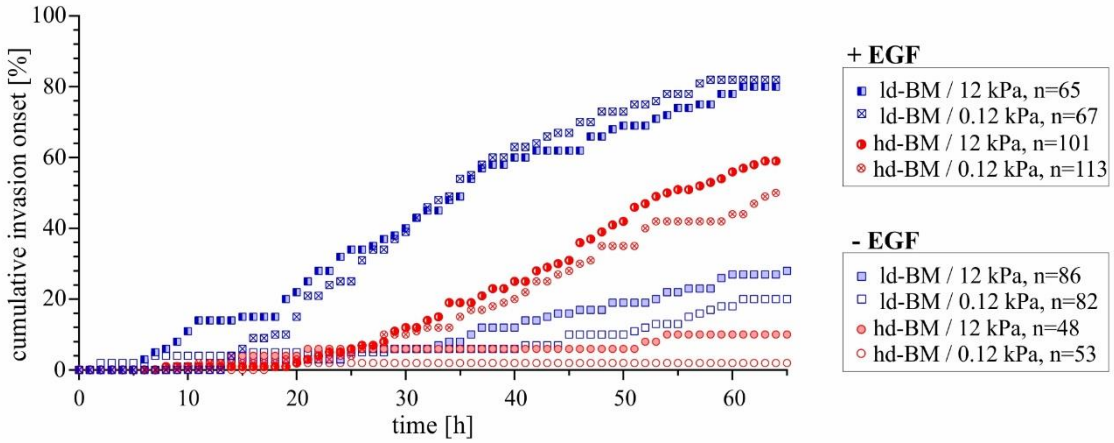

Figure 3.9: Course of cumulative invasion onsets in EGF-stimulated compared to EGF-depleted MCF10A acini under tumor progressing scenarios.
Cumulative invasion onsets over 65 hours. In EGF-stimulated groups, the curve progressions of cumulative invasion events in ld-BM acini were similar and clearly above the curves of hd-BM acini, which also showed a similar progression compared among themselves, independent on substrate rigidity. In total, 21 % more ld-BM acini disseminated on stiff substrates and 29 % more ld-BM acini disseminated on soft substrates, compared to corresponding hd-BM acini groups. In contrast, in EGF-depleted groups the invasiveness steadily increased with increasing tumor conditions.

Additionally, the individual time points of invasion onsets were compared. Here, the highly-developed state of the basement membrane showed a significant impact on the average invasion time points in individual acini (see Table 3.1 and Figure 3.10). The mean invasion onset in hd- BM acini (32.2 hours) interacting with a normal-like matrix stiffness (0.12 kPa) was 11.7 hours later when directly compared with ld-BM acini (43.9 hours) on the same substrate stiffness of 0.12 kPa. The difference of the average invasion onset between hd-BM (30.9 hours) and ld-BM (42.3 hours) acini on stiff substrate (12 kPa) was 11.4 hours. Statistical evaluation

confirmed a positive coherence between impaired basement membrane development, significantly higher incidence and accelerated time course of cell invasion (see Figure 3.10).

Table 3.1: Statistics of invasion onsets in EGF-stimulated MCF10A acini.

	hd-BM		ld-BM	
	0.12 kPa	**12 kPa**	**0.12 kPa**	**12 kPa**
mean invasion onset [h]	**43.9**	**42.3**	**32.2**	**30.9**
Lower 95 % CI*) of mean [h]	40.3	39.1	28.9	26.5
Upper 95 % CI of mean [h]	47.6	45.5	35.5	35.2
number of invasive acini	60	60	55	52

*) CI: confidence interval.

For EGF-stimulated ld-BM acini on both substrate elasticities, a trend of decreased invasion onset could be observed, to approximately 30 hours, compared to EGF-depleted hd-BM acini in which the mean invasion onset started about 40 hours after acini transfer (see Figure 3.10). At the same time, the mean invasion onset in EGF-stimulated hd-BM acini was close to the EGF depleted ld-BM acini groups, taking place after about 40 hours on the substrates.

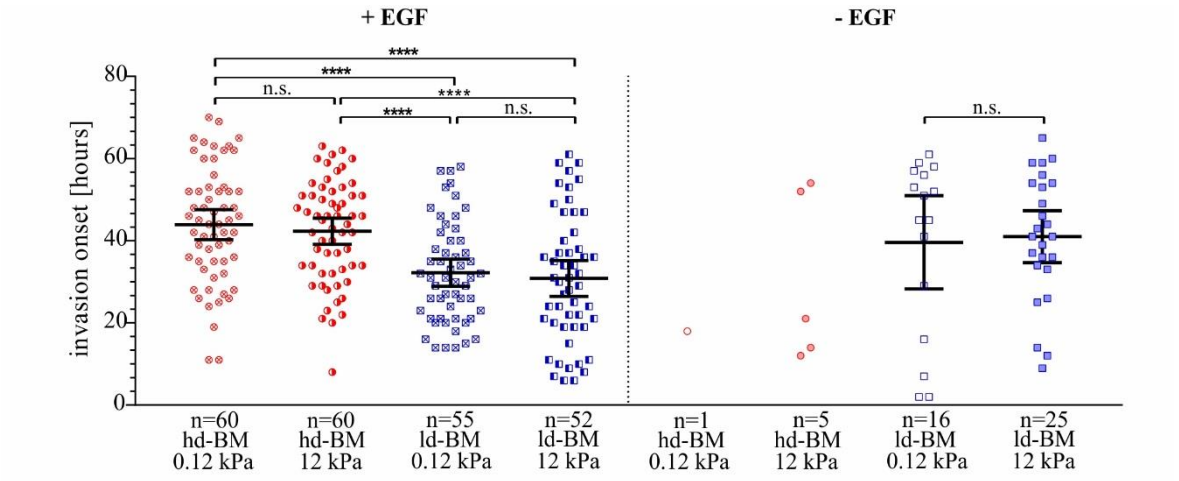

Figure 3.10: Counts of individual invasion onsets in EGF-stimulated and EGF-depleted MCF10A acini under tumor progressing scenarios.
Scatter plots illustrate the distribution of the individual time points of invasion onsets in hours and the mean values. In EGF-stimulated groups, ld-BM acini invaded the substrates (0.12 kPa and 12 kPa) significantly earlier than hd-BM acini, on the same substrate elasticities. Hd-BM acini invasion took place about 11 hours later. Without EGF, no significant difference in invasion onsets in ld-BM acini could be observed. In these groups the mean time point of invasion was at 40 hours on 12 kPa and at 41 hour on 0.12 kPa, being close to the mean invasion onsets in EGF-stimulated hd-BM acini. In EGF-depleted hd-BM acini the invasive fraction was too low for a statistical test. Tukey's multiple comparison test: *** $p < 0.001$, **** $p < 0.0001$, n.s.: $p > 0.05$. Scatter bars: mean with 95 % confidence interval.

Overall, these results demonstrate that aberrant stimulation of MCF10A acini with EGF, resulted in an increase of invasive phenotype in all four groups, irrespective of the BM state or substrate stiffness.

The critical role of the basement membrane as a possible barrier to invasive cells became more evident, since acini covered by a highly-developed basement membrane showed less susceptibility to invasion on both matrix rigidities, when directly compared to corresponding groups with low-developed basement membrane. Additionally, hd-BM acini invaded the substrates significantly later than ld-BM acini. These results emphasize that the state of the basement membrane might be a very important factor in keeping acini from invasion.

3.3.3. Analyses of invasion-arresting role of the basement membrane by biochemical treatments

Previous experiments on EGF-depleted and EGF-stimulated MCF10A acini demonstrated that healthy basement membrane (hd-BM) seems to retard the acini from invasion. To evaluate the actual role of the basement membrane as a barrier to invading cells, two following experiments were performed to affect the state of the basement membrane. Biochemical drugs were used either to interfere the structural integrity of the basement membrane or to stabilize the basement membrane.

Influence of type IV collagenase treatment on invasive potential of MCF10A acini

Type IV collagen is a key player and the major component of the basement membrane. The mesh-like structural composition of this protein has been identified to strengthen the basement membrane and to provide structural support [124]. These properties made type IV collagen (coll IV) a suitable target candidate to weaken the structural integrity of the basement membrane. It was hypothesized that proteolytic degradation of the basement membrane by type IV collagenase might induce faster invasion and additionally lead to increased invasion outcome in MCF10A acini.

To test this hypothesis the most physiological condition with hd-BM acini on 0.12 kPa was chosen, as in previous experiments (see Sections 3.3.1 and 3.3.2) acini under this condition showed the lowest invasion incidences. Here, the basement membrane of hd-BM acini was weakened by type IV collagenase digestion. To prove that the basement membrane was affected by type IV collagenase, immunofluorescent stainings were performed. For that type IV collagen

(coll IV) and laminin-332 (lam-332) were stained after treatment (see Figure 3.11). When compared to untreated MCF10A acini, in which the basement membrane showed a continuous signal (see Figure 3.1 B), in type IV collagenase treated acini nearly no coll IV was present, despite of some fragments sparsely located around the acinus. In addition, lam-332 staining showed a less continuous signal in the treated acini. Areas with weak or absent lam-332 signal were visible, presumably at the sites where no correlation to coll IV was evident.

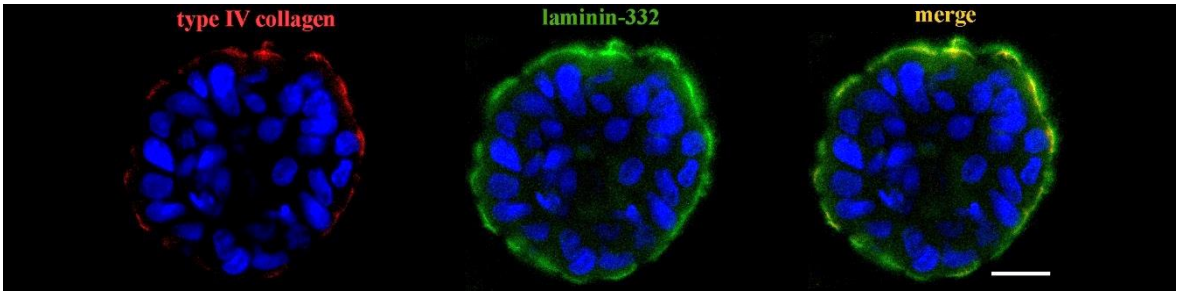

Figure 3.11: Type IV collagenase treatment of MCF10A acinus to disrupt the structural basement membrane integrity.
Micrographs demonstrate an hd-BM MCF10A acinus treated with type IV collagenase (290 U/mL, 3 h) and immunofluorescently stained for the basement membrane proteins type IV collagen (red) and laminin-332 (green). Nuclei were counterstained with DAPI. There was low type IV collagen signal, while the signal of laminin-332 was present around the acinus. At sites of correlation with digested type IV collagen, the laminin-332 signal appeared weaker. Both signals were merged to show co-localization (yellow). Scale bar = 20 µm.

Type IV collagenase treatment successfully impaired the coll IV meshwork of hd-BM acini. The establishment of this assay was important for the next step, comparing the invasion outcome of untreated and treated acini.

In Figure 3.12 A the cumulative invasion onsets in EGF-stimulated, collagenase treated hd-BM acini group were compared to the corresponding group of native EGF-stimulated hd-BM acini. The comparison of these two groups revealed that the state of the basement membrane has an impact on the invasion outcome: the intact basement membrane seemed to impede the cell invasion process. Thus, in native, most physiological acini group only half (53 %) of all analyzed acini (n = 113) showed invasive behavior, compared to 100 % of invasive acini (n = 51) with a structurally impaired basement membrane (see Figure 3.12 A). Two proportions Z-Test was used to compare the invasive fractions of those groups and showed a highly significant difference ($p < 0.0001$).

Additionally, the mean invasion onset in collagenase treated group was significantly earlier. While untreated acini needed on average 44 hours to initiate invasion, as soon as the basement membrane was purposely weakened by type IV collagenase, the mean invasion time point dropped to 28 hours (see Figure 3.12 B). The mean invasion onset was significantly delayed (by 16 hours) in acini with impaired BM integrity compared to the untreated control group.

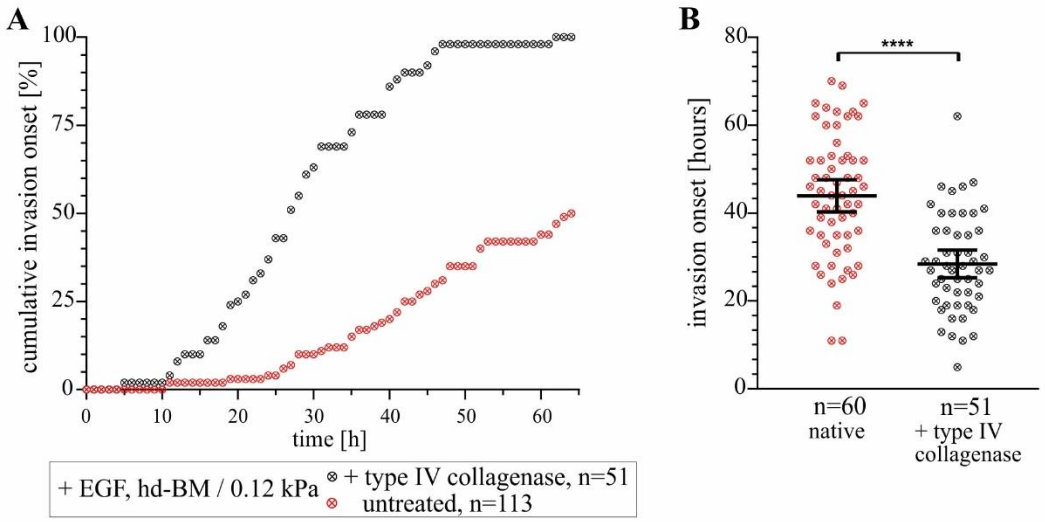

Figure 3.12: The impact of basement membrane destabilization on cell invasion in MCF10A acini. Cell invasion of hd-BM MCF10A acini on 0.12 kPa substrates after treatment with type IV collagenase, compared to the corresponding untreated group. Both groups were stimulated with 20 ng/mL EGF. **A.** Cumulative invasion onsets during the analysis period of 65 hours. In acini with native basement membrane, 53 % of all analyzed acini were invasive, while after collagenase IV treatment of the basement membrane, all acini disseminated on the substrate. **B.** Scatter dot plot illustrates the time points of invasion onset in the invasive acini fraction. The mean invasion onset was clearly delayer (by 16 hours) in acini with impaired basement membrane integrity compared to the untreated control group. Tukey's multiple comparison test: **** $p<0.0001$. Scatter bars: mean with 95 % confidence interval.

These results demonstrate that a structurally intact basement membrane has a high impact on preventing cell invasion in breast acini. In type IV collagenase treated acini the invasion onsets started in mean 16 hour earlier compared to the untreated group.

Influence of matrix metalloproteinases on invasion in MCF10A acini

Treatment of MCF10A acini with type IV collagenase resulted in weakening of the basement membrane. This raised the question whether in untreated MCF10A acini the observed invasion events were also triggered by enzymatic degradation of the basement membrane. In this context, matrix metalloproteinases (MMPs) are the most important proteolytic enzymes capable to degrade nearly all proteins found in the ECM and were described to be highly expressed in breast cancer tissue [125].

To test, whether or to what extent MMP activity could contribute to the basement membrane degradation and therefore to the BM-cell invasion process in MCF10A acini, following experiments were performed. MCF10A acini groups under the four established tumor progressing scenarios in which invasion was stimulated by EGF were chosen (see Section 3.3.2). In these acini, the BM state was experimentally stabilized by inhibition of proteolytic MMP activity by applying the broad spectrum MMP-inhibitor marimastat.

Data analysis revealed that the invasion incidence in all four groups was reduced by MMP-inhibition, but was not disabled entirely. In Fig. 3.13 the data from marimastat treated MCF10A acini are compared to the corresponding groups of native MCF10A acini previously shown in Figure 3.9. In the presence of marimastat, even in hd-BM sample group, cells were still capable to escape from the acinus and emigrate into the microenvironment. Nevertheless, the presence of marimastat inhibitor significantly (two proportions Z-Test) reduced the spreading incidence in all four acini groups - on average by approximately 30 % each, compared to the control groups: from 80 % to 44 % (-36 %, $p < 0.0001$) in ld-BM acini on 12 kPa (see Figure 3.13 A), from 82 % to 52 % (-30 %, $p < 0.001$) in ld-BM acini on 0.12 kPa (see Figure 3.13 B), from 59 % to 33 % (-26 %, $p < 0.001$) in hd-BM acini on 12 kPa, (see Figure 3.13 C), and from 53 % to 23 % (-30 %, $p < 0.0001$) in hd-BM acini on 0.12 kPa (see Figure 3.13 D).

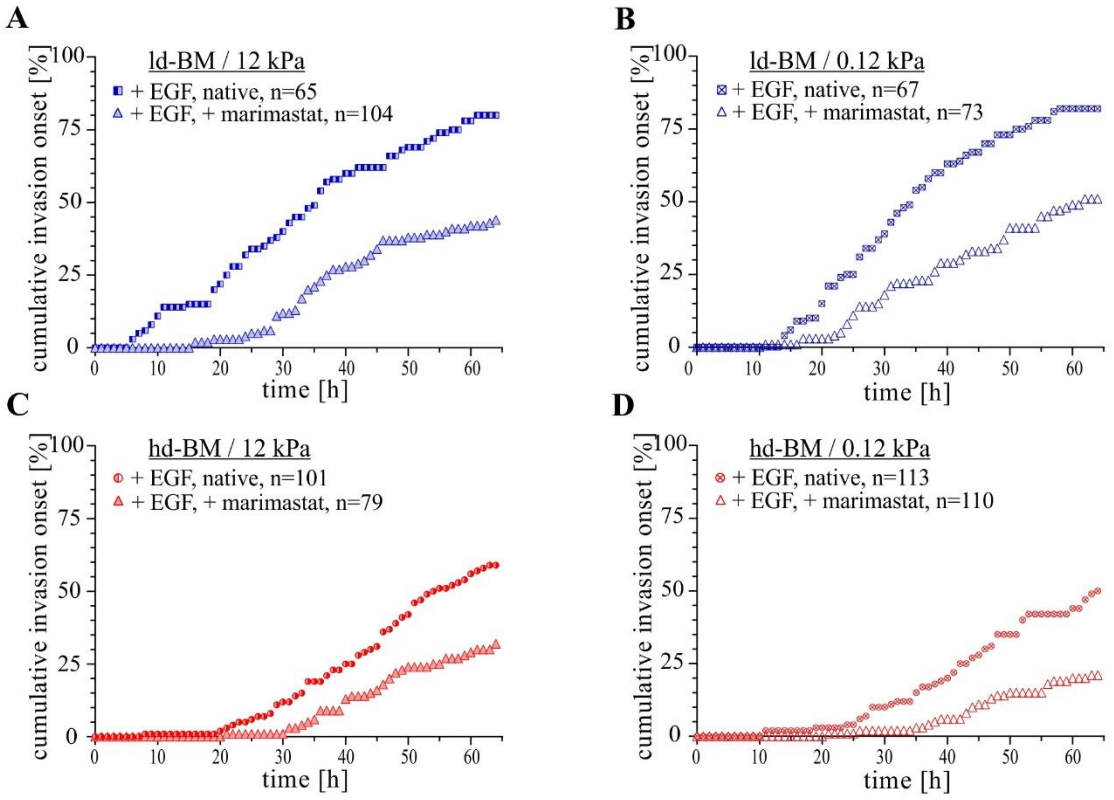

Figure 3.13: Course of cumulative invasion onsets in MCF10A acini upon stabilization of the basement membrane by MMP-inhibition.
A-D. Cumulative invasion onsets over time (65 hours) in designated marimastat treated (20 µM) acini groups, directly compared to the corresponding native groups. Both groups were stimulated by 20 ng/mL EGF. The number of invading acini in marimastat treated acini dropped in mean by about 30 % in all analyzed groups. This led to more plane courses of cumulative invasion onsets, compared to the untreated groups. Ld-BM acini groups are shown in blue, hd-BM acini in red.

In marimastat treated hd-BM acini the mean invasion inset was retarded by 7-8 hours compared to the corresponding ld-BM acini groups which disseminated on the substrates in mean 38 hours after the transfer (see Table 3.2).

Table 3.2: Statistics of invasion onset in MMP-inhibited acini.

	hd-BM		**ld-BM**	
	0.12 kPa	**12 kPa**	**0.12 kPa**	**12 kPa**
mean invasion onset [h]	**46.9**	**45.7**	**37.9**	**38.1**
Lower 95 % CI*) of mean [h]	42.3	41.0	33.4	34.7
Upper 95 % CI of mean [h]	51.5	50.3	42.4	41.5
number of invasive acini	25	26	38	46

*) CI: confidence interval.

The mean time of invasion onset in marimastat treated and untreated MCF10A acini groups were similar (see Figure 3.14, compare also to Figure 3.10). In hd-BM acini on both substrate elasticities, the mean invasion onset started about 40 hours after acini transfer in untreated acini, and 46 hours in marimastat treated acini. In marimastat treated and untreated ld-BM acini, on both substrate elasticities, a trend of decreased invasion onset could be observed, to approximately 30 hours in untreated, and to 33 hours in marimastat treated.

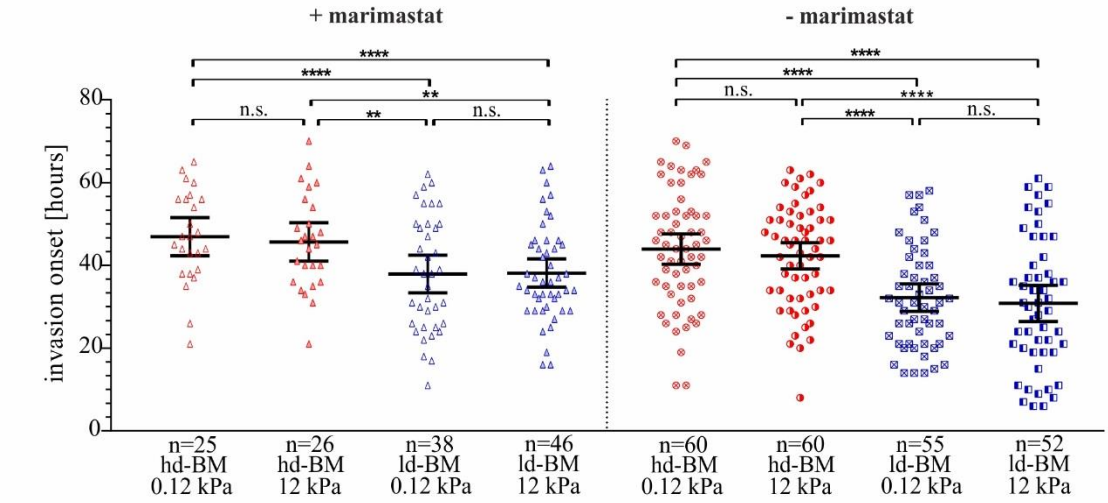

Figure 3.14: Counts of individual invasion onsets in marimastat treated and untreated MCF10A acini under tumor progressing scenarios.
Individual time points of invasion onsets in hours. In marimastat treated (20 µM) and untreated groups the trend of invasion initiation was similar among corresponding groups. Ld-BM acini disseminated on the substrates significantly earlier than hd-BM acini, independent of substrate elasticities. In marimastat treated group, hd-BM acini took about 8 hours longer to initiate invasion, while in untreated groups hd-BM acini took about 11 hours longer for invasion onset, compared to ld-BM acini. Tukey's multiple comparison test: ** $p<0.01$, *** $p<0.001$, **** $p<0.0001$, n.s. Scatter bars: mean with 95 % confidence interval.

These experiments showed that marimastat induced a major decrease of cumulative invasion onsets in all four analyzed MCF10A acini groups. Though, the invasion incidence was not completely disabled by the broad-spectrum MMP-inhibitor. This indicates that the presence of the invasive acini fraction in marimastat treated groups is triggered either by residual MMP activity or by further factors, other than MMPs. Since the invasion in those groups was triggered by EGF, this raised the question whether the invasion onsets could be completely disabled by marimastat in EGF-depleted acini.

To figure this out, the group that exhibited the highest invasion outcome in EGF-depleted MCF10A acini, ld-BM acini on 12 kPa, was chosen (see section 3.3.1). As previously shown, in this group 29 % of acini (n = 86) invaded the substrate (see Figure 3.15 A, blue curve), even without EGF stimulation. Inhibition of MMPs in these EGF-depleted ld-BM acini on 12 kPa led to a significant drop of invasion events. Here, only 5 % of all analyzed acini (n = 88) showed cell BM transmigration and dissemination onto the substrate (see Figure 3.15 A). Two proportions Z-Test was used to compare the invasive fractions of those groups and showed a highly significant decrease of invasion incidence ($p < 0.0001$).

In marimastat treated ld-BM acini on 12 kPa the invasion events were visibly decreased by marimastat to only four invasive acini, out of 88 analyzed acini. The invasion onsets in those four acini was scattered between 3 and 61 hours. Due to the low count, no statistical mean invasion onset could be calculated. In contrast, in the corresponding untreated group, acini invaded the substrate in mean 41 hours after the transfer (see Figure 3.15 B).

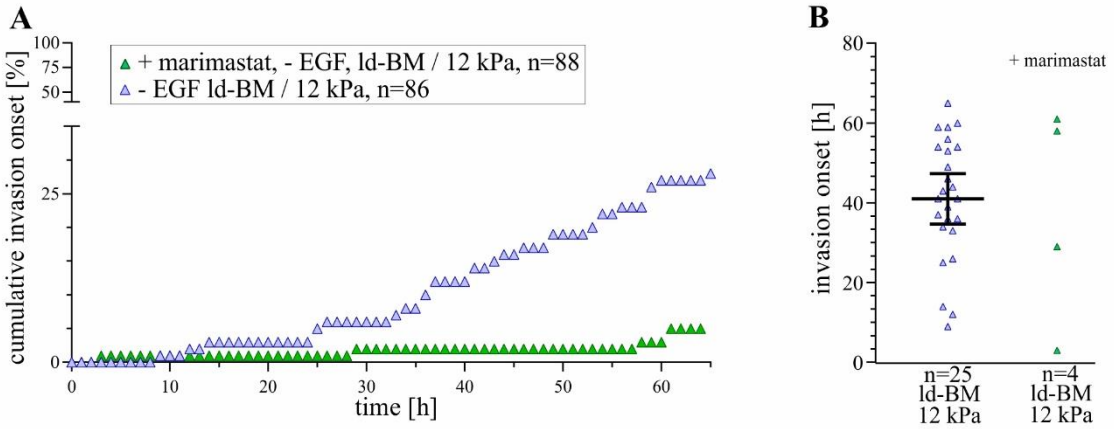

Figure 3.15: Cell invasion after MMP inhibition in EGF-depleted MCF10A acini.
EGF-depleted ld-BM acini on 12 kPa substrates treated with marimastat (20 µM) were analyzed and compared to the corresponding untreated group. **A.** Cumulative invasion onsets over 65 hours. In total only 5 % of marimastat treated acini invaded the substrate by the end of investigation time, making up a decrease of invasion onsets by 24 % compared to the untreated group. **B.** Time points of invasion onsets in individual acini. While EGF-depleted acini needed in mean 41 hours to initiate invasion, the amount of invasive marimastat treated acini was as low, that no statistical mean value could be given. Here only four acini invaded the substrate. Scatter bars: mean with 95 % confidence interval.

This experiment has shown that the invasion onset in MCF10A acini can be nearly entirely suppressed by marimastat, when the invasive phenotype is not triggered by EGF. This result together with the result on type IV collagenase treatment, suggest that during the invasion

process of MCF10A acini, proteolytic degradation of the basement membrane by MMPs might play an important role, triggering earlier invasion onset as well as higher invasion incidence.

3.4. Investigation of the role of the phosphoinositide 3-OH kinase (PI3K) as a possible invasion initiator in MCF10A acini

It has been shown that invasive breast cancer cells use invadopodia, specialized ECM-degrading cellular protrusions, to breach the basement membrane [126]. Other studies could convincingly demonstrate that invadopodia formation can be induced by growth factor stimulation [106]. Additionally, other investigations focused on the signaling pathways that link the extracellular stimulation to invadopodia formation. In this context, phosphoinositide 3-OH kinase (PI3K), an essential player in migration and invasion [107], was shown to be required for invadopodia formation in human breast cancer cells [106].
Therefore the intention of the next experiment was to analyze whether PI3K is involved in induction of the invasive phenotype in MCF10A acini. The involvement of PI3K activity was proven by its inhibition by wortmannin.

Temporal inhibition of PI3K in the most tumorigenic group, ld-BM acini on tumor-like stiff ECM (12 kPa), stimulated by EGF, led to a clear shift in cumulative invasion onsets (see Figure 3.16 A). The wortmannin treated group was compared to untreated ld-BM acini on 12 kPa and to hd-BM acini on 0.12 kPa. Interestingly, at the beginning of the measurement, up to 25 hours on the substrates, the cumulative events in wortmannin treated tumorigenic group were nearly identical to the more physiological group (hd-BM on 0.12 kPa), while in untreated ld-BM acini on 12 kPa, more cumulative invasion events took place during the same time period. By the end of the measurements, the invasion incidence in wortmannin treated group (70 %) laid in-between the two other groups, ld-BM on 12 kPa (80 % cumulative invasion onsets, two proportions Z-Test: $p > 0.05$), and hd-BM on 0.12kPa (53 % cumulative invasion onsets, two proportions Z-Test: $p < 0.05$).
Moreover, treatment of the tumorigenic group with wortmannin, led to an increase of the mean invasion onset, compared to the untreated group (see Figure 3.16 B). In the untreated ld-BM acini the mean invasion onset was approximately 31 hour after the transfer. In contrast, wortmannin treatment resulted in a delayed mean invasion onset by 13 hours. In this group

(ld-BM on 12 kPa), the mean invasion onset was 44 hours after the acini transfer, which was identical to the untreated hd-BM acini on 0.12 kPa.

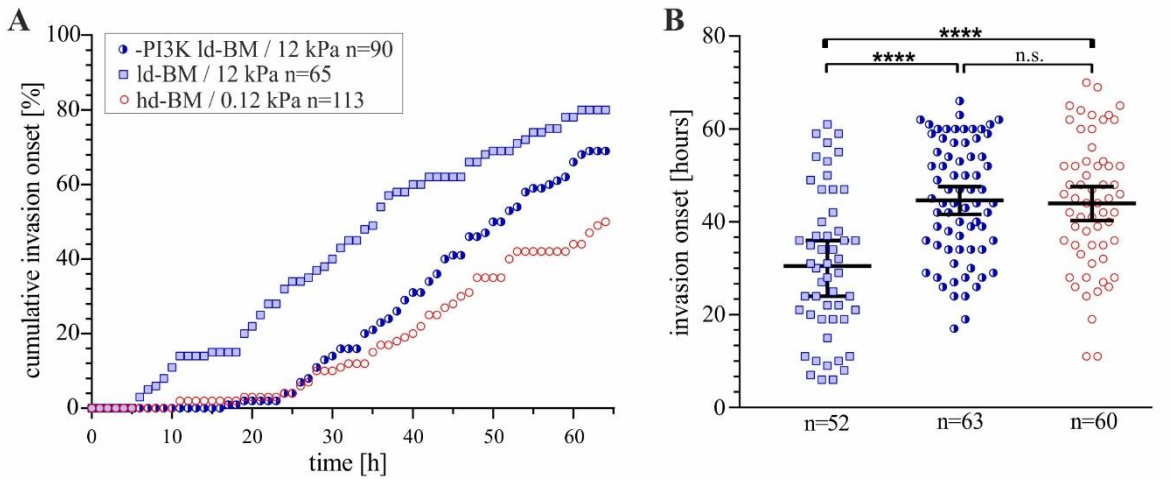

Figure 3.16: Inhibition of cell invasion in MCF10A acini by PI3K inhibitor.
Ld-BM acini on 12 kPa substrates were treated with wortmannin (1 h, 25 nM). The cumulative course of invasion and outcome, as well as the mean invasion onset were compared to corresponding untreated group (ld-BM acini on 12kPa), and to the more physiological group, hd-BM acini on 0.12 kPa. All groups were stimulated by 20 ng/mL EGF. **A.** Cumulative invasion onsets over 65 hours. Wortmannin induced a shift of the cumulative invasion onsets when compared to the control group, towards the outcome seen in the more physiological group. In wortmannin treated acini the invasion was reduced by 10 % compared to the untreated control group. **B.** Time points of invasion onsets in individual invasive acini. Wortmannin treated acini in mean started substrate invasion 44 hours after the transfer, similar to the physiological group, hd-BM acini on 0.12 kPa. Thus wortmannin treated acini disseminated13 hours later than the control group, ld-BM acini on 12 kPa. Tukey's multiple comparison test: ****: $p<0.0001$, n.s.: $p > 0.05$. Scatter bars: mean with 95 % confidence interval.

Overall, the analyses of the invasive potential of MCF10A acini under different conditions showed that the state of the basement membrane has a high impact on invasion outcome. In the first experiment it could be demonstrated that the stiffness of the substrate promoted increased invasion while the highly developed basement membrane seemed to retard the cells from invasion. Once the invasive phenotype of MCF10A acini was additionally stimulated with aberrant concentration of EGF, the influence of substrate rigidity was neglectable, while the role of the basement membrane as a barrier became more apparent. Proteolytic weakening of the basement membrane by type IV collagenase led to 100 % of invasion onsets of the analyzed acini, while inhibition of proteolytic enzymes led to a large decrease of invasive potential of MCF10A acini. Additionally, temporal inhibition of the PI3K signaling pathway resulted in a shift of the invasive phenotype towards more physiological group, with less and later invasion

insets. These results lead to the hypothesis that during the invasion process of MCF10A acini the state of the basement membrane is largely controlled by MMPs and the invasive phenotype might be induced via the PI3K mechanotransduction pathway, by initiating migration and invadopodia formation.

3.5. Investigation of the strain energy generated by MCF10A acini during invasion

Cells in a tissue constantly exert tractions on their environment during a variety of cellular functions including physiological processes like wound healing, but also during aberrant behavior, like spreading and invasion processes seen in cancer [114,127]. Thus, cell fate, tissue development and its proper functions are force-modulated. This is also true for the human breast, and loss of tissue force homeostasis can lead to breast cancer progression [51,57]. Malignant changes of environmental forces, such as ECM stiffening in cancers, can reinforce focal adhesions and activate increased actomyosin contractions [128]. This led to the question, whether cellular forces are also changed in the induced invasive MCF10A acini phenotype.
Therefore the intention of the next experiments was to identify a possible interplay between matrix stiffness, aberrant growth signaling and potential increase of cellular contractility in MCF10A acini. Hereby, TFM was used to determine the stress that is applied by MCF10A acini to the substrate during the rolling phase and invasion.

Following investigation on invasive potential of MCF10A acini, the developed invasion assay was used to determine the strain energy applied by MCF10A acini to the substrates of different rigidities. The 3D invasion assay was compatible with TFM, by introduction of fluorescent microbeads on top of the elastomeric substrates. This enabled determination of the stress applied by acini to the substrates by tracking the bead displacements. The determined stress was further converted into strain energy, which is defined as the total energy transferred by the cells to the substrate.

3.5.1. Characterization of the system substrate properties

Prior to investigation of the strain energy applied by MCF10A acini, the empty, cell-free positions which were simultaneously recorded in each experimental run, were carefully analyzed. So far no long time TFM experiments over 60 hours were performed on crosslinked PDMS substrates in our laboratory. Therefore it was important to characterize the properties of the system over the observation time. For this, conditions and image processing were held identical for the cell-free positions, as for other acini-containing positions. The different substrate rigidities were analyzed separately. Interestingly, a ground level of substrate deformations could be measured at all cell-free positions. Representative images of bead displacement fields and corresponding forces are shown in Figure 3.17.

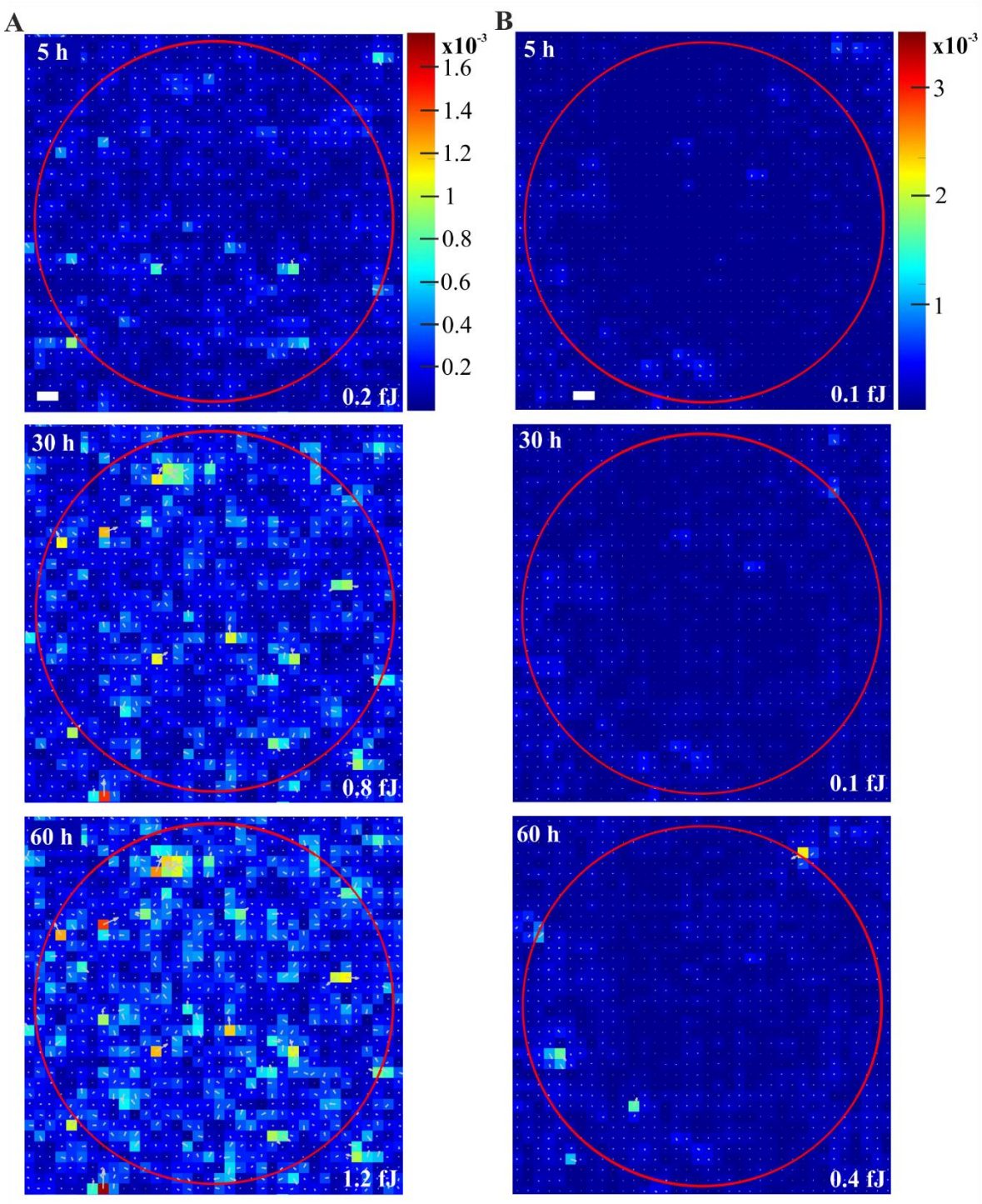

Figure 3.17: Representative heat maps of strain energy at cell free control position.
A. Cell free position on 12 kPa stiff substrate. Linear interpolated stress maps of substrate deformations with incorporated force vectors. Force vector scale: 0.2 nN. For a better visualization a rough grid was chosen. **B.** Cell free position on 0.12 kPa elastomeric substrate. Linear interpolated stress maps of substrate deformations with incorporated force vectors. For a better visualization a rough grid was chosen. Force vector scale: 0.04 nN. All heat maps show stress in nN/µm^2.

The determined strain energy values at cell free positions on 12 kPa and 0.12 kPa substrates are graphically shown as scatter dot plots in Figure 3.18. At the beginning of the measurements (5 hours after the acini transfer), the median strain energy values on the soft substrates (0.12 kPa) were visibly below the strain energy values on the rigid substrates (12 kPa). On 0.12 kPa substrates the median strain energy value started at approximately 0.001 fJ and increased to 0.3 fJ over the investigation time of 60 hours. On 12 kPa substrates, the initial median strain energy value was approximately 0.04 fJ and increased to 2 fJ over the observation time. Independent of substrate stiffness, intensive increase of strain energies could be observed between 5 and 30 hours. From this time point on, only marginal increase of strain energy could be observed, resulting in a kind of a plateau.

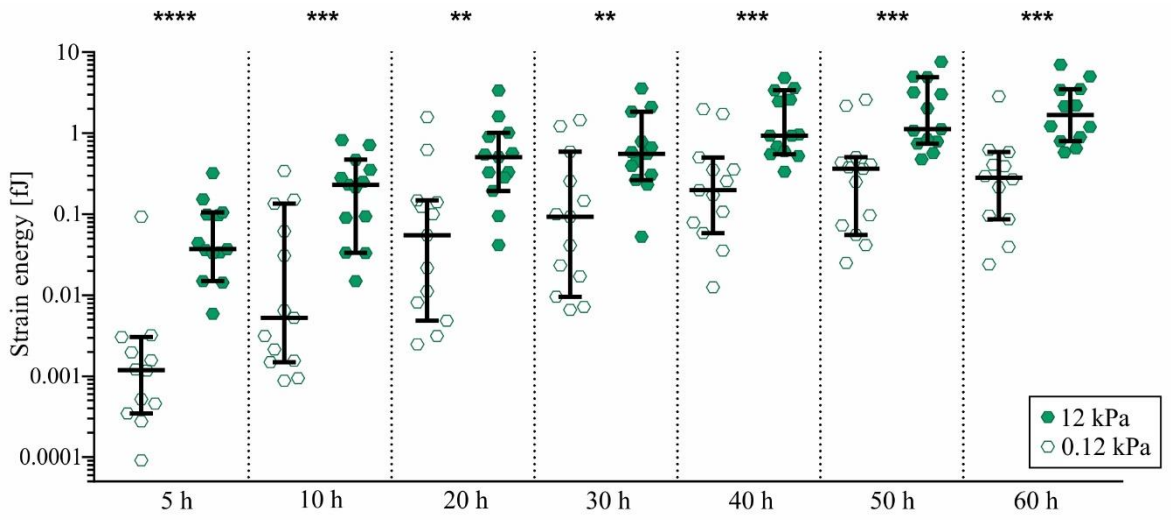

Figure 3.18: Strain energy at cell-free positions.
The median strain energy values in fJ at cell-free positions were analyzed on two different substrate rigidities, 0.12 kPa (n = 13) and 12 kPa (n =13) over the investigation time. The values were plotted logarithmically (log_{10}). On both substrates the strain energy values increased over the time. On 0.12 kPa substrates, the median strain energy values at all time points were lower than on 12 kPa substrates. Mann-Whitney-Test: ****: $p < 0.0001$, ***: $p < 0.001$, **: $p < 0.01$. Scatter bars: median with 95 % confidence interval.

The analysis of cell-free control positions revealed the presence of a baseline strain energy level. These values gradually increased over the observation time. Most of the determined baseline strain energy values were below 1 fJ. The baseline strain energy exceeded 1 fJ only by the end of the measurements (60 hours) on 12 kPa elastomeric substrates reaching a final value of 2 fJ. In following analyses, when looking at the strain energies applied by MCF10A acini to

the substrates, the corresponding strain energies at cell free control positions were also plotted into the graphs.

3.5.2. Strain energy applied by MCF10A acini during invasion

Previous results on invasion outcome in MCF10A acini under tumor progressing scenarios, stimulated with EGF, revealed a high outcome of invasive acini (see Section 3.3.2). To determine the strain energy that MCF10A acini generate during invasion, the mentioned groups with the highest invasive potential were chosen for investigation by TFM: ld-BM and hd-BM acini on 0.12 kPa and 12 kPa substrates, all stimulated with EGF, to trigger the invasive phenotype.

As already described in section 3.2, invasion onset was assessed in phase contrast images by first appearance of a cell escaping from the acinus. As the invasion onset varied between single acini, this individual time point was set as the mutual point of origin (0 h). Strain energies were compared at the time of invasion onset and at four further time points emanating from this time point: 5 and 10 hours prior to invasion onset and 5 and 10 hours post invasion onset.
Directly after the transfer onto elastomeric substrates, MCF10A acini began to rotate in place, thereby applying measurable stress to the substrate. A general observation in the analyzed MCF10A acini groups was the readily increasing strain energy over the entire investigation time, during the rolling phase, 5 and 10 hours prior to invasion onset and after the invasion onset. In Figure 3.19 a representative image sequence of an invading MCF10A acinus is shown as phase contrast images (upper row) with the corresponding linear interpolated stress maps with incorporated force vectors (lower row). The calculated strain energies (from the stress maps) are shown for the designated time points. In this representative image sequence, the ld-BM acinus generated a maximum strain energy of 120 fJ to the substrate (12 kPa) during the rolling phase, 10 hours prior to invasion onset (-10 h). The strain energy remained quite constant during the following 5 hours on the substrate (-5 h, 115 fJ). At the invasion onset (0 h), invasive cells applied 230 fJ to the substrate, a 2-fold increase in applied strain energy from the recorded strain energy 10 hours prior to invasion onset. Following invasion onset, acinar cells collectively invaded the substrate. Thereby the strain energy further increased to 320 fJ, 5 hours after the invasion onset (+5 h), and to 6000 fJ, 10 hours after the invasion onset (+10 h).

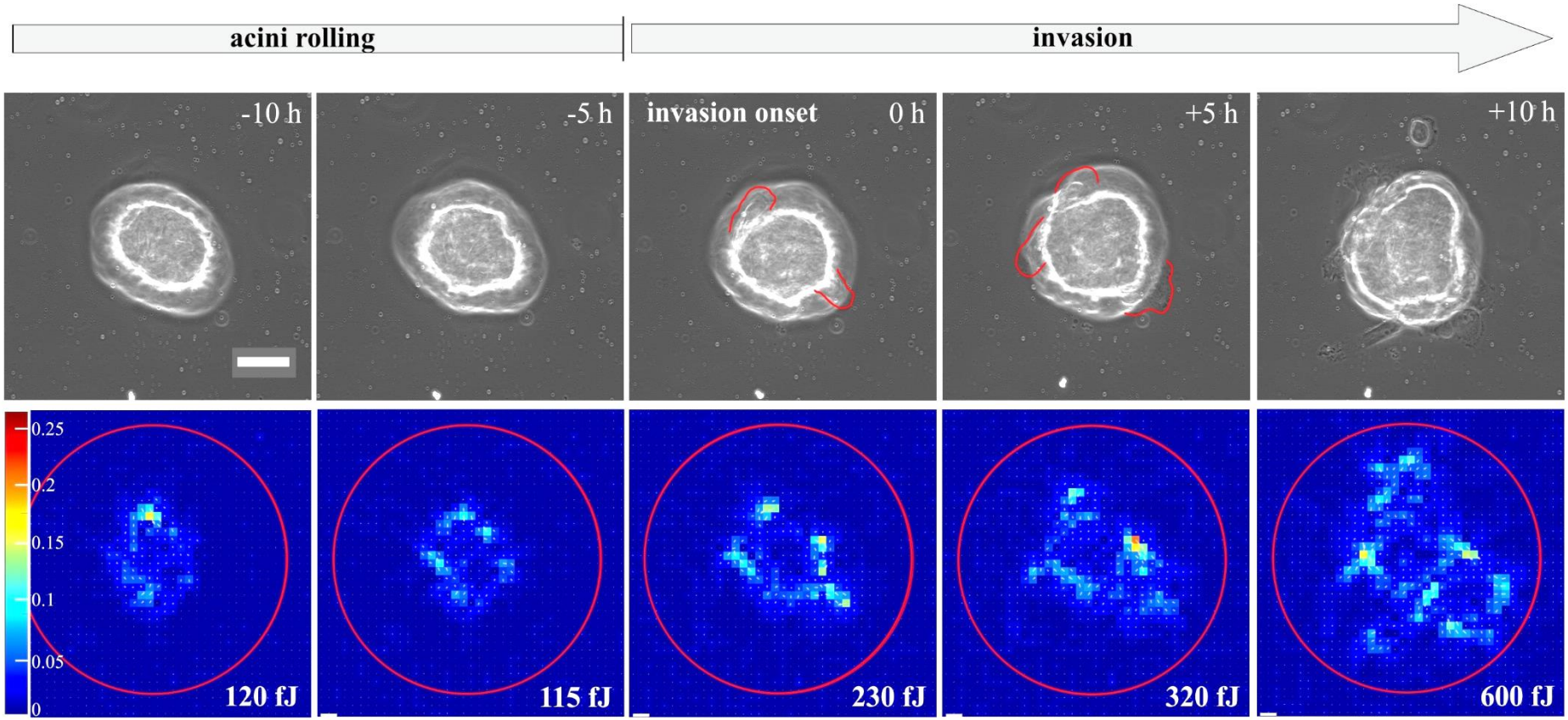

Figure 3.19: Strain energy applied to the substrate by invasive MCF10A acinus.
EGF-stimulated (20 ng/mL) ld-BM MCF10A acinus on 12 kPa elastomeric substrate. Upper row: phase contrast images. Lower row: Corresponding linear interpolated stress maps of substrate deformations with incorporated force vectors. Force vector scale: 6 nN. The heat maps show tangential stress in $nN/\mu m^2$, which were converted into strain energy in Femtojoule (fJ). The strain energy was determined in the red circle, surrounding the acinus. The acinus applied strain energy to the substrate already during the rolling phase, 10 hours prior to invasion onset, the measured strain energy was 120 fJ. The first invasive cells were observed 25 hours after the transfer (invasion onset). The disseminating cells are marked by red outlines in phase contrast images. Further cells followed by collective cell migration and invaded the substrate. The generated stress by MCF10A acinus gradually increased up to invasion onset to 230 fJ. The invading cells applied gradually more strain energy to the substrate over the following 10 hours after the invasion onset, reaching 600 fJ at 10 hours post invasion onset.

To validate the accuracy of the determined strain energy produced by MCF10A acini, additionally, the cell-free positions were analyzed. For each individual invasive acinus, the baseline strain energy level at the cell-free position from the same experimental run and at the same time point was investigated. The corresponding baseline strain energy was plotted in the same graph as the strain energy generated by acini.

First, hd-BM acini were analyzed (see Figure 3.20). From the graph it could be observed that the median strain energy generated by acini, slightly increased over time on both substrate rigidities. But also the median of the baseline strain energies at cell-free positions revealed a slight increase over time. This increase was more prominent on 0.12 kPa substrates (0.1 fJ, 10 h prior to invasion onset - 2 fJ, 10 h post invasion onset), while the median baseline strain energy on 12 kPa stayed constant over time (0.6 fJ, 10 h prior to invasion onset - 1 fJ, 10 h post invasion onset). Although the scatter of the baseline strain energy on 12 kPa reached maximal values of 8 fJ, and on 0.12 kPa values of 3 fJ, in general, the median baseline strain energies were below the corresponding median strain energies applied by acini in the same experiment. Overall, the strain energy exerted by the analyzed hd-BM acini groups was higher on tumor-like stiff ECM (12 kPa), compared to the strain energy applied by the same BM-group acini on normal-like stiff ECM (0.12 kPa). The median strain energy on 0.12kPa, 10 hours prior to invasion was around 2 fJ. This value was 10-fold lower, compared to the strain energy generated by the same BM-group acini on 12 kPa (20 fJ). The median of applied strain energy increased to around 3 fJ on 0.12 kPa substrates, and to 26 fJ on 12 kPa substrates, 5 hours prior to invasion onset. At the time of invasion onset, the median strain energy applied by hd-BM acini on 0.12 kPa was 3 fJ, and 33 fJ on 12 kPa, 11-fold higher. After the invasion onset, the median strain energy on 0.12 kPa substrates increased to 11 fJ, 5 hours after the invasion onset, and to 27 fJ, 10 hours after the invasion onset. On 12 kPa substrates, the median strain energy was 65 fJ, 5 hours after the invasion onset, and 111 fJ, 10 hours after the invasion onset. While in general, the strain energies increased on both substrates over time, the initial 10-fold difference of applied strain energy on different substrate rigidities decreased to 4-fold difference, 10 hours after the invasion onset (27 fJ on 0.12 kPa compared to 111 fJ on 12 kPa). The differences in generated strain energies at the same investigation time points between two substrate rigidities were statistically significant.

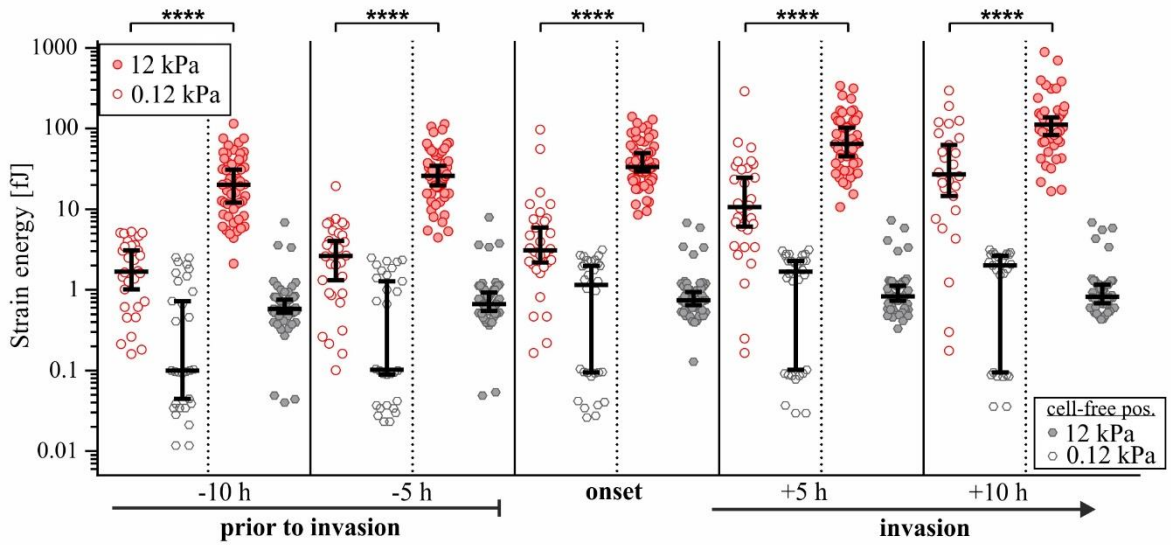

Figure 3.20: Strain energy generated by hd-BM acini compared to the baseline strain energy level at the cell-free control position.
The strain energies generated by invasive hd-BM acini on 0.12 kPa (n = 30) and 12 kPa (n = 54) substrates were compared at different stages of invasion: 10 and 5 hours prior to invasion, at invasion onset, and 5 and 10 hours after the invasion onset. The strain energy values were plotted logarithmically (log_{10}). On 0.12 kPa substrates, the median strain energy increased from 2 fJ 10 hours prior to invasion onset, to 3 fJ at the invasion onset, and further to 27 fJ, 10 hours after the invasion onset. Compared to 0.12 kPa substrates, on 12 kPa, the initial strain energy was 10-fold higher: 20 fJ 10 hours prior to invasion onset. Here, the strain energy increased to 33 fJ at invasion onset, and further to 111 fJ, 10 hours after the invasion onset. Mann-Whitney-Test: ****: $p < 0.0001$. The baseline strain energy values were recorded at the same time points of invasion stage, from the corresponding cell-free positions in the individual experimental runs. In general the median strain energy values produced by MCF10A acini were clearly above the median of the detected baseline strain energies. Scatter bars: median with 95 % confidence interval.

For a better comparison between the MCF10A acini groups, in following, the measured strain energy applied by MCF10A acini to the substrate was standardized. Hereby, the ratios of the generated strain energy produced by acini and the corresponding baseline strain energy from the cell-free positions were calculated for each time point (acini generated strain energy was divided by the baseline strain energy). The baseline strain energy divided by itself, provided a threshold of 1 for lower ratio border. Acini with a strain energy ratio lower than 1 were not included in the data analyses. In general, the strain energy applied by acini was higher than the baseline strain energy. Only 4 hd-BM acini generated strain energy values that were below the measured uncertainty range of the measurement.

The strain energy ratios at the designated time points in hd-BM acini (invasion onset, 5 and 10 hours prior to and post invasion onset) were plotted as scatter dot plots using individual time points of each invasive MCF10A acinus (see Figure 3.21). Data analysis revealed that on both substrate rigidities, the median strain energy ratio in hd-BM acini was nearly constant during

the rolling phase, up to the invasion onset. In detail, acini facing soft substrates (0.12 kPa), generated median strain energy ratios of 13, 10 h prior to invasion onset, 7, 5 h prior to invasion onset, and 7 at the invasion onset. At the same time points, the median strain energy ratios were in mean 5-fold higher on 12 kPa substrates during the rolling phase. Here the median strain energy ratios were 34, 10 h prior to invasion onset, 36, 5 h prior to invasion onset, and 48 at the invasion onset. After the invasion onset, on 0.12 kPa substrates, the median strain energy ratios increased to 14, 5 hours after the invasion onset and to 28, 10 hours after the invasion onset. On 12 kPa substrates, the median strain energy ratios were 6-fold higher 5 hours after the invasion onset (80), and 4-fold higher 10 hours after the invasion onset (104), compared to the respective groups on 0.12 kPa substrates.

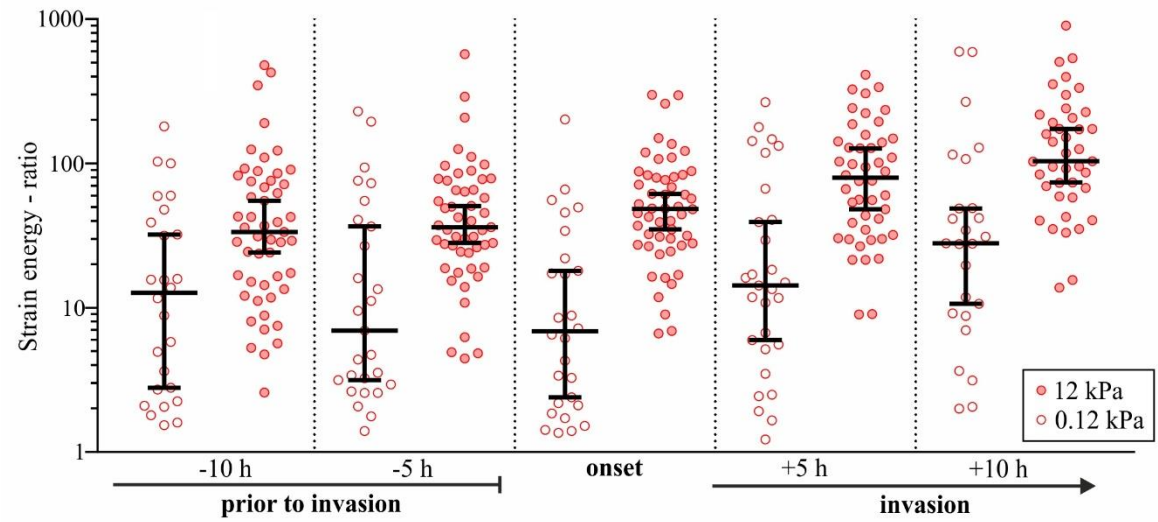

Figure 3.21: Strain energy ratios generated by invasive hd-BM MCF10A acini.
Strain energy ratios in EGF-stimulated (20 ng/mL) hd-BM acini were plotted logarithmically (log_{10}). The strain energy ratios were compared at different stages of invasion. On both substrates the median strain energy ratios were constant during the rolling phase and visibly increased after the invasion onset. The strain energy ratios on 12 kPa were in mean 5-fold higher over time, than on 0.12 kPa substrate at the corresponding time points. Scatter bars: median with 95 % confidence interval.

Next, ld-BM acini were investigated. Also in these groups the cell-free positions were analyzed. For each individual invasive acinus, the baseline strain energy at the cell-free position from the same experimental run and at the corresponding time point was investigated. The baseline strain energies were plotted in the same graphics as the strain energies generated by ld-BM acini (see Figure 3.22). Similar to hd-BM groups, also in ld-BM groups the strain energy readily increased over the investigation time on both substrate rigidities, 0.12 kPa and 12 kPa. And also here, the median baseline strain energy at cell-free positions slightly increase over time, which was more prominent on 0.12 kPa substrates (0.1 fJ, 10 h prior to invasion onset – 0.4 fJ, 10 h post invasion onset). Notably, the median baseline strain energy on 12 kPa was higher than in all other groups, and also slightly increased over time (1 fJ, 10 h prior to invasion onset - 3 fJ, 10 h post invasion onset). The maximum scatter of the baseline strain energy on 12 kPa reached values of up to 7 fJ, and on 0.12 kPa values of up to 3 fJ. However, in general, the baseline strain energy was below the strain energy applied by acini in the corresponding experimental runs.

Overall, also in ld-BM acini, the generated strain energies were higher on tumor-like stiff matrix (12 kPa), compared to strain energies on normal-like stiff matrix (0.12 kPa). In these groups, the median strain energy on 0.12kPa, 10 hours prior to invasion was around 1 fJ. At the same time point of invasion stage, the median strain energy on 12 kPa was 35 fJ. Thus, the applied strain energy by ld-BM acini on stiff substrates (12 kPa) seemed to be 35-fold higher than on 0.12 kPa substrates. This fold change difference was more than doubled when directly compared to hd-BM acini group (see Figure 3.20, compare to Figure 3.22). Further in ld-BM acini the median of applied strain energy slightly increased to around 2 fJ on 0.12 kPa substrates, and to 37 fJ on 12 kPa substrates, 5 hours prior to invasion onset. At the time of invasion onset, the median strain energy applied by ld-BM acini on 0.12 kPa was doubled to 4 fJ. The strain energy on 12 kPa at the invasion onset increased to 50 fJ, and was thereby 13-fold higher than on 0.12 kPa matrix. After the invasion onset, the median strain energy on 0.12 kPa substrates increased further to 12 fJ, 5 hours after the invasion onset, and to 25 fJ, 10 hours after the invasion onset. On 12 kPa substrates, the median strain energy was 80 fJ, 5 hours after the invasion onset, and 105 fJ, 10 hours after the invasion onset. The differences in generated strain energies at the same investigation time points between two substrate rigidities were statistically significant.

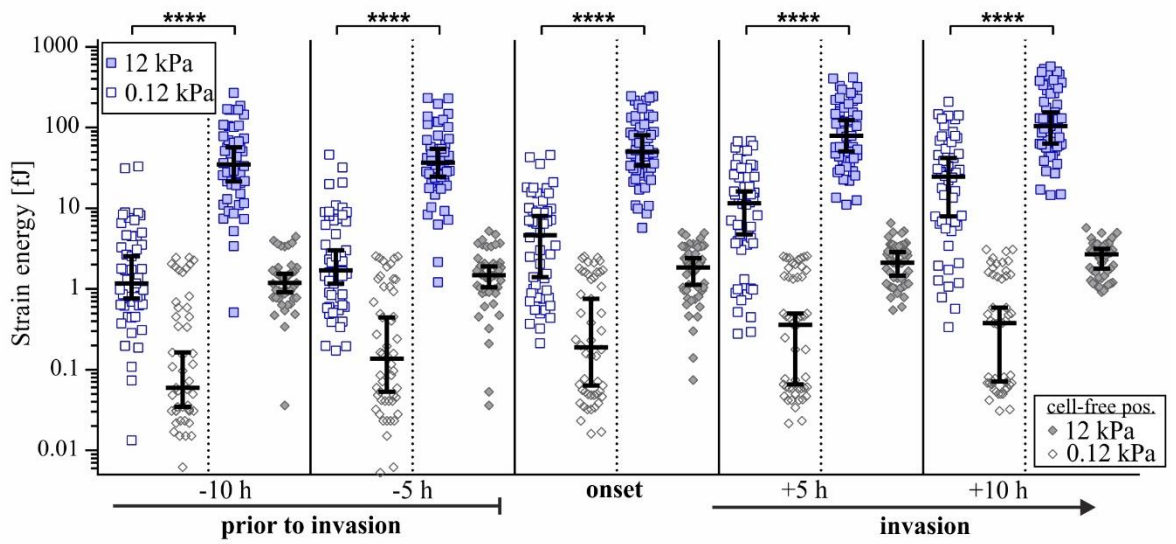

Figure 22: Strain energy generated by ld-BM acini compared to the baseline strain energy level at the cell-free control position.
The strain energies generated by invasive ld-BM acini on 0.12 kPa (n = 50) and 12 kPa (n = 52) substrates were compared at different stages of invasion: 10 and 5 hours prior to invasion, at invasion onset, and 5 and 10 hours after the invasion onset. The strain energy values were plotted logarithmically (log_{10}). On normal-like stiff substrates (0.12 kPa), the median strain energy increased from around 1 fJ 10 hours prior to invasion onset, to 4 fJ at the invasion onset, and further to 25 fJ, 10 hours after the invasion onset. On tumor-like stiff substrates (12 kPa) in general a similar increase of strain energy was observed. But in contrast to 0.12 kPa substrates, on 12 kPa, the initial median strain energy was 35-fold higher: 35 fJ 10 hours prior to invasion onset. Here, the median strain energy increased to 50 fJ at invasion onset, and further to 105 fJ, 10 hours after the invasion onset. Mann-Whitney-Test: ****: $p < 0.0001$. The baseline strain energy levels were recorded at the same time point of invasion stage, from the corresponding cell-free position in the individual experimental run. In general the median strain energy produced by MCF10A acini was clearly above the median of the detected baseline strain energy. Scatter bars: median with 95 % confidence interval.

Also the data obtained for ld-BM acini on normal-like stiff ECM (0.12 kPa) and on tumor-like stiff ECM (12 kPa) were standardized (see Figure 3.23). In these groups no sphere were excluded, as in all acini the strain energy ratios exceeded the threshold of 1. Analysis of the data revealed that on both substrates, the median strain energy ratios in hd-BM acini, similar to ld-BM acini, were nearly constant during the rolling phase, up to invasion onset. On 0.12 kPa the median strain energy ratios were 10, 10 h prior to invasion onset, 11, 5 h prior to invasion onset, and 13 at the invasion onset. In comparison, at the same time points, the strain energy ratios on 12 kPa substrates were in mean 2-fold higher: 22, 10 h prior to invasion onset, 24, 5 h prior to invasion onset, and 27 at the invasion onset. On both substrates the strain energy ratios remained constant up to invasion onset. After the invasion onset, median strain energy ratios increased to 20, 5 hours- and to 50, 10 hours after the invasion onset, on 0.12 kPa substrates. On 12 kPa substrates, the median strain energy ratios were 42, 5 hours after the invasion onset, and 50, 10 hours after the invasion onset. In this BM-acini sample group, after the invasion

onset, as cells disseminated on the substrates, the median strain energy ratios approximated and were identical.

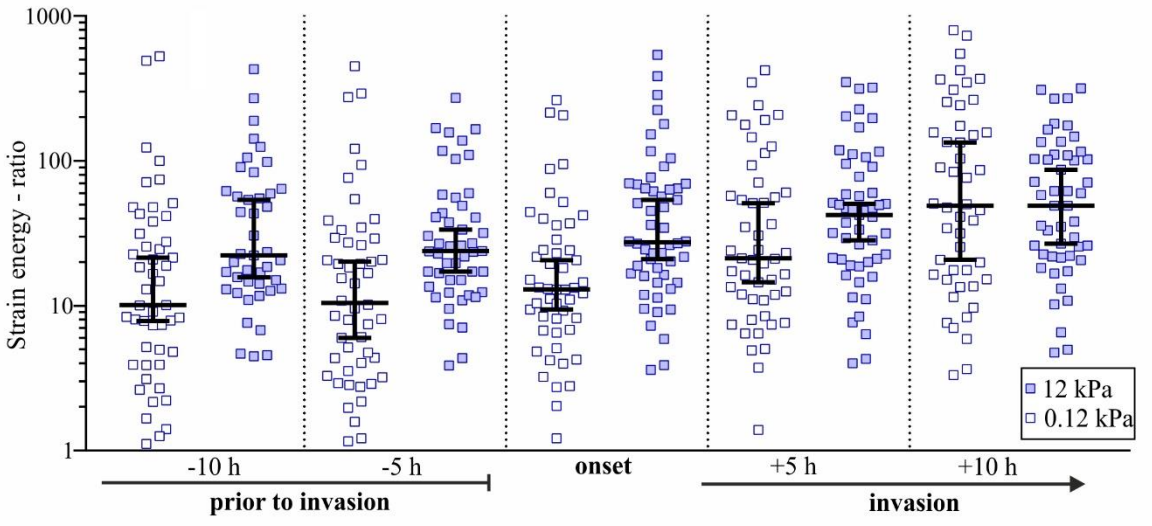

Figure 3.23: Strain energy ratios generated by invasive hd-BM MCF10A acini.
Strain energy ratios in EGF-stimulated (20 ng/mL) ld-BM acini were plotted logarithmically (log_{10}). The strain energy ratios were compared at different stages of invasion. On both substrates the median strain energy ratios were constant during the rolling phase and increased after the invasion onset. Thereby, the strain energy ratios on 12 kPa were in mean 2-fold higher over time up to 5 hours after invasion onset, than on 0.12 kPa substrate at the corresponding time points. As cells disseminated on the substrate after the invasion onset, median strain energy ratios between the substrate rigidities were nearly identical. Scatter bars: median with 95 % confidence interval.

These data revealed a significant association between cellular strain energy generation and tumor-related ECM stiffening from normal-like (0.12 kPa) towards tumor stroma (12 kPa) resembling rigidity. Both, acini with ld-BM and hd-BM showed reduced strain energies exerted to the substrate which stiffness lain in the range of healthy breast gland tissue (0.12 kPa).

In contrast to previous observations made on invasion course and outcome in the same MCF10A acini groups, where the state of the basement membrane dominated over the substrate rigidity (see Section 3.3.2), here the developmental state of the basement membrane seemed to be not directly related to strain energy amplitudes exerted by acinar cells onto the elastomeric substrates.

3.5.3. Strain energy applied by MCF10A acini during the early rolling phase

Previous experiments on invasive acini (see Section 3.5.2) have revealed that at those stages of invasion process, no substantial increase of strain energy amplitude took place among the groups during the rolling phase (10 and 5 hours prior to invasion onset). This raised the question whether the cell-matrix interactions take place much earlier in the rolling phase.

Resting and invasive acini from the EGF-stimulated MCF10A acini groups were analyzed on their ability to apply strain energy to the substrate during the early rolling phase, 5 and 10 hours directly after the transfer of MCF10A acini onto the elastomeric substrates (see Figure 3.24). Also for these time points the baseline strain energies from the cell-free control positions were measured. Since the two analyzed time points were identical between all acini, from the three individual experimental runs, three cell-free positions were available. The exception was the hd-BM group on 0.12 kPa, here no data were available for the time point 5 hours after the transfer (since the experiment could not be started earlier, due to technical problems). Therefore, for this group only two experimental measurements are given for the investigation time point 5 hours after the transfer.

Similar to previous observations during the invasive phase of MCF10A acini, the baseline strain energies were below the strain energies produced by acini from the corresponding experimental runs. Interestingly, during the early rolling phase, 5 hours after the transfer, ld-BM and hd-BM acini on 0.12 kPa exerted similar low median strain energies to the soft substrate, 0.01 fJ and 0.02 fJ, respectively. The baseline strain energy values were below 0.004 fJ. In contrast, the median strain energy produced by the same BM-groups on stiffer substrates (12 kPa) was significantly higher. In ld-BM groups the median strain energy applied by acini was 9 fJ, and 0.1 fJ in hd-BM acini, respectively. Notably, the median strain energy in ld-BM acini on tumor like stiff matrix (12 kPa) was 93-fold higher than the median strain energy in hd-BM group on the same matrix stiffness, and more than 1000-fold higher than in the same BM-group on normal-like stiff matrix (0.12 kPa). On 12 kPa substrates, the baseline strain energy values were also higher than on 0.12 kPa, ranging between 0.01 fJ and 0.3 fJ. The baseline strain energy values on both substrate rigidities increased during the next 5 hours, but notably were in a similar range in all groups, but not higher than 1 fJ. The median strain energies generated by acini also increased during the following 5 hours on the substrates. Thus, 10 hours after acini transfer, ld-BM acini on 0.12 kPa soft substrates generated median strain energy of 0.4 fJ, showing a 40-fold increase in strain energy generation than 5 hours earlier. The generation of median strain energy was not as high in hd-BM acini on 0.12 kPa substrates, but increased to 0.1 fJ, 10 hours after the transfer, showing a 5-fold increase compared to the applied median

strain energy 5 hours after the transfer. In ld-BM acini on 12 kPa, the median strain energy increased nearly 4-fold, to 33 fJ, compared to 5 hours after the transfer. In hd-BM acini on 12 kPa substrates, the median strain energy 10 hours after the transfer was measured to be 4 fJ, 39-fold higher than 5 hours earlier.

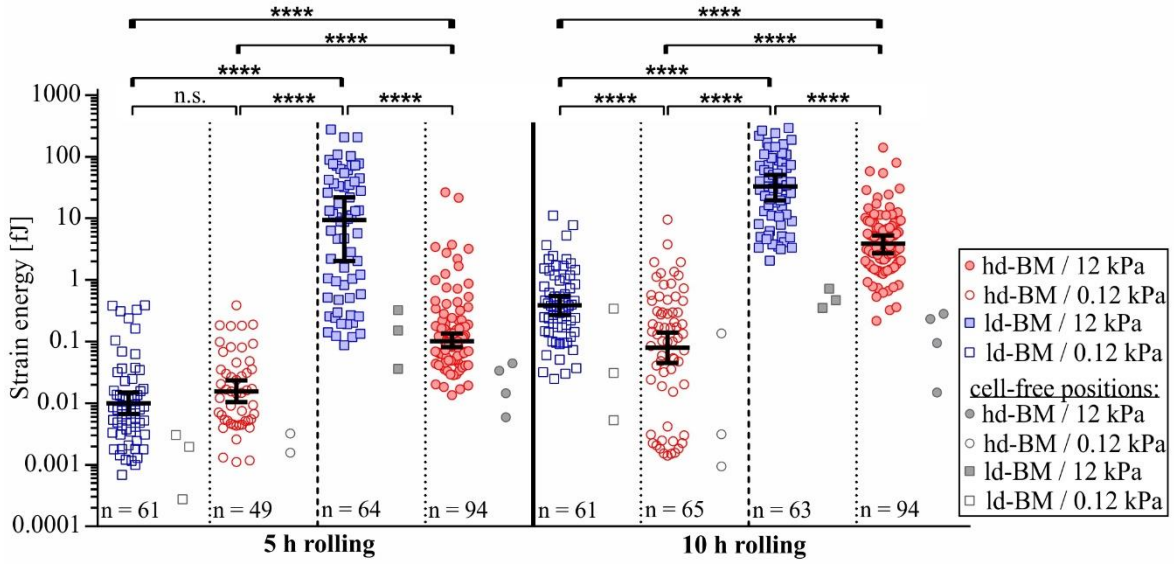

Figure 3.24: Strain energy produced by MCF10A acini during the rolling phase.
The strain energies generated by MCF10A acini during the rolling phase and the corresponding baseline strain energies from the cell-free control positions were plotted logarithmically (log_{10}). The analyzed numbers of acini (n) are indicated in the graph. In all four groups the median strain energies increased between 5 and 10 hours after the transfer. The strain energies produced by ld- and hd-M acini on 12 kPa substrates were higher than on 0.12 kPa substrates in the corresponding groups. Also the baseline strain energies at the corresponding cell-free positions increased between the two analyzed time points. Mann-Whitney-Test: ****: $p < 0.0001$. n.s.: $p > 0.05$. Scatter bars: median with 95 % confidence interval.

Also the data from the early rolling phase were standardized (see Figure 3.25). In general, 5 hours after the transfer, the median strain energy ratios in ld-BM (8) acini and hd-BM (6) acini on 0.12 kPa, as well as hd-BM (6) acini on 12 kPa were nearly identical, while the median strain energy ratio in ld-BM acini on 12 kPa (50) was 6-fold and 8-fold higher, respectively. After further 5 hours on the substrates, the median strain energy ratios in both BM-groups on 0.12 kPa substrate did not substantially change: 10 in ld-BM acini, and 6 in hd-BM acini. Notably, nearly a 7-fold increase of the median strain energy ratio could be observed in hd-BM acini on 12 kPa, from 6 to 40 (in-between the two analyzed time points). The median strain energy ratio in ld-BM acini on tumor-like stiff matrix increased to 70.

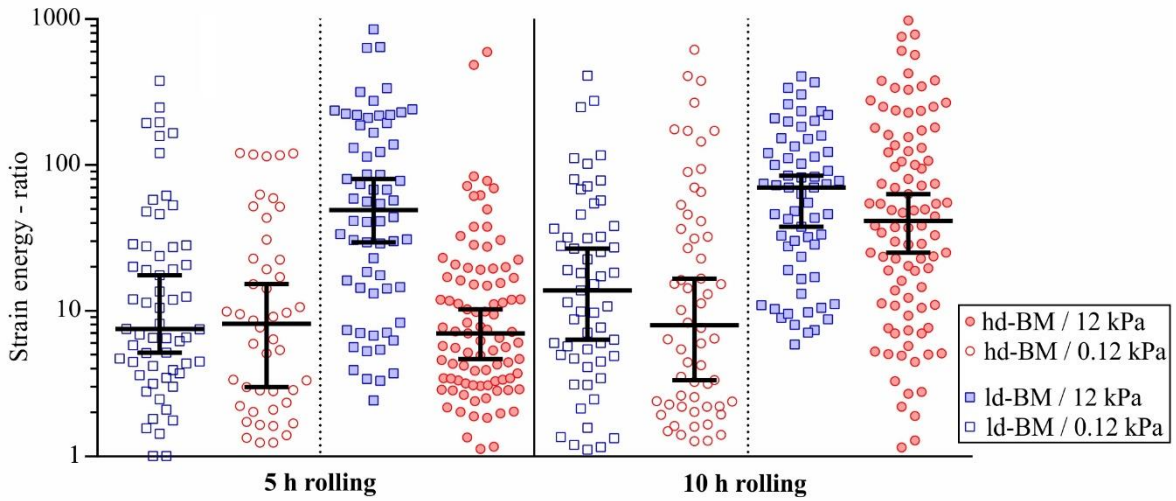

Figure 3.25: Strain energy ratios generated by MCF10A acini during the early rolling phase. Strain energy ratios in EGF-stimulated (20 ng/mL) acini were plotted logarithmically (log_{10}). Strain energy ratios between the two time points of the early rolling phase, 5 and 10 hours after acini transfer, were compared. Ld-BM acini on 12 kPa showed significantly higher strain energy ratios compared to other groups, 5 hours after the transfer. Following further 5 hours on the substrates, hd-BM acini on 12 kPa reached a similar median strain energy ratio as ld-BM acini on the same ECM stiffness. Scatter bars: median with 95 % confidence interval.

Overall, while globally comparing all MCF10A acini groups of the tumor progressing series (see Section 3.3.2), the influence on strain energy generation by developmental state of the BM seemed to be oppressed by substrate rigidity. Only during the early rolling phase, a clear and significant influence of the basement membrane state on rigid (tumor-like) substrate was noted. These data revealed that in the early rolling phase, 5 hours after the transfer, ld-BM and hd-BM acini on normal-like matrix applied significantly lower strain energies to the substrate than on tumor-like stiff substrates. The highest strain energy was generated by the most pathological group, ld-BM acini on 12 kPa. The fact that hd-BM acini on 12 kPa generated less strain energy than ld-BM acini leads to the assumption, that at this time point of the rolling phase, the basement membrane functions as a kind of buffer, which becomes less significant during further 5 hours of the rolling phase. From these data, it could be deduced, that after 10 hours on the substrates, generation of the strain energy is mainly influenced by substrate rigidity, while the state of the basement membrane plays only an important role during the early rolling phase, 5 hours after the first contact with the substrate.

3.6. Investigation of vertical cell-ECM interactions in MCF10A acini

TFM measurements revealed that MCF10A acini with ld-BM on stiff matrix had the strongest interactions with the ECM during the early rolling phase (see Section 3.5.3). It is known that filopodia, finger-like protrusions are responsible for environmental sensing [82]. This led to the hypothesis that the previously observed cellular actin-rich protrusions reaching through the basement membrane (see Section 3.2, Figure 3.3 A) might be involved in the early interactions with the underlying ECM. While TFM is a powerful method to measure tangential (x-y) substrate deformations, it has limited sensitivity in measuring the applied stress in vertical (z) direction. Therefore, in cooperation with Dr. N. Kronenberg and Prof. M. Gather from St Andrews, UK, ERISM was used as a method to investigate the acinar interactions in z-direction with the substrate during the early rolling phase. In the following experiments MCF10A acini groups that showed the highest interactions with the ECM in TFM during the rolling phase were chosen: ld-BM and hd-BM acini on stiff matrix, stimulated with EGF.

Observations of acini with differently developed basement membrane on ERISM substrates with a stiffness of 3 kPa, revealed effective vertical interactions of acini with the substrate. In Figure 3.26, representative image sequences of vertical substrate interactions of an ld-BM and an hd-BM acinus are shown in comparison over time. In general, all MCF10A acini started to rotate in place on the substrate after the transfer, as already demonstrated by TFM, which took place during the rolling phase (see Section 3.2). Simultaneously, local spot-like substrate deformations underneath the acini were detected by ERISM. These acinar substrate interactions were not static, but highly dynamic. The observed deformations were visible as local pushing (dark-violet spots) and pulling (bright-yellow spots) events. Hereby, pushing of the substrate was recorded as a negative value, while pulling on the substrate was recorded as a positive value. The non-deformed substrate at the cell-free area around the acinus provided the zero point reference. Pushing of acinar structures into the substrate was accompanied by pulling on the substrate. To visualize the structures more clearly, broad features were removed via spatial Fourier filter (right column in Figure 3.26 A and B). This revealed fine and restricted pushing and pulling sites.

In ld-BM acini vertical substrate deformations were detected earlier than in hd-BM acini. In the representative ld-BM acinus (shown in Figure 3.26 A) the first vertical substrate deformations started already about 1.5 hours after the transfer. Simultaneous pushing and pulling of the substrate could be observed in a range of up to 25 nm (see Figure 3.26 A, upper row). Compared to the ld-BM acinus, in the representative hd-BM acinus (shown in Figure 3.26 B) similar

substrate displacements starter clearly later during the rolling phase. In the represented hd-BM acinus in Figure 3.26 B (upper row), 4.5 hours after the transfer, the observed pushing and pulling reached values of up to 12 nm, 2-fold lower than in ld-BM acinus after 1.5 hours. At a similar time point, 5 hours after the transfer, in the ld-BM acinus (Figure 3.26 A, central row) the deformation spots became larger (than 3.5 hours earlier), and displacements slightly increased to 30 nm. During further 2.5 hours on the substrate, ld-BM acinus generated substrates displacements of up to 50 nm (see Figure 3.26 A, lower row). In contrast, in hd-BM acinus, the substrate deformations remained very weak (about 12 nm) even after 16 hours on the substrate (see Figure 3.26 B, central row). Similar substrate deformations, as those seen in the ld-BM acinus, 7.5 hours after the transfer, were observed in the represented hd-BM acinus after 26 hours on the substrate (see Figure 3.26 B, lower row).

In addition, a general note became evident during the analyses of ERISM data. These data revealed that MCF10A acini cells in fact invaded the substrate a bit earlier than previously determined by phase contrast images in the 3D invasion assay (as described in Sections 3.3 and 3.4). However, these cells remained underneath the acinus, not visible in phase contrast images. Due to preliminary low number of analyzed acini by ERISM, this observation could not be statistically verified yet.

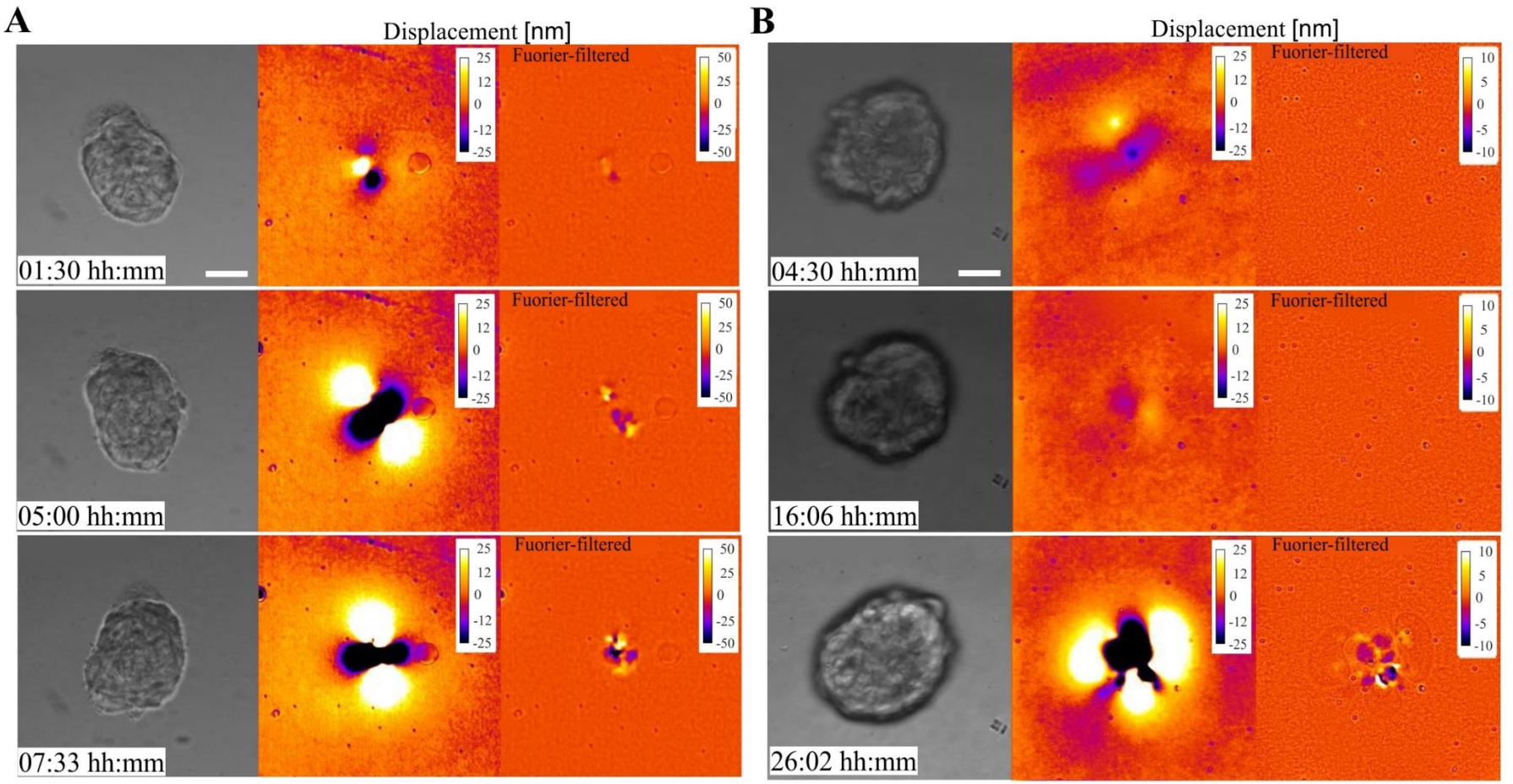

Figure 3.26: ERISM comparisons of cell-substrate interaction in ld-BM and hd-BM MCF10A acini.
MCF10A acini were transferred onto ERISM substrates and stimulated with 20 ng/mL EGF. Cell-substrate interactions were observed over a period of up to 28 hours. Representative acini are shown in phase contrast, together with substrate displacements in ERISM and spatial Fourier filtered ERISM. Substrate displacements were recorded as negative values through pushing (dark spots) or as positive values through pulling (bright spots) on the substrate. Non-deformed substrate (orange) served as zero-reference. **A.** Ld-BM acini showed intensive interactions with the substrate in the early rolling phase. The displaced volume directly underneath the acini increased over time. **B.** Substrate interactions in hd-BM acini were visible in the late rolling phase. Displacements of the substrate steadily increased. Scale bars = 25 µm. Figures were prepared from image sequences kindly provided by Dr. N. Kronenberg, St Andrews, UK.

Preliminary evaluation of ERISM data, focusing first on the pushing events during acinar interactions with the substrates over time, revealed that there are three characteristic phases of pushing in MCF10A acini. The first phase that could be observed among acini was characterized by weak, hardly visible interactions with the substrates, and was designated as the rolling phase. This phase was followed by phase 2, characterized by highly dynamic focal interactions of acinar structures with the substrate, visible as deep local substrate deformations. In phase 3 the first cells disseminating on the substrates became visible. These migrating cells induced broad areal substrate deformations.

Further, the duration of each phase and the displaced volume (total volume by which acinar structures indent into the substrate, as a proxy for the applied force [118]) of the substrate were observed and compared between both BM-groups (see Figure 3.27 and Figure 3.28). In ld-BM acini (see Figure 3.27 A), in eight of 11 acini the measurements were started later than 5 hours after the transfer. By this time, most of those acini were already in the second or even in the third phase. Thus, in those acini, phase 1 seemed to take place during the first 5 hours after the transfer. In the other four of 11 ld-BM acini, phase 1 was observed to end between three and 13 hours on the substrates. Thereby the displaced volume was measured to be between 0.3 and 29 μm^3.

Six of the analyzed 11 acini entered phase 2 during the observation time. One of those acini remained in phase 2 during the entire investigation time. In three other acini, phase 2 ceased 5.5, 12 and 19 hours after the transfer. The other two acini did not enter phase 3 during the investigation time. In phase 2 the displaced volume was in the range of 10 μm^3.

Fife of 11 analyzed ld-BM acini were in phase 3 during the entire investigation time. In those acini phase 1 and phase 2 seemed to have had happened in the period directly after the transfer, earlier than 5.5 hours after the transfer. Acini that have entered phase 3 during the investigation time, showed volume displacements in the range of 30 and 164 μm^3.

Hd-BM acini (see Figure 3.27 B) remained in phase 1 in mean about 15 hours after the transfer and generated volume displacements below 2 μm^3. Phase 2 was relatively short in hd-BM acini (between 0.5 and 5 hours), and was rapidly followed by phase 3. In phase 2, substrate displacement were in the range of 1 and 23 μm^3. In phase 3 the displaced volume was between 20 and 480 μm^3.

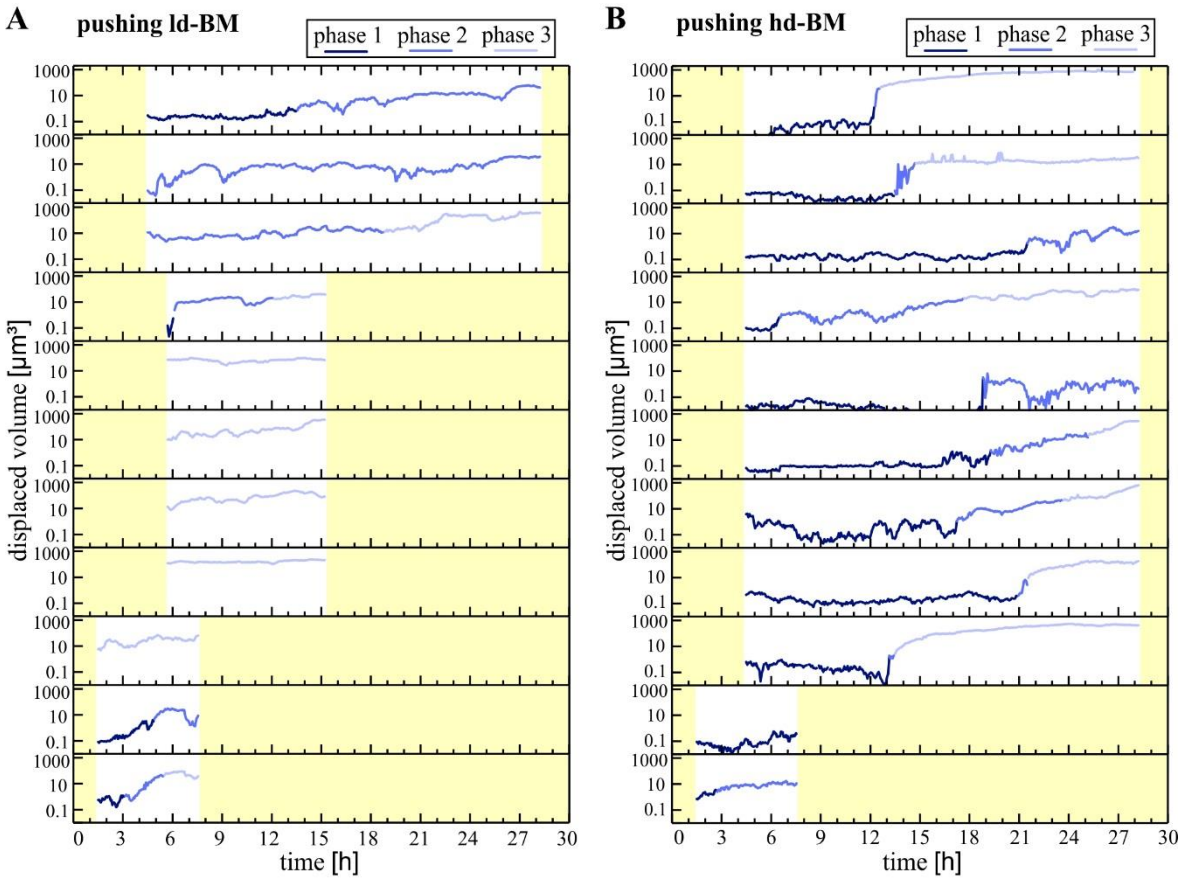

Figure 3.27: Different phases of substrate deformations produced through pushing by MCF10A acini.
Courses of the three pushing phases in ld-BM (n=11) and hd-BM (n=11) acini were compared. The displaced volume was plotted logarithmically (log_{10}). **A.** In ld-BM acini phase 1 (acini rolling phase) was relatively short-lived. Most of the analyzed ld-BM acini were in the phase 2 (focal interactions) or phase 3 (cell dissemination). **B.** In hd-BM acini phase 1 was quite prominent and lasted up to 21 hours after the transfer. Here phase 2 was short-lived rapidly followed by phase 3. Graphics were kindly provided by Dr. N. Kronenberg, St Andrews, UK.

In following, the median displaced volume during the individual phases (from Figure 3.27) were compared between ld-BM and hd-BM acini (see Figure 3.28). In hd-BM acini the median of displaced volume in phase 1 was 0.1 µm^3, and in ld-BM acini 0.3 µm^3, 3-fold higher. In phase 2, the median displaced volume rapidly increased, in hd-BM acini to 3 µm^3, and to 7 µm^3 in ld-BM acini. Thus, in phase 2 ld-BM acini displaced 2-fold more substrate volume than hd-BM acini. In phase 3 the first disseminating cells on the substrate became visible. These cells induced deformation by pushing on the substrate with a displaced volume being in median 64 µm^3 in ld-BM acini and 86 µm^3 in hd-BM acini.

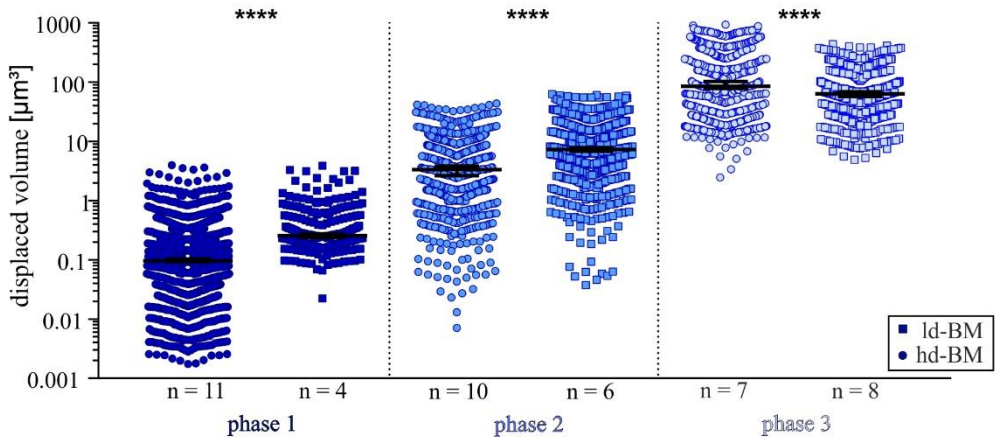

Figure 3.28: Displaced volume by pushing on the substrate by MCF10A acini in individual phases of invasion.
Ld-BM and hd-BM MCF10A acini (the number of analyzed acini is indicated in the graph) were analyzed by ERISM. The median displaced volume, in vertical direction, directly underneath the acini was calculated and separated into three phases. The values from each time point interval were plotted logarithmically (log_{10}). Phase 1 was characterized by weak interactions of acini with the substrate. In phase 2 local substrate deformations resulted in increased displaced volume. In phase 3, several cells escaped from the acinus, further increasing the displaced volume. Scatter bars: median with 95 % confidence interval. Mann-Whitney-Test: ****: $p < 0.0001$.

Overall, ERISM measurements revealed that ld-BM acini established the first cell-matrix interactions clearly earlier than hd-BM acini. Local deformations of the substrate directly underneath the acini suggest that those deformations are produced by cellular protrusions, leading to the hypothesis that the thin protrusions observed in MCF10A acini might be responsible for the detected vertical substrate deformations.

4. Discussion

The human breast cancer is the most frequently diagnosed cancer among women. And besides many research foundations that made significant contributions for a better diagnosis of breast cancer and its early treatment, this malignancy is still the leading cause of cancer deaths worldwide [129]. Thereby, it is not the primary tumor, but cells that disseminated from the original lesion and formed secondary tumors at distant organs, metastases, which account for the majority of deaths from cancer [130]. While treatment of the early breast cancer achieves good results, clinically it is more difficult to manage metastases [131]. An improved understanding of the mechanical and biophysical mechanisms of the early metastatic process would contribute to identification of novel targets that could be used to facilitate an effective therapy and might hinder a malignant tumor from invading the adjacent tissue [9].

The invasion in breast cancer is a highly coordinated process between cancer cells and their microenvironment [80]. In the past decades the basement membrane gained a crucial role as regulator of cell behavior as it is known to define tumor microenvironment and to regulate signals during tumor progression [30,44]. However, the factors that induce cellular transformations and cell invasion through the basement membrane are still not fully understood. There is upcoming evidence that cell invasion through the basement membrane is influenced by a three-way-crosstalk between stromal stiffening, growth factor signaling, and epithelial cytoskeletal contractility [12].

The aim of this thesis was to analyze biophysical properties of the basement membrane as a barrier to invasive cells. The spontaneously immortalized, non-transformed, human mammary epithelial cell line MCF10A has been proven as a good model for 3D experiments, as it exhibits many properties of normal breast tissue [100]. Especially with respect to the basement membrane, MCF10A acini represent a powerful tool to study the mechanical and biophysical properties of the basement membrane *in vitro* [33].

Factors promoting breast cancer invasion through the basement membrane

In a healthy tissue, an intact basement membrane provides structural support and separates the tissue of its origin from the adjacent stroma, while in cancer, the basement membrane is often found to be fragmented [132]. Initially, epithelial tumors evolve from normal epithelium and progress to a tumor *in situ* (DCIS) while remaining enclosed by the basement membrane [4]. This situation was perfectly mimicked by selected hd-BM acini, since in those acini thick basement membrane was shown to be continuously arranged around the acini, resembling the healthy state, while the lumen was not formed yet. In the context of breast cancer, the ld-BM acini with a thin basement membrane matched the pathological state of the mammary gland in which the basement membrane deposition is often perturbed, resulting in a less cross-linked meshwork that can be more easily degraded and remodeled [120].

To be able to analyze the individual contribution of stromal stiffening, growth factor signaling, and epithelial cytoskeletal contractility, first of all it was necessary to find out whether the non-transformed MCF10A acini can acquire an invasive phenotype. Radically changing the environmental factors in MCF10A acini with a weak basement membrane (ld-BM), such as tumor-resembling ECM stiffness (12 kPa) and aberrant growth factor stimulation (with EGF), which are known to be involved in promoting malignancy [47,122], confirmed this fact in the initial experiment. However, it was not possible to conclude to which extent the applied tumor promoting factors contributed individually to the observed invasive phenotype. Therefore, the influence of these factors on induction of an invasive phenotype in MCF10A acini will be discussed separately in the following sections.

4.1.1. Effects of extracellular matrix stiffness

It is known that cancer invasion is upregulated by increased substrate stiffness [133], which in turn has been identified to be associated with breast cancer risk [122]. Therefore, in this thesis the effect of substrate stiffness was analyzed on its ability to induce an invasive phenotype in MCF10A acini depleted of further exogenous invasion promoting factors, such as EGF. Observations of ld-BM and hd-BM acini on 0.12 kPa and 12 kPa substrates revealed an increase of invasive phenotype in both BM-groups on stiffer matrices. Thereby also the healthy state of the basement membrane showed a significant impact on invasion outcome, by arresting the invasive cells.

The mammary gland is surrounded by loose connective and adipose tissues, representing a compliant tissue with a Young's modulus of around 170 Pa [121]. Thus, to mimic the ECM

stiffness of the normal mammary gland, the elastomeric silicone rubber with an elastic modulus of 120 Pa used in this thesis, ideally matched the soft ECM of the human breast. *In vivo*, the tissue stiffness changes with age, but also during tumorigenesis [52]. Also the breast cancers are characterized by increasing stiffness of the ECM and are therefore frequently detected by palpation [121,122]. Thus, to mimic the tumor-like ECM rigidity, the used elastomeric silicone rubber with an elastic modulus of 12 kPa ideally fitted the reported Young's modulus in low grade invasive ductal carcinoma of 10.4 ± 2.6 kPa (mean ± standard deviation) [58].

Cells in a tissue constantly sense the stiffness of their microenvironment (ECM), which in turn is a critical player in regulation of cell behavior and determination of normal cell functions and tissue homeostasis [52,134]. Cellular sensing and response to ECM stiffness are performed through dynamic regulation of integrin clustering, which leads to focal adhesion formation and remodeling of the actin filaments [135]. Integrins are the cue mechanisms to probe the matrix, they can adhere to their specific ligands on a substrate and direct migration [75]. Hence, upon ligand binding on the ECM, integrins recruit different adhesion proteins which link integrins to the actin cytoskeleton and initiate formation of adhesion structures [77]. The maturation of focal adhesions is directly affected by matrix stiffness and results in generation of larger forces [74,79]. Thus, stiffening of the ECM strongly contributes to cell migration, and can result in cancer cell invasion and dissemination through increased force generation [136]. This mechanism of stiffness regulated focal adhesion maturation and cytoskeletal force generation is known as reinforcement [116]. In line with this, several studies could already demonstrate that stiff matrix has profound effects on mammary epithelial cells through promoting proliferation and invasion in MCF10A acini [121,123,137,138]. Increased matrix stiffness was shown to disrupt acini formation and polarization during their differentiation [121]. Additionally, stiff matrix induced integrin clustering and activated focal adhesion kinases [59,121] which promote invasion and proliferation [137]. Although in the mentioned studies MCF10A cells were stimulated with EGF, the observed effect of ECM stiffening matches the observations made in this thesis on EGF-depleted MCF10A acini. Here, increasing matrix stiffness to tumor-resembling stiffness of 12 kPa, increased the number of invasive acini.

The phenomenon that in absence of EGF, MCF10A acini disseminated rather on rigid than on soft substrates argues for an EGF-independent mechanosensing mechanism.
A recent study has found epidermal growth factor receptor (EGFR) to be active in substrate rigidity sensing on stiff (17.2 kPa) surfaces, thus regulating cellular functions like proliferation

even in the absence of EGF [139]. EGFR is a transmembrane receptor for extracellular protein ligands of the EGF-family, and under physiological conditions is a key regulator of a variety of cellular functions, including differentiation, proliferation and migration [140]. The mechanosensing mechanisms of EGFR are unknown [141]. But given the fact that EGFR are often found to be overexpressed in cancers, understanding their mechanosensing process is critically important to cancer progression [141]. It was therefore recently postulated that the ligand-independent activation of EGFR might be caused by integrins [141], as they are known to interact with growth factor receptors (GFRs) during cell spreading and migration, and they can directly activate GFRs in the absence of a ligand [139,142]. It was found that binding of integrin α6 to its ligand laminin during adhesion mimics the effect of EGF stimulation in a stiffness-dependent manner in breast cancer cells [141]. Given the fact that MCF10A cells are EGFR positive [143], this hypothesis of ligand-independent rigidity sensing mechanism regulated by EGFR can be adopted to the observations made in this thesis on stiffness induced invasion in MCF10A acini in absence of EGF. The facts that EGFR localizes to integrin adhesions more on rigid than on soft substrates [139], and low substrate rigidity is described to downregulate protein expression and phosphorylation of focal adhesion complexes [144], can be adopted to explain low invasion incidence in MCF10A acini observed on soft substrates in this thesis.

In addition to the substrate stiffness, in this thesis, for the first time the state of the basement membrane was demonstrated to have a large impact on invasion outcome in MCF10A acini. Although several studies have already demonstrated that MCF10A cell invasion can be triggered by stiff matrix, those studies either neglected the basement membrane by culturing the cells as monolayers (2D assays) [123] or equated the ECM (often represented by EHS matrix mixed with varying concentrations of type I collagen) with the endogenous basement membrane and focused only on the invasive phenotype of the cells or acini [121,138]. By means of the 3D *in vitro* invasion assay using MCF10A acini as a model, in this thesis it was possible to certainly differentiate between the endogenous basement membrane and the underlying ECM. This allowed to look on the outcome of invasion in MCF10A acini regulated by the basement membrane integrity. Accordingly, the data suggest that despite substrate stiffness, the state of the basement membrane has an enormous impact on invasion, as more acini were retained from invasion in hd-BM acini compared to ld-BM acini on the same substrate rigidities. The observed invasion and dissemination of MCF10A acini on the elastomeric substrates require the cells to penetrate through the compact basement membrane [145]. Previously, it was

shown that tumor cells can migrate through small pores, but their migration is limited to a pore size being in the range of 3 μm^2 [146] and 7 μm^2 [65,147] in the human mammary breast carcinoma cell line MDA-MB-231. Based on permeability properties of the basement membrane, in our recent work, we conducted that the basement membrane in hd-BM MCF10A acini has a pore size in the range of 9 nm in diameter [33], while in her doctoral thesis, a co-worker Dr. Gloria Fabris, has optically identified the mean pore size in ld-BM MCF10A acini to be in the range of 0.2 μm^2 [148]. These findings implicate that the invasive MCF10A acini cells observed in this thesis cannot freely migrate through the pores of the basement membrane and must acquire a motile phenotype [12]. Cellular migration under space restriction has been shown to be strongly dependent on proteolytic degradation of the basement membrane to enlarge the pore size [65].

In this thesis, small cellular actin-rich protrusions were observed in MCF10A acini reaching through the pores of the basement membrane. These novel finding suggests that those structures might be filopodia or filopodia-like protrusions. Filopodia are described as highly dynamic finger-like protrusions that are responsible for environmental sensing [82]. Emerging evidence suggests that there might be several subtypes of filopodia in a 3D environment, each fulfilling a different function [82]. One of those functions could be the proteolytic degradation by MMPs of the ECM through switching of filopodia to invadopodia [83]. Invadopodia are described as invasive finger-like protrusions, which are capable of proteolytically degrading the ECM [83]. Formation of invadopodia is stimulated by stiffened ECM [12]. Additionally, proteolytic degradation of the basement membrane can generate or release cryptic fragments which can act as growth stimulators and facilitate invasion [34]. Thus, for example cleavage of laminin-γ2 chain with MMP14 generates an EGF-like fragment. This fragment was shown to promote epithelial cell proliferation and migration [149]. Given the fact that MCF10A acini endogenously produce laminin-332, which is the only functional laminin that contains a γ2 chain, possible proteolytic activity of MMPs, induced by stiff matrix, might activate this kind of migration mechanism, via EGF-like signaling, even in the absence of EGF in medium.

In summary, it can be hypothesized that higher invasion outcome seen in ld-BM acini on a tumor-like stiff matrix might come along with stiffness induced reinforcement of focal adhesion formation. At focal adhesions, integrins might activate EGFR in a ligand-independent manner, which in turn might induce a motile phenotype of acinar cells. Simultaneously, filopodia-like protrusions in those cells might sense the stiff matrix and activate proteolytic degradation of the basement membrane, finally leading to invasion of acinar cells through the generated

physical space in the basement membrane. Low substrate stiffness down-regulates the expression of focal adhesion complex proteins [144]. This might explain the lower number of invasion events in ld-BM acini on normal-like substrates. In hd-BM acini on tumor-like stiff matrix the same process might take place as in ld-BM acini on the same stiffness, but with the exception that invasive cells might need longer to break down the thicker basement membrane, which in this case functions as a barrier to invasive cells. Under the most physiological conditions only one single acinus invaded the substrate. This might be a result of a soft ECM, which does not promote invasion, and a healthy basement membrane, which in addition retains the cells from invasion.

4.1.2. Effects of epidermal growth factor

Previous experiments have shown that the stiffness of the substrate alone can trigger an invasive phenotype. So in the next experiments is was analyzed whether this invasion of MCF10A acini can be further increased by exogenous stress. To test this, MCF10A acini under tumor progressive scenarios were additionally stimulated with aberrant concentration of EGF. The results revealed an increase of invasive phenotype in all groups (ld-BM and hd-BM acini on 0.12kPa and 12 kPa, respectively). Interestingly, the stiffness of the substrate did not have the same influence on invasion as in EGF-depleted acini. Instead, the state of the basement membrane conducted the invasion outcome independent on substrate rigidity. Thereby, thick basement membrane slowed down the invasion onset and reduced the invasion outcome.

One possible mechanism of increased invasion in MCF10A acini might be the EGF induced disruption of hemidesmosomes [150]. The primary function of hemidesmosomes in epithelial tissue is to maintain the tissue integrity. Their main component is the heterodimer receptor α6β4 integrin. Under normal conditions, this heterodimer has been shown to be localized to the basal site in MCF10A acini, where hemidesmosomes connect epithelial cells to the basement membrane [121]. The localization of this heterodimer at the basement membrane was also demonstrates in this thesis. Cellular stimulation with EGF was reported to stimulate a rapid disassembly of hemidesmosomes [151]. In this thesis, staining of the hemidesmosomal protein α6 integrin at a late stage of acinar invasion, validated the distribution of this integrin throughout the cell. Moreover, mobilization of α6β4 integrin from hemidesmosomes in response to EGF is thought to enable its incorporation into F-actin protrusions, such as filopodia [151]. Additionally, stimulation of cells with 10 ng/mL - 250 ng/mL EGF has been

shown to induce phosphorylation of the β4 integrin subunit in squamous carcinoma cells [150], thus leading to disassembly of hemidesmosomes and activation of signaling pathways influencing migration and invasion in carcinoma cells [107,151]. The used EGF concentration of 20 ng/mL in this thesis to stimulate invasion in MCF10A acini lies perfectly in this range. This leads to the assumption that the same mechanism might be activated in MCF10A acini upon EGF stimulation.

The fact that upon stimulation of MCF10A acini with EGF, the rigidity of the substrate had no impact on invasion outcome, might also be associated with the used EGF concentration. EGF is described to shift the cells from contact-inhibited to contact-independent proliferation, which is a property of cancer cells [123]. Thereby soft substrates favor contact inhibition, but strongly depend on EGF concentration. Thus, upon a certain threshold of EGF concentration, contact inhibition on soft substrates is reduced, leading to contact-independent proliferation. For MCF10A clusters in a 2D assay, the EGF threshold was identified to be 10 ng/mL on 7 kPa and 0.1 ng/mL on 31 kPa substrates [123]. The used EGF concentration in this thesis was clearly above these reported thresholds, while the used substrate rigidities were either in-between (12 kPa) or clearly below (0.12 kPa) the ones described. Additionally, in our recent study, we could show, that MCF10A acini in 3D culture are highly sensitive to EGF concentrations [33]. Therefore, the results of this thesis suggest, that stimulation of MCF10A acini with 20 ng/mL EGF, either on 0.12 kPa or on 12 kPa substrates, leads to a turning-off of the cellular mechanosensing mechanisms, and induces contact-independent proliferation that finally might lead to invasion of the cells through the basement membrane.

The observed later invasion in hd-BM acini might be connected to the further function of EGF in cell invasion, namely its ability to induce invadopodia formation. In case invadopodia are active in MCF10A acini, this could be a possible explanation for the later invasion onset in hd-BM acini. Here the invasive structures might need longer to proteolytically digest the thick basement membrane compared to ld-BM acini with a thin basement membrane.

In summary, stimulation of MCF10A acini with aberrant EGF concentration, has clarified the functional role of the basement membrane as a barrier to invasive cells, most likely by turning-off the mechanosensing of acinar cells.

4.1.3. Effects of proteolytic degradation of the basement membrane

Former experiments led to the assumption that during acinar invasion, proteolytic cleavage of the basement membrane by MMPs might take place. To prove this assumption, the most physiological group of MCF10A acini with hd-BM on a compliant matrix (0.12 kPa) were purposely proteolytically weakened by type IV collagenase, to identify whether the basement membrane indeed plays a gatekeeper role during invasion. The results revealed a complete loss of the basement membrane function in retarding the cells from invasion. In contrast to this experiment, the involvement of proteolytic digestion of the basement membrane in invasive MCF10A acini was proven by inhibition of MMPs. Treatment of MCF10A acini in all four groups with marimastat decreased the invasion outcome in all acini groups. Thereby, stimulation with EGF seemed to play a significant role in promoting invasion.

Under physiological conditions, MMPs are responsible for remodeling of the basement membrane and the extracellular matrix, for example during tissue growth [89]. However, dysregulation or increased expression of MMPs has been observed in many cancers, leading to their direct contribution to cancer progression [90]. During cancer invasion, cells proteolytically disrupt the basement membrane. At those sites, the basement membrane was shown to be lost. And in turn, loss of basement membrane is thought to directly stimulate cellular invasive behavior [66]. These findings are perfectly in line with the results from this thesis, as purposely weakened basement membrane by type IV collagenase has led to 100 % invasion events in MCF10A acini with a thick basement membrane on a compliant substrate. MMP-2 and MMP-9 belong to the family of type IV collagenases, and their increased expression has been discovered in many cancer types, including breast cancer. Moreover, a positive correlation between MMP-2 and -9 activity or expression and the invasive tumor potential has been found [89]. The crucial contribution of those MMPs to initiating invasion, could be successfully demonstrated in this thesis, using the type IV collagenase, thereby identifying their possible role in metastasis initiation [89].

In contrast, inhibition of MMPs by the broad-spectrum MMP inhibitor marimastat revealed a clear decrease of invasive events in MCF10A acini, thereby strengthening the assumption, that the basement membrane of MCF10A acini is effectively cleaved by MMPs during invasion. Since secretion of MMPs is interconnected to formation of invadopodia [12], the findings of this thesis implicate that the observed cellular protrusions in MCF10A acini might be invadopodia or invadopodia-like protrusions. Both, invadopodia formation and MMP secretion are stimulated and induced by EGF [12]. This correlates with the experimental procedure in

this thesis, as during MMP inhibition, MCF10A acini were simultaneously stimulated with EGF.

The fact that the invasion events in MCF10A acini were not completely diminished by marimastat, might come along with compensation mechanisms [152]. Also other studies have experienced similar results after blocking the MMPs. Moreover, MMP inhibitors failed in clinical trials [90]. This implicates other mechanisms to be involved in inducing cellular transmigration through the basement membrane. Therefore, it is assumed, that proteolytic compensation takes place by other enzymes, not inhibited by the MMP inhibitors [152]. Since other ECM modifying enzymes such as heparanase, cathepsins or urokinase plasminogen activator were also shown to be upregulated in breast tumors [131], it can be assumed that in this work the activity of those proteinases might be activated by aberrant EGF stimulation as well. In support to this hypothesis, EGF depleted ld-BM acini on stiff matrix, treated with marimastat showed nearly a complete diminishment of invasive phenotype in MCF10A acini. This result supports previous assumptions that EGF is responsible for secretion of MMPs and other proteases, and subsequent induction of cell invasion. The low number of acini that invaded the substrate despite MMP inhibition and absence of EGF, might suggest a switch of migration mode from integrin-dependent mesenchymal mode, to amoeboid type of migration, which do not require proteolytic activity [152,153]. The amoeboid movement has been proposed to be a compensatory mode of invasion, taking place when proteolysis is inhibited [11,152].

In summary, these results lead to the hypothesis that upon stimulation with EGF, the basement membrane in MCF10A acini is proteolytically cleaved by MMPs. But, in absence of EGF, another, compensatory mechanism, stimulated by stiff matrix are used by cells to breach the basement membrane.

4.1.4. Effects of mechanotransduction pathway inhibition

Previous results from this thesis have demonstrated that MCF10A acini are capable to sense the mechanical properties of the ECM and to respond by mechanotransduction, initiating invasion on stiff substrates. Additionally, invasive potential of MCF10A acini could be increased by EGF stimulation, simultaneously turning-off the mechanosensitivity of the cells. Therefore, it was aimed to identify a possible mechanotransduction pathway being responsible for promoting the invasive phenotype in MCF10A acini.

As already discussed above, MCF10A acini form hemidesmosomes, containing α6β4 integrins, which are critical to normal acini formation [154,155]. Additionally, however, α6β4 integrin

has been shown to play a significant role in activating signaling pathways, influencing migration and invasion in epithelial and carcinoma cells [151]. One of the most important signaling molecules regulated by α6β4 in respect to migration is phosphoinositide 3-kinase (PI3K) [151]. PI3K is a key molecule in signaling for invasion in carcinoma cells [107], and its activation seems to depend on phosphorylation of the β4 subunit [150,156]. Stimuli such as EGF, in addition to induction of hemidesmosomal dissociation, increase phosphorylation of β4 [151]. In turn, phosphorylated β4 subunit is thought to activate PI3K [40]. Under physiological conditions, PI3K mediates downstream signal transduction of extracellular stimuli through diverse signaling pathways, which regulate different cellular events, including proliferation, apoptosis and cell migration [106,157]. PI3K was reported to be up-regulated in human breast cancers and its signaling cascade leads to tumor growth [157,158].

In this thesis, immunofluorescent staining of the α6 integrin at a late stage of acinar invasion under EGF-stimulation, revealed dislocation of this hemidesmosomal subunit. This is in line with previous studies, which could already demonstrate that EGF stimulation triggers destruction of hemidesmosomes and re-localization of α6β4 to filopodia and other actin-rich protrusions. This finding and knowledge from literature, encouraged to analyze the involvement of PI3K in inducing the invasive phenotype in MCF10A acini.

Temporal treatment of EGF-stimulated ld-BM acini on tumor-like stiff matrix with PI3K inhibitor wortmannin, indeed resulted in a time dependent decrease of invasion events. In total, 10% less acini were invasive and in general the invasion onset was similar to the hd-BM acini on normal-like stiff substrate. These findings are in line with a previous study, where overexpression of PI3K has been demonstrated to be involved in activation of malignant phenotype in MCF10A acini [138]. Additionally, hemidesmosomal re-localization has been shown to take place in MCF10A acini on a stiff matrix, also triggered by the PI3K pathway [138]. Moreover, PI3K activity is described to be required for invadopodia formation in invasive human breast cancer cells [106]. Inhibition of PI3K in this study, might therefore be connected to indirect inhibition of invadopodia formation in MCF10A acini. This could explain the timed delay of observed invasion, as inhibited invadopodia were not able to produce MMPs to degrade the basement membrane. In line with this hypothesis is a recent work which gives insight about a novel signaling mechanism, in which MMP2 expression is induced by PI3K pathway in human breast cancer [159].

4.1.5. Effects of mechanotransduction and actomyosin contractility

Measurements of the strain energy generated by MCF10A acini during the invasion phase revealed, that acini, independent on the basement membrane state, generated significantly higher strain energy on tumor like than on normal-like stiff substrates, during the rolling phase and up to invasion onset. Thereby the applied strain energy slightly increased in all acini groups over the entire observation time. Interestingly, in addition to substrate rigidity, the influence of basement membrane state seemed to play an important role during the early rolling phase. Here, 5 hours after the transfer, ld-BM acini on stiff substrates generated significantly higher strain energy than other acini groups. Additionally, analyses of the rolling phase by ERISM revealed that in ld-BM acini the rolling phase was shorter than in hd-BM acini. During this time, the interactions with the substrate were short-lived and very dynamic. These findings can be explained by substrate interactions via integrins, the cue mechanisms to probe the matrix that can adhere to the substrate and direct migration [75]. Hence, upon ligand binding on the ECM, integrins recruit different adhesion proteins which link integrins to the actin cytoskeleton and initiate formation of first but short-lived adhesion structure, termed nascent adhesions [77]. Most probably, the measured short-lived interactions with the substrate seen in ERISM in this thesis, are this kind of adhesion structures, to probe the substrate. Since these substrate interactions were visible as spot-like structures, they might be derived from the actin rich protrusions, seen in MCF10A acini, which are able to reach through the basement membrane. As already described above, those structures could be filopodia or filopodia-like protrusions. In the literature, filopodia are described to be responsible for environmental sensing, and are also discussed to trigger mechanical responses by traction force production [82]. The observed pushing and pulling events in ERISM in this thesis can also be connected to the presence of protrusive structures, since they are described to promote pushing during protrusion, and pulling during retraction [160]. Although the bindings in nascent adhesions are short-lived and weak, cells are able to exert contractile forces of a low magnitude on the substrate [79]. In response to this forces, nascent adhesions either undergo fast turnover during active protrusions (pushing and pulling seen in ERISM) or start to grow and elongate into mature focal adhesions recruiting other proteins [77]. The maturation of nascent adhesions into focal adhesions is directly affected by matrix stiffness [79]. Additionally, in the literature normal mammary epithelial cells are described to produce higher force on a stiff, than on a soft ECM [51]. Thus, this knowledge can be adopted to explain higher strain energy generated by MCF10A acini on stiffer matrix determined by TFM.

However, upon adhesion formation, invasive cells cannot just use their actomyosin machinery to pull them out of the acinus, due to the small pore size of the basement membrane. Thus, the cells first have to overcome the basement membrane as a physical barrier [65]. The exact mechanism of matrix degradation at this stage in a 3D environment is not fully understood yet. But, in cancer cells increased density of filopodia is considered to be characteristic for invasive cancer cells in 3D [75,76,82]. Interestingly, it was suggested that filopodia might become invasive and are then represented by invasive finger-like protrusions called invadopodia, which are capable to proteolytically degrade the ECM [83]. In case of invadopodia formation, matrix-degrading enzymes are recruited to the sites of integrin mediated adhesion, allowing local, contact-dependent proteolytic degradation of the basement membrane [65,80]. As in ld-BM acini the basement membrane is thinner, the degradation process might be faster, compared to hd-BM acini. This could be a possible explanation for the shorter rolling phase seen in ld-BM acini in ERISM. Upon degradation of the basement membrane, the cells break through by actomyosin-mediated contraction, thereby generating forces to the substrate [65]. The magnitude of generated forces is coupled with matrix stiffness. Consequently, increased stiffness of the substrate results in increased focal adhesion assembly and generation of larger forces [74,79]. Moreover, force-induced assembly of stable focal adhesions was reported to enhance PI3K signaling, which further activates intracellular signaling that leads to invasion of cancer cells [161].

The observation by TFM, that no influence of the basement membrane was detected up to 10 hours prior to invasion and during the invasion onset, can be explained by the fact that the invasion onset was set as the point of origin, and the basement membrane, most likely, was already digested by MMPs at this time point, and had no further barrier function.

In summary, it can be hypothesized that after the transfer of MCF10A acini onto elastomeric substrates, the observed actin-rich protrusions, presumably filopodia, might be responsible for mechanosensing. Most likely, this sensing was detected by ERISM. In case the ECM has a tumor-like stiffness, cells generate higher forces and acquire an invasive phenotype. In the next step those cells probably produce invadopodia which proteolytically cleave the basement membrane to generate larger pores for cells to escape. In ld-BM acini the basement membrane is thinner, and therefore can be cleaved faster. Hence, a thin basement membrane is an easier to overcome physical barrier for invasive cells. Therefore, the basement membrane represents a physical and mechanical barrier to invasive cells at the beginning of the invasion process.

4.2. Conclusion

In this work for the first time the interplay between growth factor signaling, actin cytoskeleton contraction and matrix stiffening was analyzed in the human mammary gland acini, using MCF10A cells as *in vitro* model. These factors are thought to promote cancer development and understanding their contribution in breast cancer progression would facilitate the treatment of the disease.

In this thesis it could be demonstrated, that in absence of external tumorigenic factors, such as EGF, substrate stiffness alone was able to induce an invasive phenotype in the non-tumorigenic MCF10A acini. These findings indicate that cells in an acinus are able to sense the substrate rigidity. It is assumed, that this sensing takes place via the observed actin-rich protrusions reaching through the basement membrane, presumably representing filopodia-like protrusions. Moreover, ERISM measurements suggest that those protrusions interact with the underlying substrate, generating measurable stress through pushing and pulling on the substrate. This is a novel finding in mammary gland acini indicating that the acinar cells are constantly sensing the substrate rigidity through the basement membrane and in turn are also able to respond to it via activation of mechanosensitive intracellular signaling pathways. The results of this thesis suggest that PI3K might be an important upstream signaling player activated by EGFR, leading to proliferation, invadopodia formation and MMP production, thereby inducing invasion. This emphasizes the crucial role of EGFR, and its overexpression seems to be a more critical parameter in breast cancer progression than a stiff matrix, because in this thesis, cellular mechanosensing seemed to be over-written by aberrant stimulation with EGF, and increased invasion. Thereby, a healthy basement membrane had a large impact on cellular breakthrough and invasion as a physical and mechanical barrier, retaining the invasive cells, thus enhancing the importance of an intact basement membrane in breast cancer.

4.3. Future perspectives

In this thesis, the integrity of the basement membrane was demonstrated to play a critical gate keeping role during breast cancer invasion. Thereby, proteolytic enzymes were shown to be involved in a general mechanism of membrane degradation, which initiated invasion. It would be interesting to non-proteolytically destroy the basement membrane, for example by local laser ablation. This would help to uncover whether the destruction of the basement membrane is a reversible process. This knowledge might be helpful to find out how a disrupted basement membrane could be treated *in vivo* to prevent metastasis at the early stage

Further, in this thesis actin-rich cellular protrusions were observed reaching through the basement membrane. The experimental data lead to the hypothesis that these protrusions might be filopodia which can turn into invadopodia during the invasion progression. In connection with these results, it would be interesting to more closely analyze and to characterize the type of the observed protrusions. By selecting appropriate marker proteins, immunofluorescent stainings would be a helpful method to identify the involved structural proteins. Possible marker proteins to identify filopodial structures would be fascin and myosin-X [76], while cortactin, TKS5 and MMP14 are described as invadopodial markers [162]. Stainings at different stages of acini invasion could be used to determine whether those protrusions indeed can switch their mode from filopodia to invadopodia. Additionally, it would be interesting to look at histological sections derived from breast cancer patients to determine, whether a similar kind of protrusions is also present *in vivo*. Eventually, the frequency of those protrusions or staining of their specific structural proteins might be used clinically as a prognostic marker to predict the outcome of the lesion.

Additionally, the observed protrusions seemed to sense and deform the underlying substrate. Therefore, it would be interesting to analyze the MCF10A acini on other substrate rigidities by ERISM and to compare their dynamics and the displaced volume, as the acini showed different behavior, generating higher strain energy on stiffer substrates during TFM analyses. Additionally, in this thesis PI3K was shown to be involved in mechanotransduction mechanisms. Therefore, it would be interesting to inhibit PI3K during the ERISM and TFM measurements to verify, that the formation of those protrusion and their activity are directed via PI3K signaling pathway and identify whether the measured forces generated by these protrusions can be diminished through inhibition of PI3K signaling pathway. In this context, also other inhibitors acting in early formation of actin protrusions would be interesting to be

analyzed, to detect which proteins are involved, thereby additionally helping to identify the nature of these protrusions.

Changes of the microenvironment were shown to change cellular behavior. This indicates, that cells have to adopt to the exogenous forces via changing their gene expression. Therefore, it would be interesting to analyze how the different exogenous forces, like increased stiffness or EGF stimulation, change the expression profile of MCF10A acini during invasion. This gene expression analysis would help to identify potential marker proteins that in turn could be used as targets in therapy.

5. References

1. Ferlay J, Soerjomataram I, Dikshit R, *et al.* (2015) Cancer incidence and mortality worldwide: sources, methods and major patterns in GLOBOCAN 2012. International Journal of Cancer 136: E359-86.
2. Torre LA, Islami F, Siegel RL, Ward EM, Jemal A (2017) Global Cancer in Women: Burden and Trends. Cancer Epidemiol Biomarkers Prev 26: 444-57.
3. Malvezzi M, Carioli G, Bertuccio P, *et al.* (2018) European cancer mortality predictions for the year 2018 with focus on colorectal cancer. Ann Oncol 29: 1016-22.
4. Mallon E, Osin P, Nasiri N, *et al.* (2000) The basic pathology of human breast cancer. J Mammary Gland Biol Neoplasia 5: 139-63.
5. Key TJ, Verkasalo PK, Banks E (2001) Epidemiology of breast cancer. Lancet Oncol 2: 133-40.
6. Schlehe B, Schmutzler R (2008) [Hereditary breast cancer]. Chirurg 79: 1047-54.
7. Pathak DR, Osuch JR, He JP (2000) Breast carcinoma etiology - Current knowledge and new insights into the effects of reproductive and hormonal risk factors in black and white populations. Cancer 88: 1230-8.
8. Husmann G, Kaatsch P, Katalinic A (2010) Krebs in Deutschland 2005/2006-Häufigkeiten und Trends. Berlin: Robert Koch-Institut und die Gesellschaft der epidemiologischen Krebsregister in Deutschland e. V.
9. Weigelt B, Peterse JL, van 't Veer LJ (2005) Breast cancer metastasis: markers and models. Nat Rev Cancer 5: 591-602.
10. Scully OJ, Bay BH, Yip G, Yu Y (2012) Breast cancer metastasis. Cancer Genomics Proteomics 9: 311-20.
11. Rowe RG, Weiss SJ (2008) Breaching the basement membrane: who, when and how? Trends Cell Biol 18: 560-74.
12. Chang TT, Thakar D, Weaver VM (2017) Force-dependent breaching of the basement membrane. Matrix Biol 57-58: 178-89.
13. Inman JL, Robertson C, Mott JD, Bissell MJ (2015) Mammary gland development: cell fate specification, stem cells and the microenvironment. Development 142: 1028-42.
14. Hassiotou F, Geddes D (2013) Anatomy of the human mammary gland: Current status of knowledge. Clin Anat 26: 29-48.
15. Russo J, Russo IH (2004) Development of the human breast. Maturitas 49: 2-15.
16. Vidi PA, Bissell MJ, Lelievre SA (2013) Three-dimensional culture of human breast epithelial cells: the how and the why. Methods Mol Biol 945: 193-219.
17. Watson RJ, Eyden BP, Howell A, Sellwood RA (1988) Ultrastructural observations on the basal lamina in the normal human breast. J Anat 156: 1-10.
18. Royer C, Lu X (2011) Epithelial cell polarity: a major gatekeeper against cancer? Cell Death Differ 18: 1470-7.
19. Godde NJ, Galea RC, Elsum IA, Humbert PO (2010) Cell polarity in motion: redefining mammary tissue organization through EMT and cell polarity transitions. J Mammary Gland Biol Neoplasia 15: 149-68.
20. Brennan K, Offiah G, McSherry EA, Hopkins AM (2010) Tight junctions: a barrier to the initiation and progression of breast cancer? J Biomed Biotechnol 2010: e460607.
21. Farquhar MG (1963) Junctional Complexes in Various Epithelia. The Journal of cell biology 17: 375-412.
22. Schwarz MA, Owaribe K, Kartenbeck J, Franke WW (1990) Desmosomes and hemidesmosomes: constitutive molecular components. Annu Rev Cell Biol 6: 461-91.
23. Borradori L, Sonnenberg A (1996) Hemidesmosomes: roles in adhesion, signaling and human diseases. Curr Opin Cell Biol 8: 647-56.

24. Diedrich K, Holzgreve W, Jonat W, *et al.* (2007) Gynäkologie und Geburtshilfe. Heidelberg: Springer Medizin Verlag.
25. Morandi A, Taddei ML, Chiarugi P, Giannoni E (2017) Targeting the Metabolic Reprogramming That Controls Epithelial-to-Mesenchymal Transition in Aggressive Tumors. Front Oncol 7: 40.
26. Rayat CS, Joshi K, Sakhuja V, Datta U (2005) Glomerular basement membrane thickness in normal adults and its application to the diagnosis of thin basement membrane disease: an Indian study. Indian J Pathol Microbiol 48: 453-8.
27. Yurchenco PD (2011) Basement membranes: cell scaffoldings and signaling platforms. Cold Spring Harb Perspect Biol 3.
28. Welling LW, Zupka MT, Welling DJ (1995) Mechanical-Properties of Basement-Membrane. News in Physiological Sciences 10: 30-5.
29. Candiello J, Balasubramani M, Schreiber EM, *et al.* (2007) Biomechanical properties of native basement membranes. FEBS J 274: 2897-908.
30. Kalluri R (2003) Basement membranes: structure, assembly and role in tumour angiogenesis. Nat Rev Cancer 3: 422-33.
31. LeBleu VS, Macdonald B, Kalluri R (2007) Structure and function of basement membranes. Exp Biol Med (Maywood) 232: 1121-9.
32. Ferrell N, Cameron KO, Groszek JJ, *et al.* (2013) Effects of pressure and electrical charge on macromolecular transport across bovine lens basement membrane. Biophys J 104: 1476-84.
33. Gaiko-Shcherbak A, Fabris G, Dreissen G, *et al.* (2015) The Acinar Cage: Basement Membranes Determine Molecule Exchange and Mechanical Stability of Human Breast Cell Acini. PloS one 10: e0145174.
34. Xu R, Boudreau A, Bissell MJ (2009) Tissue architecture and function: dynamic reciprocity via extra- and intra-cellular matrices. Cancer Metastasis Rev 28: 167-76.
35. Freedman BR, Bade ND, Riggin CN, *et al.* (2015) The (dys)functional extracellular matrix. Biochim Biophys Acta 1853: 3153-64.
36. Miller RT (2017) Mechanical properties of basement membrane in health and disease. Matrix Biol 57-58: 366-73.
37. Dingemans KP (1988) What's new in the ultrastructure of tumor invasion in vivo? Pathol Res Pract 183: 792-808.
38. Pozzi A, Yurchenco PD, Iozzo RV (2017) The nature and biology of basement membranes. Matrix Biol 57-58: 1-11.
39. Khoshnoodi J, Pedchenko V, Hudson BG (2008) Mammalian collagen IV. Microsc Res Tech 71: 357-70.
40. Stewart RL, O'Connor KL (2015) Clinical significance of the integrin alpha6beta4 in human malignancies. Lab Invest 95: 976-86.
41. Halfter W, Candiello J, Hu H, *et al.* (2013) Protein composition and biomechanical properties of in vivo-derived basement membranes. Cell Adh Migr 7: 64-71.
42. Wu X, Chen G, Qiu J, *et al.* (2016) Visualization of basement membranes in normal breast and breast cancer tissues using multiphoton microscopy. Oncol Lett 11: 3785-9.
43. Rejon C, Al-Masri M, McCaffrey L (2016) Cell Polarity Proteins in Breast Cancer Progression. J Cell Biochem 117: 2215-23.
44. Tanjore H, Kalluri R (2006) The role of type IV collagen and basement membranes in cancer progression and metastasis. Am J Pathol 168: 715-7.
45. Xu R (2017) Mammary epithelial polarity and macrophage infiltration. Macrophage (Houst) 4.
46. Gonzalez-Conchas GA, Rodriguez-Romo L, Hernandez-Barajas D, *et al.* (2018) Epidermal growth factor receptor overexpression and outcomes in early breast cancer: A systematic review and a meta-analysis. Cancer Treat Rev 62: 1-8.

47. Garcia MP, Shahid A, Chen JY, Xi J (2013) Effects of the expression level of epidermal growth factor receptor on the ligand-induced restructuring of focal adhesions: a QCM-D study. Anal Bioanal Chem 405: 1153-8.
48. Sigismund S, Avanzato D, Lanzetti L (2018) Emerging functions of the EGFR in cancer. Mol Oncol 12: 3-20.
49. Masuda H, Zhang D, Bartholomeusz C, *et al.* (2012) Role of epidermal growth factor receptor in breast cancer. Breast Cancer Res Treat 136: 331-45.
50. Thiery JP (2003) Epithelial-mesenchymal transitions in development and pathologies. Curr Opin Cell Biol 15: 740-6.
51. Butcher DT, Alliston T, Weaver VM (2009) A tense situation: forcing tumour progression. Nat Rev Cancer 9: 108-22.
52. Mason BN, Califano JP, Reinhart-King CA (2012) Matrix Stiffness: A Regulator of Cellular Behavior and Tissue Formation. 19-37.
53. Kalli M, Stylianopoulos T (2018) Defining the Role of Solid Stress and Matrix Stiffness in Cancer Cell Proliferation and Metastasis. Front Oncol 8: 55.
54. Cox TR, Erler JT (2011) Remodeling and homeostasis of the extracellular matrix: implications for fibrotic diseases and cancer. Dis Model Mech 4: 165-78.
55. Engler AJ, Sen S, Sweeney HL, Discher DE (2006) Matrix elasticity directs stem cell lineage specification. Cell 126: 677-89.
56. Erler JT, Weaver VM (2009) Three-dimensional context regulation of metastasis. Clin Exp Metastasis 26: 35-49.
57. Paszek MJ, Weaver VM (2004) The tension mounts: mechanics meets morphogenesis and malignancy. J Mammary Gland Biol Neoplasia 9: 325-42.
58. Samani A, Zubovits J, Plewes D (2007) Elastic moduli of normal and pathological human breast tissues: an inversion-technique-based investigation of 169 samples. Phys Med Biol 52: 1565-76.
59. Provenzano PP, Inman DR, Eliceiri KW, Keely PJ (2009) Matrix density-induced mechanoregulation of breast cell phenotype, signaling and gene expression through a FAK-ERK linkage. Oncogene 28: 4326-43.
60. Bissell MJ, Radisky D (2001) Putting tumours in context. Nat Rev Cancer 1: 46-54.
61. Allred DC (2010) Ductal carcinoma in situ: terminology, classification, and natural history. J Natl Cancer Inst Monogr 2010: 134-8.
62. Wells RG (2008) The role of matrix stiffness in regulating cell behavior. Hepatology 47: 1394-400.
63. Behrens J (1993) The role of cell adhesion molecules in cancer invasion and metastasis. Breast Cancer Res Treat 24: 175-84.
64. Muschler J, Streuli CH (2010) Cell-matrix interactions in mammary gland development and breast cancer. Cold Spring Harb Perspect Biol 2: a003202.
65. Wolf K, Te Lindert M, Krause M, *et al.* (2013) Physical limits of cell migration: control by ECM space and nuclear deformation and tuning by proteolysis and traction force. Journal of Cell Biology 201: 1069-84.
66. Kelley LC, Lohmer LL, Hagedorn EJ, Sherwood DR (2014) Traversing the basement membrane in vivo: a diversity of strategies. Journal of Cell Biology 204: 291-302.
67. Doyle AD, Yamada KM (2016) Mechanosensing via cell-matrix adhesions in 3D microenvironments. Exp Cell Res 343: 60-6.
68. Mrkonjic S, Destaing O, Albiges-Rizo C (2017) Mechanotransduction pulls the strings of matrix degradation at invadosome. Matrix Biol 57-58: 190-203.
69. De Pascalis C, Etienne-Manneville S (2017) Single and collective cell migration: the mechanics of adhesions. Mol Biol Cell 28: 1833-46.
70. Fletcher DA, Mullins RD (2010) Cell mechanics and the cytoskeleton. Nature 463: 485-92.

71. Przybyla L, Muncie JM, Weaver VM (2016) Mechanical Control of Epithelial-to-Mesenchymal Transitions in Development and Cancer. Annu Rev Cell Dev Biol 32: 527-54.
72. Chanet S, Martin AC (2014) Mechanical force sensing in tissues. Prog Mol Biol Transl Sci 126: 317-52.
73. Haase K, Pelling AE (2015) Investigating cell mechanics with atomic force microscopy. J R Soc Interface 12: 20140970.
74. Geiger B, Spatz JP, Bershadsky AD (2009) Environmental sensing through focal adhesions. Nat Rev Mol Cell Biol 10: 21-33.
75. Mattila PK, Lappalainen P (2008) Filopodia: molecular architecture and cellular functions. Nat Rev Mol Cell Biol 9: 446-54.
76. Arjonen A, Kaukonen R, Ivaska J (2011) Filopodia and adhesion in cancer cell motility. Cell Adh Migr 5: 421-30.
77. Sun Z, Guo SS, Fassler R (2016) Integrin-mediated mechanotransduction. Journal of Cell Biology 215: 445-56.
78. Ananthakrishnan R, Ehrlicher A (2007) The forces behind cell movement. Int J Biol Sci 3: 303-17.
79. Carey S. P. CJM, Reinhart-King C. A (2010) Forces During Cell Adhesion and Spreading: Implications for Cellular Homeostasis. Cellular and Biomolecular Mechanics and Mechanobiology: Springer. pp. 29-69.
80. McSherry EA, Donatello S, Hopkins AM, McDonnell S (2007) Molecular basis of invasion in breast cancer. Cellular and Molecular Life Sciences 64: 3201-18.
81. Caswell PT, Zech T (2018) Actin-Based Cell Protrusion in a 3D Matrix. Trends Cell Biol.
82. Jacquemet G, Hamidi H, Ivaska J (2015) Filopodia in cell adhesion, 3D migration and cancer cell invasion. Curr Opin Cell Biol 36: 23-31.
83. Li A, Dawson JC, Forero-Vargas M, *et al.* (2010) The actin-bundling protein fascin stabilizes actin in invadopodia and potentiates protrusive invasion. Curr Biol 20: 339-45.
84. Destaing O, Block MR, Planus E, Albiges-Rizo C (2011) Invadosome regulation by adhesion signaling. Curr Opin Cell Biol 23: 597-606.
85. Seguin L, Desgrosellier JS, Weis SM, Cheresh DA (2015) Integrins and cancer: regulators of cancer stemness, metastasis, and drug resistance. Trends Cell Biol 25: 234-40.
86. Lawson CD, Ridley AJ (2018) Rho GTPase signaling complexes in cell migration and invasion. Journal of Cell Biology 217: 447-57.
87. Guo W, Giancotti FG (2004) Integrin signalling during tumour progression. Nat Rev Mol Cell Biol 5: 816-26.
88. Alizadeh AM, Shiri S, Farsinejad S (2014) Metastasis review: from bench to bedside. Tumour Biol 35: 8483-523.
89. Klein T, Bischoff R (2011) Physiology and pathophysiology of matrix metalloproteases. Amino Acids 41: 271-90.
90. Cathcart J, Pulkoski-Gross A, Cao J (2015) Targeting Matrix Metalloproteinases in Cancer: Bringing New Life to Old Ideas. Genes Dis 2: 26-34.
91. Bartsch JE, Staren ED, Appert HE (2003) Matrix metalloproteinase expression in breast cancer. J Surg Res 110: 383-92.
92. Radisky ES, Radisky DC (2015) Matrix metalloproteinases as breast cancer drivers and therapeutic targets. Frontiers in bioscience (Landmark edition). pp. 1144-63.
93. Deryugina EI, Quigley JP (2006) Matrix metalloproteinases and tumor metastasis. Cancer Metastasis Rev 25: 9-34.
94. Lacroix M, Leclercq G (2004) Relevance of breast cancer cell lines as models for breast tumours: an update. Breast Cancer Res Treat 83: 249-89.

95. Bissell MJ, Radisky DC, Rizki A, Weaver VM, Petersen OW (2002) The organizing principle: microenvironmental influences in the normal and malignant breast. Differentiation 70: 537-46.
96. Lelievre SA, Bissell MJ, Pujuguet P (2000) Cell Nucleus in context. Crit Rev Eukaryot Gene Expr.
97. Hughes CS, Postovit LM, Lajoie GA (2010) Matrigel: a complex protein mixture required for optimal growth of cell culture. Proteomics 10: 1886-90.
98. Kleinman HK, Martin GR (2005) Matrigel: basement membrane matrix with biological activity. Semin Cancer Biol 15: 378-86.
99. Soule HD, Maloney TM, Wolman SR, *et al.* (1990) Isolation and characterization of a spontaneously immortalized human breast epithelial cell line, MCF-10. Cancer Res 50: 6075-86.
100. Debnath J, Muthuswamy SK, Brugge JS (2003) Morphogenesis and oncogenesis of MCF-10A mammary epithelial acini grown in three-dimensional basement membrane cultures. Methods 30: 256-68.
101. Sodunke TR, Turner KK, Caldwell SA, *et al.* (2007) Micropatterns of Matrigel for three-dimensional epithelial cultures. Biomaterials 28: 4006-16.
102. Herr R, Wohrle FU, Danke C, Berens C, Brummer T (2011) A novel MCF-10A line allowing conditional oncogene expression in 3D culture. Cell Commun Signal 9: 17.
103. Cesa CM, Kirchgessner N, Mayer D, *et al.* (2007) Micropatterned silicone elastomer substrates for high resolution analysis of cellular force patterns. Rev Sci Instrum 78: 034301.
104. Bailey AJ, Sims TJ, Light N (1984) Cross-linking in type IV collagen. Biochem J 218: 713-23.
105. Chiu CL, Digman MA, Gratton E (2013) Cell matrix remodeling ability shown by image spatial correlation. J Biophys 2013: 532030.
106. Yamaguchi H, Yoshida S, Muroi E, *et al.* (2011) Phosphoinositide 3-kinase signaling pathway mediated by p110alpha regulates invadopodia formation. Journal of Cell Biology 193: 1275-88.
107. Shaw LM, Rabinovitz I, Wang HHF, Toker A, Mercurio AM (1997) Activation of Phosphoinositide 3-OH Kinase by the α6β4 Integrin Promotes Carcinoma Invasion. Cell 91: 949-60.
108. Harris AK, Wild P, Stopak D (1980) Silicone rubber substrata: a new wrinkle in the study of cell locomotion. Science 208: 177-9.
109. Oliver T, Dembo M, Jacobson K (1995) Traction forces in locomoting cells. Cell Motil Cytoskeleton 31: 225-40.
110. Lee J, Leonard M, Oliver T, Ishihara A, Jacobson K (1994) Traction forces generated by locomoting keratocytes. Journal of Cell Biology 127: 1957-64.
111. Merkel R, Kirchgessner N, Cesa CM, Hoffmann B (2007) Cell force microscopy on elastic layers of finite thickness. Biophys J 93: 3314-23.
112. Plotnikov SV, Sabass B, Schwarz US, Waterman CM (2014) High-resolution traction force microscopy. Methods Cell Biol 123: 367-94.
113. Style RW, Boltyanskiy R, German GK, *et al.* (2014) Traction force microscopy in physics and biology. Soft Matter 10: 4047-55.
114. Butler JP, Tolic-Norrelykke IM, Fabry B, Fredberg JJ (2002) Traction fields, moments, and strain energy that cells exert on their surroundings. Am J Physiol Cell Physiol 282: C595-605.
115. Preibisch S, Saalfeld S, Tomancak P (2009) Globally optimal stitching of tiled 3D microscopic image acquisitions. Bioinformatics 25: 1463-5.
116. Hersch N, Wolters B, Dreissen G, *et al.* (2013) The constant beat: cardiomyocytes adapt their forces by equal contraction upon environmental stiffening. Biol Open 2: 351-61.

117. Houben S, Kirchgeßner N, Merkel R. Estimating Force Fields of Living Cells – Comparison of Several Regularization Schemes Combined with Automatic Parameter Choice. Pattern Recognition; 2010; Berlin, Heidelberg. Springer Berlin Heidelberg. pp. 71-80.
118. Kronenberg NM, Liehm P, Steude A, *et al.* (2017) Long-term imaging of cellular forces with high precision by elastic resonator interference stress microscopy. Nat Cell Biol 19: 864-72.
119. Liehm P, Kronenberg NM, Gather MC (2018) Analysis of the Precision, Robustness, and Speed of Elastic Resonator Interference Stress Microscopy. Biophys J 114: 2180-93.
120. Guzman A, Sanchez Alemany V, Nguyen Y, Zhang CR, Kaufman LJ (2017) A novel 3D in vitro metastasis model elucidates differential invasive strategies during and after breaching basement membrane. Biomaterials 115: 19-29.
121. Paszek MJ, Zahir N, Johnson KR, *et al.* (2005) Tensional homeostasis and the malignant phenotype. Cancer cell 8: 241-54.
122. Boyd NF, Li Q, Melnichouk O, *et al.* (2014) Evidence that breast tissue stiffness is associated with risk of breast cancer. PloS one 9: e100937.
123. Kim JH, Asthagiri AR (2011) Matrix stiffening sensitizes epithelial cells to EGF and enables the loss of contact inhibition of proliferation. J Cell Sci 124: 1280-7.
124. Poschl E, Schlotzer-Schrehardt U, Brachvogel B, *et al.* (2004) Collagen IV is essential for basement membrane stability but dispensable for initiation of its assembly during early development. Development 131: 1619-28.
125. Kim Y, Ollberding NJ, Shvetsov YB, *et al.* (2012) Plasma matrix metalloproteinases and postmenopausal breast cancer risk: a nested case-control study in the Multiethnic Cohort study. Breast Cancer Res Treat 136: 837-45.
126. Schoumacher M, Goldman RD, Louvard D, Vignjevic DM (2010) Actin, microtubules, and vimentin intermediate filaments cooperate for elongation of invadopodia. Journal of Cell Biology 189: 541-56.
127. Koch TM, Munster S, Bonakdar N, Butler JP, Fabry B (2012) 3D Traction forces in cancer cell invasion. PloS one 7: e33476.
128. Northcott JM, Dean IS, Mouw JK, Weaver VM (2018) Feeling Stress: The Mechanics of Cancer Progression and Aggression. Front Cell Dev Biol 6: 17.
129. Jemal A, Bray F, Center MM, *et al.* (2011) Global cancer statistics. CA Cancer J Clin 61: 69-90.
130. Oskarsson T, Batlle E, Massague J (2014) Metastatic stem cells: sources, niches, and vital pathways. Cell Stem Cell 14: 306-21.
131. Insua-Rodriguez J, Oskarsson T (2016) The extracellular matrix in breast cancer. Adv Drug Deliv Rev 97: 41-55.
132. Bosnian FT, Havenith M, Cleutjens JPM (1985) Basement Membranes in Cancer. Ultrastructural Pathology 8: 291-304.
133. Mah EJ, McGahey GE, Yee AF, Digman MA (2018) Collagen stiffness modulates MDA-MB231 cell metabolism through adhesion-mediated contractility. bioRxiv.
134. Jansen KA, Donato DM, Balcioglu HE, *et al.* (2015) A guide to mechanobiology: Where biology and physics meet. Biochim Biophys Acta 1853: 3043-52.
135. Lin HH, Lin HK, Lin IH, *et al.* (2015) Mechanical phenotype of cancer cells: cell softening and loss of stiffness sensing. Oncotarget 6: 20946-58.
136. Friedl P, Alexander S (2011) Cancer invasion and the microenvironment: plasticity and reciprocity. Cell 147: 992-1009.
137. Stowers RS, Allen SC, Sanchez K, *et al.* (2017) Extracellular Matrix Stiffening Induces a Malignant Phenotypic Transition in Breast Epithelial Cells. Cellular and Molecular Bioengineering 10: 114-23.

138. Chaudhuri O, Koshy ST, Branco da Cunha C, *et al.* (2014) Extracellular matrix stiffness and composition jointly regulate the induction of malignant phenotypes in mammary epithelium. Nat Mater 13: 970-8.
139. Saxena M, Liu S, Yang B, *et al.* (2017) EGFR and HER2 activate rigidity sensing only on rigid matrices. Nat Mater 16: 775-81.
140. Guo G, Gong K, Wohlfeld B, *et al.* (2015) Ligand-Independent EGFR Signaling. Cancer Res 75: 3436-41.
141. Schwartz AD, Hall CL, Barney LE, Babbitt CC, Peyton SR (2017) Mechanosensing of Integrin α6 and EGFR Converges at Calpain 2. bioRxiv.
142. Comoglio PM, Boccaccio C, Trusolino L (2003) Interactions between growth factor receptors and adhesion molecules: breaking the rules. Current Opinion in Cell Biology 15: 565-71.
143. Subik K, Lee JF, Baxter L, *et al.* (2010) The Expression Patterns of ER, PR, HER2, CK5/6, EGFR, Ki-67 and AR by Immunohistochemical Analysis in Breast Cancer Cell Lines. Breast Cancer (Auckl) 4: 35-41.
144. Wei W-C, Lin H-H, Shen M-R, Tang M-J (2008) Mechanosensing machinery for cells under low substratum rigidity. American Journal of Physiology-Cell Physiology 295: C1579-C89.
145. Gimona M, Buccione R (2006) Adhesions that mediate invasion. Int J Biochem Cell Biol 38: 1875-92.
146. Spagnolo B, Brunetti V, Lemenager G, *et al.* (2015) Three-dimensional cage-like microscaffolds for cell invasion studies. Sci Rep 5: 10531.
147. Denais CM, Gilbert RM, Isermann P, *et al.* (2016) Nuclear envelope rupture and repair during cancer cell migration. Science 352: 353-8.
148. Fabris G (2016) Cellular biomechanics in 2D and 3D epithelial model tissues: from keratin intermediate filaments to breast gland in vitro reconstructed basement membranes. Bonn: Rheinischen Friedrich-Wilhelms-Universität Bonn. 188 p.
149. Koshikawa N, Minegishi T, Sharabi A, Quaranta V, Seiki M (2005) Membrane-type matrix metalloproteinase-1 (MT1-MMP) is a processing enzyme for human laminin gamma 2 chain. J Biol Chem 280: 88-93.
150. Mainiero F, Pepe A, Yeon M, Ren Y, Giancotti FG (1996) The intracellular functions of alpha6beta4 integrin are regulated by EGF. Journal of Cell Biology 134: 241-53.
151. Mercurio AM, Rabinovitz I, Shaw LM (2001) The α6β4 integrin and epithelial cell migration. Current Opinion in Cell Biology 13: 541-5.
152. Wolf K, Mazo I, Leung H, *et al.* (2003) Compensation mechanism in tumor cell migration: mesenchymal-amoeboid transition after blocking of pericellular proteolysis. Journal of Cell Biology 160: 267-77.
153. Even-Ram S, Yamada KM (2005) Cell migration in 3D matrix. Curr Opin Cell Biol 17: 524-32.
154. Debnath J, Brugge JS (2005) Modelling glandular epithelial cancers in three-dimensional cultures. Nat Rev Cancer 5: 675-88.
155. Underwood JM, Imbalzano KM, Weaver VM, *et al.* (2006) The ultrastructure of MCF-10A acini. J Cell Physiol 208: 141-8.
156. Adams JC (2001) Cell-matrix contact structures. Cellular and Molecular Life Sciences CMLS 58: 371-92.
157. Vivanco I, Sawyers CL (2002) The phosphatidylinositol 3-Kinase–AKT pathway in human cancer. Nature Reviews Cancer 2: 489.
158. Costa RLB, Han HS, Gradishar WJ (2018) Targeting the PI3K/AKT/mTOR pathway in triple-negative breast cancer: a review. Breast Cancer Res Treat 169: 397-406.

159. Das K, Prasad R, Ansari SA, *et al.* (2018) Matrix metalloproteinase-2: A key regulator in coagulation proteases mediated human breast cancer progression through autocrine signaling. Biomed Pharmacother 105: 395-406.
160. Huttenlocher A, Horwitz AR (2011) Integrins in cell migration. Cold Spring Harb Perspect Biol 3: a005074.
161. Rubashkin MG, Cassereau L, Bainer R, *et al.* (2014) Force engages vinculin and promotes tumor progression by enhancing PI3K activation of phosphatidylinositol (3,4,5)-triphosphate. Cancer Res 74: 4597-611.
162. Murphy DA, Courtneidge SA (2011) The 'ins' and 'outs' of podosomes and invadopodia: characteristics, formation and function. Nat Rev Mol Cell Biol 12: 413-26.

Acknowledgements

First of all I would like to thank Prof. Rudolf Merkel for admission at the Institute of Complex Systems (ICS-7), for the opportunity to work in his group on this thesis and for his guidance and many critical but supportive discussions.

I would also like to express my thanks to Prof. Kubitscheck for accepting to be my doctoral referee and taking the time to review my work.

My deepest gratitude is to my supervisor, Dr. Erik Noetzel-Reiss, for providing me with this fascinating research topic, for his advice and guidance, for giving me encouragement and for the support during the entire course of this thesis.

A big thanks also to Dr. Bernd Hoffmann for critical and constructive discussions, and for his expertise.

My special gratitude goes to our collaboration partners Dr. Nils Kronenberg and Prof. Malte Gather. Their experimental expertise was a cornerstone for this thesis. I am especially thankful to Dr. Nils Kronenberg for his support during ERISM measurements and for helping with data evaluation.

I'm also thankful to all my colleagues at the ICS-7.
A special thank goes to Dr. Ronald Springer, for his IT support and his readiness to always help solve any statistical or data evaluation problem. I would become desperate without your support, especially during the last days while writing this thesis.
A big thank goes to Dr. Barbara Nöthel, for many critical and supporting discussions and for proofreading this thesis.
I am also thankful to Julian Eschenbruch for precious collaboration and for providing with some data.
Lastly, I thank my former cubicle neighbor Dr. Tobias Braun for pleasant company, as well as Georg Dreissen and Lisann Esser for the great time at ICS-7.

My special thanks go to my family, as this thesis would not have been possible unless their encouragement and tolerance during the last years. In loving commemoration of my grandfather, I would like to thank him for supporting me spiritually throughout my life, and being an inspiring example.

Last but not least, I want to thank my lovely husband Yaroslav Shcherbak and our beloved daughter for their support and tolerance, especially during the last months.

Publications

Gaiko-Shcherbak, A.[1], Fabris, G.[1], Dreissen, G., Merkel, R., Hoffmann, B., Noetzel, E. (2015) The Acinar Cage: Basement Membranes Determine Molecule Exchange and Mechanical Stability of Human Breast Cell Acini. *PloS one* 10: e0145174.

Rose, M., Kloten, V., Noetzel, E., Gola, L., Ehling, J., Heide, T., Meurer, S.K., Gaiko-Shcherbak, A., Sechi, A.S., Huth, S., Weiskirchen, R., Klaas, O., Antonopoulos, W., Lin, Q., Wagner, W., Veeck, J., Gremse, F., Steitz, J., Knüchel, R., Dahl, E. (2017) ITIH5 mediates epigenetic reprogramming of breast cancer cells. *Mol Cancer* 16(1): 44.

[1] These authors contributed equally.